2008-12-23

Dynamic Optical Model of the Primate Crystalline Lens and Implications for the Restoration of Accommodation

David Borja
University of Miami, dborja@med.miami.edu

UNIVERSITY OF MIAMI

DYNAMIC OPTICAL MODEL OF THE PRIMATE CRYSTALLINE LENS AND IMPLICATIONS FOR THE RESTORATION OF ACCOMMODATION

By

David Borja

A DISSERTATION

Submitted to the Faculty
of the University of Miami
in partial fulfillment of the requirements for
the degree of Doctor of Philosophy

Coral Gables, Florida

December 2008

UNIVERSITY OF MIAMI

A dissertation submitted in partial fulfillment of
the requirements for the degree of
Doctor of Philosophy

DYNAMIC OPTICAL MODEL OF THE PRIMATE CRYSTALLINE LENS AND IMPLICATIONS FOR THE RESTORATION OF ACCOMMODATION

David Borja

Approved:

Fabrice Manns, Ph.D.
Associate Professor of Biomedical Engineering and Ophthalmology

Terri A. Scandura, Ph.D.
Dean of the Graduate School

Jean Marie Parel, Ph.D.
Henri and Flore Lesieur Chair in Ophthalmology, Research Associate Professor of Ophthalmology and Biomedical Engineering

Sonia H. Yoo, M.D.
Associate Professor of Clinical Ophthalmology

Arthur Ho, M.Optom., Ph.D., F.A.A.O.
Executive Director Technology, Institute for Eye Research and Professorial Visiting Fellow, School of Optometry and Vision Science, University of New South Wales, Sydney, Australia

Jorge Bohorquez, Ph.D.
Research Assistant Professor of Biomedical Engineering

Weizhao Zhao, Ph.D.
Associate Professor of Biomedical Engineering

BORJA, DAVID (Ph.D., Biomedical Engineering)
(December 2008)

Dynamic Optical Model of the Primate Crystalline Lens and Implications for the Restoration of Accommodation

Abstract of a dissertation at the University of Miami.

Dissertation supervised by Professor Fabrice Manns.
No. of Pages of text. (174)

The human crystalline lens is a complex, inhomogeneous and dynamic optical element which enables the eye to adjust focus in a process known as accommodation. Age related changes in the optical and mechanical properties of the lens cause a loss in accommodative ability leading to a condition known as presbyopia. Several experimental surgical techniques are under development for the correction of presbyopia. The goal of this dissertation is to better understand the relationship between the crystalline lens shape, its non-uniform refractive index gradient and its optical power and their changes with age and accommodation. In this study direct lens power and shape measurements were acquired on isolated lenses, and on lenses mounted in a lens stretching system designed to simulate accommodation. Several lens shape and power measurement techniques were developed for this study including a Scheimpflug camera system optimized for imaging the crystalline lens. Direct measurements of lens shape and power were used to develop an age-dependent optical-mechanical model of the lens during accommodation. The study shows that the normal growth of the lens is a major contributor to the progressive loss of accommodation amplitude, independent of changes in the elastic properties of the lens. These findings suggest that accommodation can be restored by refilling the lens with a material having a uniform refractive index.

I dedicate this dissertation to my mother, Leonor Cardona and my father, Juan Borja

ACKNOWLEDGEMENTS

I would like to acknowledge and thank my mentor, Fabrice Manns, Ph.D., for his patience, guidance, wisdom, and tireless dedication. I would also like to acknowledge Jean-Marie Parel, Ph.D., for his support, mentorship, guidance and constant demand for excellence. I would like to thank Arthur Ho, M.Optom., Ph.D., F.A.A.O., for his mentorship and important contributions to this project. I would also like to acknowledge my remaining committee members Sonia Yoo, MD, Jorge E. Bohorquez, Ph.D., and Weizhao Zhao, Ph.D. for their willingness to participate and review this dissertation.

I would like to thank Stephen R. Uhlhorn, Ph.D., Rakhi Jain, Ph.D., and Gaku Takeuchi, MS, for their important contributions to this project as well as their guidance. I would like to thank my fellow students at the Ophthalmic Biophysics Center for their support. I would like to thank to Noel Ziebarth, Ph.D., Omer Kocaglou Ph.D., Alexandre Rosen, MD, Alberto de Castro, Andres Bernal, MS, and Raksha Urs, MS, for their contributions to this project. Special thanks are due to Peggy D Lamar, Izuru Nose, David Denham, MS, M.B.A., and William G. Lee of the Ophthalmic Biophysics Center for their technical support. I am indebted to the surgical staff of the OBC especially Viviana Fernandez MD, Esdras Arrieta MD, and Ana Carolina Acosta MD.

I would like to thank my parents Juan Borja and Leonor Cardona for all the sacrifices they made to provide an education for me and my brothers. I would like to thank my brothers Andrew and Jay Borja for their patience and support throughout my education. Finally I would like to give special thanks to my fiancée Marcia Orozco, MS for her love, patience and selfless support.

TABLE OF CONTENTS

LIST OF FIGURES

PUBLICATION NOTE

The following are peer-reviewed articles, conference proceedings, presentations, and posters on the work described in this dissertation:

Peer-Reviewed Publications:

Borja D, Manns F, Ho A, Ziebarth N, Acosta AC, Arrieta E, Augusteyn RC, and Parel J-M Optical power and biometric properties of the isolated non-human primate crystalline lens. *Investigative Ophthalmology and Visual Science*; In preparation.

Borja D, Manns F, Ho A, Ziebarth N, Rosen A, Jain R, Amelinckx A, Arrieta E, Augusteyn R, and Parel J-M. Optical power of the isolated human crystalline lens. *Investigative Ophthalmology and Visual Science*; 49 (6): 2541-2548, 2008.

Uhlhorn SR, **Borja D,** Manns F, Parel J-M. Refractive Index Measurement of the Isolated Crystalline Lens Using Optical Coherence Tomography. *Vision Research; 48 (27):* 2732-2738, 2008.

Urs R, Manns F, Ho A, **Borja D,** Amelinckx A, Smith J, Jain R, Parel J-M. Shape of the isolated ex-vivo human crystalline lens. *Vision Research;* In press.

Augusteyn RC, Rosen AM, **Borja D,** Ziebarth NM, Parel J-M. Biometry of Primate Lenses during Immersion in Preservation Media. *Molecular Vision*. 12:740-747, 2006.

Rosen AM, **Borja D,** Denham DB, Fernandez V, Ho A, Manns F, Parel J-M; In vitro dimensions and curvatures of human lenses. *Vision Research* 46:1002-1009, 2006

Conference Proceedings and Presentations:

Borja D, Uhlhorn S, Arrieta E, Augusteyn R, Manns F, K Ehrmann, Ho A, Parel J-M. Changes in lens shape and power of ex vivo monkey crystalline lenses during simulated accommodation. In *Ophthalmic Technologies XVIII,* 6844A-24, 2008.

Urs R, **Borja D,** Smith J, Manns F, Parel J-M. Profile of the whole ex-vivo human crystalline lens. In *Ophthalmic Technologies XVIII,* 6844A-23, 2008.

Uhlhorn S, **Borja D,** Manns F, Parel J-M. Refractive index measurement of the crystalline lens using optical coherence tomography. In *Ophthalmic Technologies XVIII*, 6844A-27, 2008.

Borja D, Rosen A, Augusteyn RC, Ho A, Manns F, Parel J-M. Ex vivo equivalent refractive index and biometric properties of postmortem primate crystalline lenses, In *Ophthalmic Technologies XVI, Proceedings SPIE 6426,* 2007.

Uhlhorn SR, **Borja D,** Ziebarth NM, Manns F, Parel J-M. Optical Coherence tomography of the crystalline lens during simulated accommodation. ARVO Abstract and Poster #990, Association of Research in Vision and Ophthalmology Annual Meeting, Ft.Lauderdale, FL, 2007.

Ho A, Hoang MH, **Borja D,** Amelinckx A,Manns F, Parel J-M. Optical Power and Diameter of In Situ versus Isolated Primate Crystalline Lenses Ex Vivo. ARVO Abstract and Poster #3816, Association of Research in Vision and Ophthalmology Annual Meeting, Ft.Lauderdale, FL, 2007

Borja D, Rosen A, Hoang MH, Amelinckx A, Augusteyn R, Manns F, Ho A, Parel J-M. Equivalent Refractive Indices of Isolated Human and Monkey Crystalline Lenses. ARVO Abstract and Poster #3817, Association of Research in Vision and Ophthalmology Annual Meeting, Ft.Lauderdale, FL, 2007

Borja D, Rosen A, Augusteyn R, Manns F, and Parel J-M; Equivalent Refractive Index of Postmortem Cynomolgus Monkey Crystalline Lenses. ARVO Abstract and Poster #1209, Association of Research in Vision and Ophthalmology Annual Meeting, Ft.Lauderdale, FL, 2006.

Uhlhorn SR, **Borja D,** Manns F, and Parel J-M; Refractive Index Measurement of the Monkey Crystalline Lens Using Optical Coherence Tomography. ARVO Abstract and Poster #2627, Association of Research in Vision and Ophthalmology Annual Meeting, Ft.Lauderdale, FL, 2006.

Borja D, Takeuchi G, Ziebarth N, Acosta AC., Manns F, Parel J-M, Crystalline lens MTF measurement during simulated accommodation, In *Ophthalmic Technologies XV, Proceedings SPIE 5688,* 19-25, 2005.

Other related works published during the course of my doctoral studies:

Peer-Reviewed Publications:

Nankivil D, Manns F, Arrieta-Quintero E, Ziebarth N, **Borja D,** Amelinckx A, Bernal A, Ho A, Parel J-M. Effect of Anterior Zonules on the Change in Lens Diameter and Power in Non-Human Primates during Simulated Accommodation. *Investigative Ophthalmology and Visual Science*; Accepted pending revisions.

Ziebarth N, **Borja D,** Arrieta E, Aly M, Manns F, Dortonne I, Nankivil D, Jain R, Parel J-M. Role of the lens capsule on the mechanical accommodative response in a lens stretcher. *Investigative Ophthalmology and Visual Science*; 49(10):4490-6, 2008.

Manns F, Parel J-M, Denham D, Billotte C, Ziebarth N, **Borja D,** Fernandez V, Aly M, Arrieta E, Ho A, Holden B. Optomechanical response of human and monkey lenses in a lens stretcher. *Investigative Ophthalmology and Visual Science*; 48 (7): 3260-3268, 2007.

Conference Proceedings and Presentations:

Tinoco G, Ziebarth NM, **Borja D,** Manns F, Arrieta E, Parel J-M. Contribution of the ciliary body to the forces measured during simulation of accommodation. ARVO Abstract and Poster #986, Association of Research in Vision and Ophthalmology Annual Meeting, Ft.Lauderdale, FL; 2007.

Nankivil D, Ziebarth NM, **Borja D,** Arrieta E, Ho A, Manns F, Parel J-M. Effect of anterior Zonular dissection on the change in lens diameter and power during simulated accommodation. ARVO Abstract and Presentation #5631, Association of Research in Vision and Ophthalmology Annual Meeting, Ft.Lauderdale, FL; 2007.

Manns F, Ziebarth NM, **Borja D,** Arrieta E, Ho A, Parel J-M. Age-dependence of the power-load and diameter-load responses of human and monkey lenses during simulation of accommodation in a lens stretcher. ARVO Abstract and Presentation #5632, Association of Research in Vision and Ophthalmology Annual Meeting, Ft.Lauderdale, FL; 2007

Parel J-M, Manns F, Denham D, Billotte C, Fernandez V, Abri A, Acosta AC, Ziebarth NM, **Borja D**, Ho A. Comparison of the Optomechanical Response of Human and Monkey Lenses During Simulation of Accommodation in a Lens Stretcher. ARVO Abstract and Presentation #5890, Association of Research in Vision and Ophthalmology Annual Meeting, Ft.Lauderdale, FL; 2006.

CHAPTER 1. AIMS OF THE STUDY

The human crystalline lens is a complex, inhomogeneous and dynamic optical element with a gradient refractive index which gives the eye the ability to adjust focus in a process known as accommodation. Age related changes in the optical and mechanical properties of the lens cause a loss in accommodative ability leading to a condition known as presbyopia. According to the most widely accepted theory, presbyopia is due mainly to a progressive loss of the elasticity of the crystalline lens with age. Several experimental surgical techniques are under development for the correction of presbyopia.

The work described in this dissertation is part of the Dynamic Vision Project (DV Project), an international collaboration between the University of Miami's Ophthalmic Biophysics Center (OBC) and the Vision Cooperative Research Centre (Vision CRC) of Australia. The goal of the DV project is to restore accommodation through an experimental surgical lens refilling technique known as Phaco-Ersatz. In this technique the presbyopic lens contents are removed and replaced with a flexible polymer designed to mimic the properties of the pre-presbyopic lens.

The restoration of accommodation requires a complete knowledge of the age dependent optical and mechanical properties of the lens and how they change during accommodation. Much of the missing information can be obtained from experiments on ex vivo human and animal crystalline lenses. Measurements of ex vivo lens optical and mechanical properties during simulated accommodation can be used to develop a numerical optical and mechanical model of the accommodation process.

The goal of this dissertation is to better understand the relationship between the crystalline lens shape, its non-uniform refractive index gradient and its optical power and

their changes with age and accommodation. The information acquired in this dissertation will be used to optimize the properties of the Phaco-Ersatz lens refilling implant. The specific aims are:

Aim 1: Development of an age dependent optical model of the isolated lens

The age-dependence of the isolated human and non-human primate crystalline lens power will be measured and characterized. The refractive contributions of the lens surfaces and refractive index gradient to the maximally accommodated lens power will be quantified as a function of age. The results will produce a baseline refractive index value required to restore the natural static refractive power of the maximally accommodated lens after Phaco-Ersatz. The results will also provide information on the age dependence of the maximally accommodated state of the lens and the lenticular factors contributing to presbyopia.

Aim 2: Determine how the refractive contributions of the gradient refractive index affect the accommodative amplitude of the lens.

The shape and refractive power of human and non-human primate crystalline lenses will be measured during ex vivo simulated accommodation in a custom designed *ex vivo* accommodation simulation system. A Scheimpflug imaging system will be developed to create cross-sectional images of the lens during stretching. The changes in lens shape and power during stretching will be used to quantify the refractive contributions of the gradient and surfaces to the change in lens power. The results will be used to quantify the age-dependent refractive contribution of the lens gradient refractive index to the amplitude of accommodation.

Aim 3: Development of an age and accommodation dependent optical model of the lens

The data obtained in Aims 1 and 2 will be used to develop a dynamic optical model which accurately describes the changes in the shape and power of the lens with age and accommodation. This information will be used to develop and refine an optical and mechanical model of the human accommodative process. Overall this study will produce a new level of understanding on the optics of the lens, the changes leading to presbyopia and the factors that influence the outcome of procedures to restore accommodation.

CHAPTER 2. BACKGROUND AND SIGNIFICANCE

2.1. Basic lens anatomy

The eye's ability to change focus is provided by the dynamic optical mechanical properties of the crystalline lens. The crystalline lens is positioned behind the cornea, the aqueous humor and the iris and in front of the vitreous and retina (Figure 2.1A). The lens is suspended by ligaments called the zonular fibers to a circular ciliary muscle which is attached to the choroid. The lens itself is avascular and composed of the capsule, epithelium, cortex, and nucleus (Figure 2.1B). The lens is surrounded by an optically clear and elastic extracellular matrix, the lens capsule. The mechanical properties of the lens capsule help mold the shape of softer lens matter by applying a constant tension to the lens contents (Fincham 1937). The lens capsule is secreted by a single cell layer of cuboidal lens epithelial cells (Bebe 2002). Nucleated epithelial cells are present only in the anterior surface of the lens. The lens epithelial cells migrate towards the lens equator, differentiate and elongate into lens fiber cells. Lens fiber cells are laid down in concentric layers over older fibers which are pushed toward the center of the lens. The lens fiber cells are able to be tightly packed due to their horizontal cross-sections. The optical clarity of the lens is due to the tight packing structure, the lack of organelles and the high concentration of the crystalline proteins within the lens fiber cells (Kaufmann 2002, Chapter 5). Unlike other ocular tissue the lens continually grows throughout life. The continual growth of the lens and variations in protein and water concentration gives the lens non-uniform opto-mechanical properties (Smith and Pierscionek 1998). The lens has two distinct regions, a fetal nucleus at the center which present at birth and the

surrounding cortex which consists of layers of lens fiber cells (Glasser and Kaufmann 2002).

A.

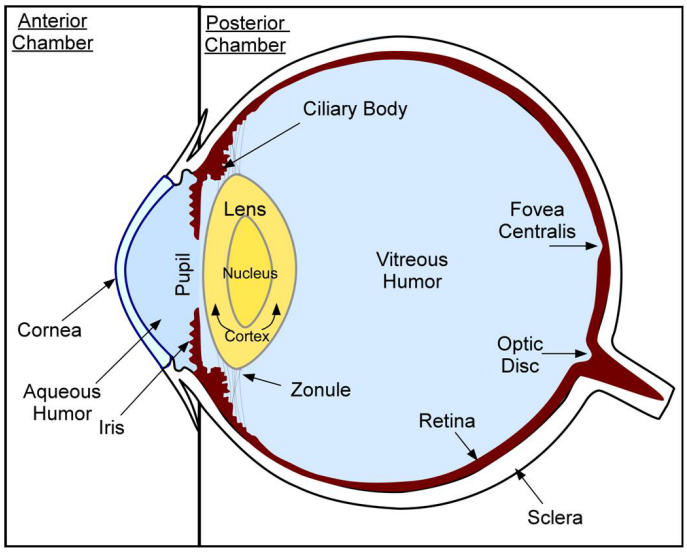

B.

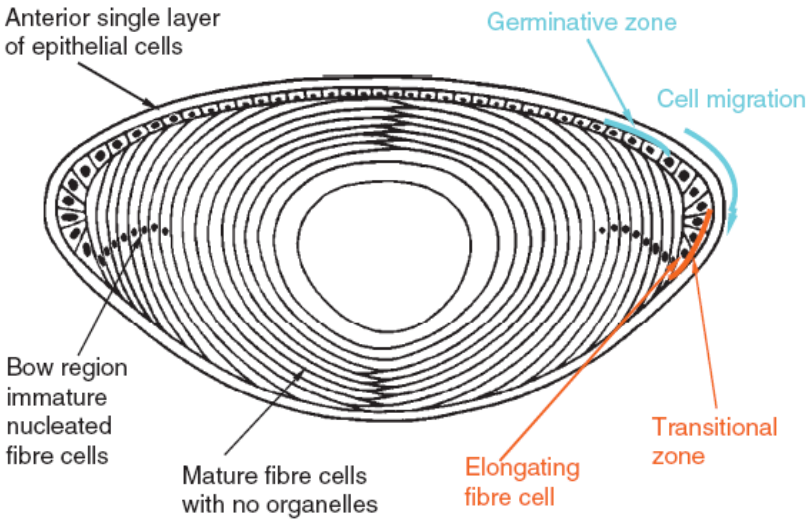

Figure 2.1: A. Cross-section of the eye. B. The schematic of the lens cellular structure and the differentiation of lens epithelial cells into lens fiber cells (Augustyn 2008). The lens does not discard non-viable cells because the lens is an enclosed by the lens capsule. Instead the cells are compacted and pushed towards the center. This process leads to a non-uniform refractive index distribution within the lens which increases towards the center of the lens.

2.2. Accommodation

The lens contributes to about one third of the eye's total refractive power but the major role of the lens is to allow the eye to focus on either near or far objects in a process called accommodation (Atchison and Smith 2000) (Figure 2.2). The eye's ability to accommodate is due to the lens' ability to change shape and refractive power. The most widely accepted theory of accommodation is the Hemholtz theory, which attributes the increase in refractive power of the lens during near vision to the contraction of the ciliary muscles and relaxation of the lens suspensory zonule. This causes the elastic lens capsule to mold the soft lens contents into a shape with shorter radii of curvature, causing an increase in refractive power. When the lens is in an unaccommodated state as is the case in viewing distant objects, the ciliary body and muscles are radially expanded. This causes a tensioning of the zonule, which in turn causes a tightening of the lens capsule, flattening the curvatures and lowering the refractive power of the lens.

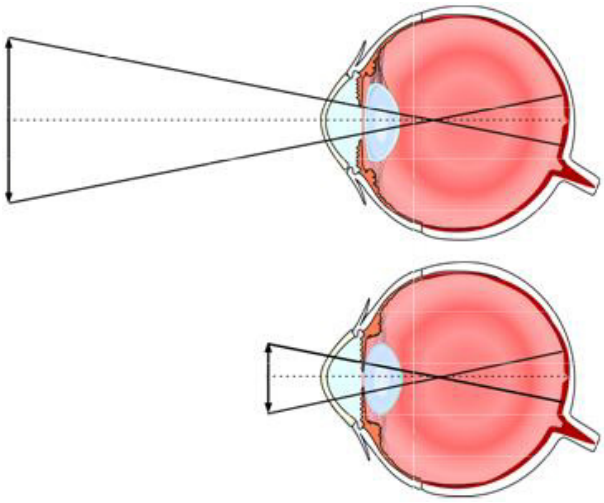

Figure 2.2: The change in focus of the eye during accommodation. When viewing distant objects (top), the ciliary muscles are relaxed, causing a tensioning of the zonules and the lens capsule which flattens the anterior and posterior lens surfaces. When viewing near objects (bottom), the ciliary mucle contracts which releases the tension on the zonules and the lens capsule. This causes the curvature of the anterior and posterior lens surfaces to increase which increases the lens refractive power.

2.3. The loss of accommodation with age and presbyopia

Starting from birth, the lens progressively loses its ability to change refractive power resulting in the eye's progressive loss of accommodation (Figure 2.3). Presbyopia is the loss of near visual function that eventually results from the progressive loss of accommodation with age. Accommodation is a result of a complex interaction of the accommodative apparatus which is composed of many different types of tissues (the lens, lens capsules, the zonuler fibers, the ciliary body, and the choroid) and systems (including the central nervous system). Aging affects many of these tissues in different ways (Kaufmann, Chapter 7). There are a number of age-related changes in the lens anatomical, mechanical and optical properties, including elasticity, volume, thickness, diameter, surface curvatures and refractive index (Weale 1963). The contribution of these changes to the decrease in accommodative amplitude is not well understood.

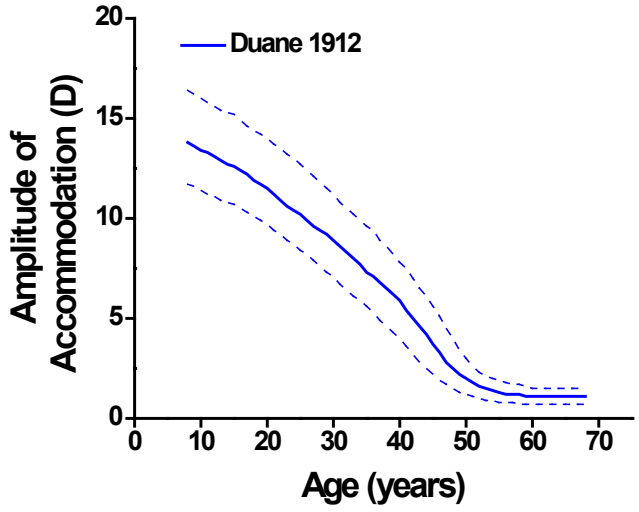

Figure 2.3: Age dependence of voluntary accommodation amplitude (Duane 1912). As the lens ages it loses its ability to change shape resulting in the eye's loss of accommodation amplitude. The symptomatic loss of accommodation amplitude is known as presbyopia. Typically the symptoms of presbyopia start between the ages of 40 and 50 years.

2.4. Restoration of accommodation

2.4.1. General description

In a presbyopic eye the near focus required for close work such as reading can be achieved simply by wearing spectacles or contact lenses. Glasses are an inexpensive and non-surgical correction. However, they do not restore a continuous range of focus. There are currently several surgical techniques under investigation to restore accommodation (Parel et al 2004) including lens refilling, scleral expansion, lens nucleus photodisruption and several different accommodating intraocular lens (IOL) designs.

2.4.2. Scleral expansion

Scleral expansion surgery relies on the controversial Shachar theory of accommodation which attributes the loss of accommodation amplitude to the continuous equatorial growth of the lens. According to this theory, this growth of the lens progressively reduces zonular tension. The scleral expansion procedure is designed to increase the space between the lens equator and the ciliary body using scleral implants. Clinical studies of this technique show that this procedure does not restore accommodation (Kleinmann, Kim and Yee 2006).

2.4.3. Accommodating intraocular lenses

Intraocular lenses (IOLs) are silicone or acrylic implants placed in the empty capsular bag after cataract surgery to replace the refractive power of the lens. Typical IOLs are rigid devices which provide a fixed refractive power and do not restore a dynamic range of accommodative refractive power. Developments in IOL materials and designs have led to IOLs which may provide a dynamic range of accommodation. These accommodating intraocular lenses (AIOL) rely on contraction of the ciliary muscle to

create either a change in optical power of the device itself or an axial displacement of the optical element to induce a change in optical power of the eye (figure 2.4) (Menapace et al 2007). Optical modeling and clinical studies have shown that these accommodating IOLs provide limited amplitude of accommodation on the order of 1D of accommodation (Ho *et al,* 2006). A recent comparative study of commercially available accommodating IOLs found some movement under pharmacological stimulation but no movement at all under normal physiological stimulation. (Menapace et al 2007)

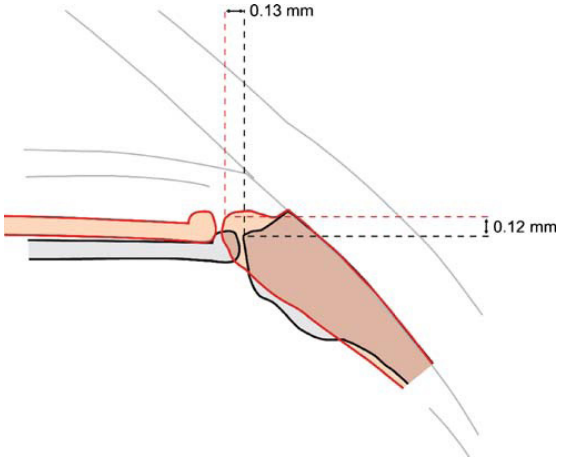

Figure 2.4: Accommodating intraocular lenses rely on contraction of the ciliary muscle to create either a change in optical power of the device itself or an axial displacement of the optical element to induce a change in optical power of the eye (Menapace et al 2007). In this figure contraction of the ciliary muscle would displace a rigid IOL in the anterior direction by 1.0-1.5mm. However fibrosis of the lens capsule has an immobilizing effect.

2.4.4. Photodisruption of the presbyopic lens

Photodisruption of the presbyopic lens relies on the lens sclerosis theory of presbyopia (Fisher 1971). This theory attributes the age related loss of accommodation to a progressive loss of elasticity of the lens. These techniques propose restoring accommodation by modifying the mechanical properties of the lens.

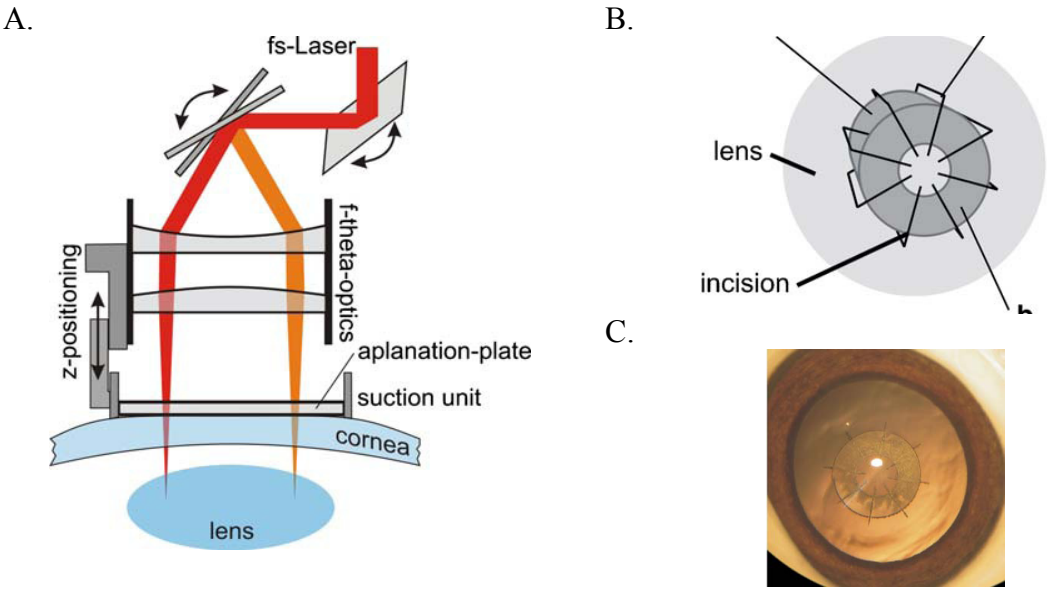

Figure 2.5: A. A schematic of the lens photo disruption laser delivery system. B. A schematic of the laser treatment pattern for the creation of gliding planes within the lens. C. An image of an ex vivo pig eye after lens photodisruption (Ripken et al 2008).

Photodisruption attempts to restore the elasticity of the crystalline lens by creating microincisions inside lens tissue to either achieve gliding planes within the lens (figure 2.5) (Ripken et al 2008) or to modify the modulus of elasticity of the lens (Krueger et al 2001). The microincisions are typically made with near-infrared high power ultra-short laser pulses. These procedures are currently in an early development stage and the efficacy remains to be demonstrated in vivo.

2.4.5. Lens refilling techniques

The goal of lens refilling techniques such as Phaco-Ersatz (Parel, 1986) is to replace the hardened lens contents with an elastic polymer having optical and mechanical properties similar to those of the young pre-presbyopic lens (Figure 2.6). The feasibility of restoring accommodation using this technique was initially demonstrated in the senile

rhesus monkey using a biocompatible polymer material (Haefliger *et al,* 1994; Nishi *et al,* 1998). The successful clinical realization of the Phaco-Ersatz lens refilling technique requires coordinated development of new optical, biomechanical, surgical and polymer technologies. To address these issues a large multi-disciplinary research and development program funded through the Australian government, the Dynamic Vision Project, was initiated in 1997 by the CRCERT (Cooperative Research Centre for Eye Research and Technology), Sydney Australia in collaboration with the OBC (Ophthalmic Biophysics Center) at the Bascom Palmer Eye Institute in Miami. The goal of the Dynamic Vision project is to develop surgical techniques, polymers, ex vivo optical and mechanical testing platforms as well as optical and mechanical models to optimize the procedure.

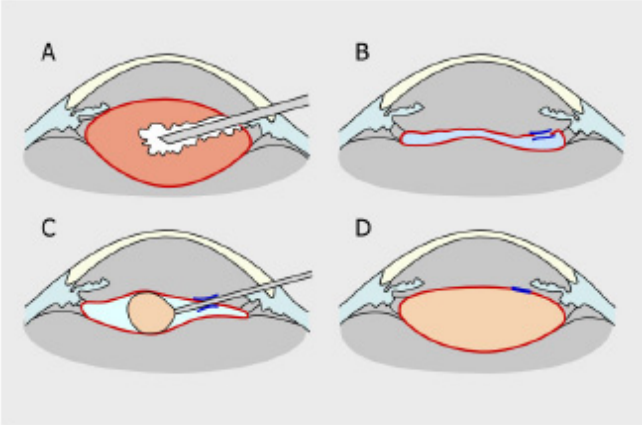

Figure 2.6: In the Phaco-Ersatz lens refilling technique the hardened lens contents are removed through a small incision in the periphery of the lens (A). A small valve is placed on the empty capsular bag (B) before injection of the soft polymer (C). The mechanical and optical properties of the polymer restore the natural lens accommodative amplitude (D). (Parel 1986)

2.5. Importance of the project and missing information

The optimization of the Phaco-Ersatz lens refilling technique requires a better understanding of how the shape and refractive index of the lens affects the accommodative response and its changes with age. One issue of a particular interest is to determine how the optical mechanical response of a lens refilled with a homogeneous material with a uniform refractive index compares to that of the natural lens which has a gradient of optical and mechanical properties.

Previous studies on the optics of the crystalline lens have focused on developing optical models designed to predict the optical performance of the complete eye (Navarro 1985, Liou and Brennan 1997). These models are not based on a correct anatomical description of the lens and most of these models do not take into account lens changes with age and accommodation. The goal of this dissertation is to provide an accurate age and accommodation dependent model that is anatomically correct based on direct measurements of the lens shape and power over a wide age range. This model will serve as a benchmark for the Phaco-Ersatz procedure and other techniques which are designed to restore the dynamic process of accommodation.

CHAPTER 3. PARAXIAL OPTICAL PROPERTIES OF THE LENS

3.1. Objective

This chapter reviews the current knowledge of the paraxial optical properties of the crystalline lens. Including:

- existing paraxial optical models of the crystalline lens
- the refractive index gradient of the lens and its contribution to accommodation
- the lens shape and its changes with age and accommodation
- the comparison of human and monkey lenses

3.2. Paraxial representation and refractive power of a lens

3.2.1 Cardinal points

In paraxial optics an optical system is fully defined by the location of four cardinal planes and six cardinal points, (Figure 3.1).

- two focal points (*F* and *F'*)
- two principal points (*H* and *H'*)
- two nodal points (*N* and *N'*)
- two focal planes (F and F')
- two principal planes (P and P')

When the optical system is surrounded by two media with equal refractive indices (n_1=n_3 in Figure 3.1) the principal points coincide with the nodal points. The image forming properties of an optical system are determined from the positions of these cardinal planes and cardinal points.

- The first focal point is the axial point in the object space whose conjugate is located at infinity. Any ray passing through the first focal point will emerge from the optical system parallel to the optical axis (see the blue ray in Figure 3.1).

- The second focal point is the axial point in the image space whose conjugate is located at infinity. Any ray entering the optical system parallel to the optical axis will emerge from the optical system and pass through the second focal point (see the red ray in Figure 3.1).
- The first and second focal planes are orthogonal to the optical axis and pass through the focal points (blue dashed lines in Figure 3.1).
- The two principal planes are conjugate planes orthogonal to the optical axis with unit lateral magnification. Any ray with height *h* intersecting the first principal plane will emerge from the second principal plane at the same height *h* (see blue and red rays in Figure 3.1).
- The two principal points are the intersections of the principal planes with the optical axis.
- The two nodal points are conjugate axial points of unit angular magnification. Any ray entering an optical system passing through the first nodal point will emerge from the optical system through the second nodal point with the same angle as the incoming ray (see purple ray in Figure 3.1).

The position of the cardinal points defines the focal lengths of an optical system:

- the front focal length (*ffl*) is the distance from the front focal point to the vertex of the system
- the back focal length (*bfl*) is the distance from the back vertex to the second focal point
- the effective focal length (*efl* = *f'*) the distance from the second principal point to the second focal point.

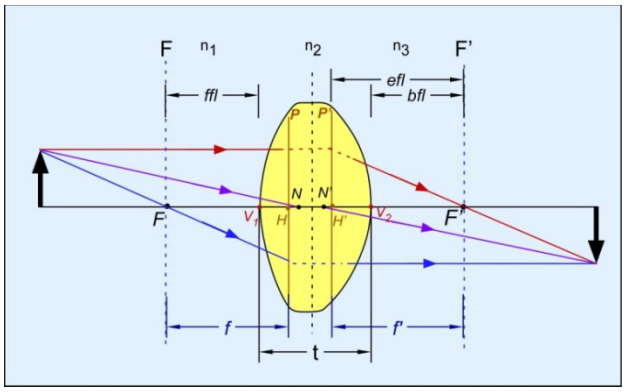

Figure 3.1: The cardinal planes and points completely define the imaging properties of an optical system in the paraxial region. The paraxial region is valid only for extremely small object heights and angles.

3.2.2. Refractive power

Refractive power is a measure of the degree to which an optical system bends (converges or diverges) light. With the notation of Figure 3.1, refractive power (P) is defined as:

$$P = \frac{n_3}{f'} \qquad \text{Eq. 3.1}$$

For an optical system surrounded by air (n_{air}=1) the power is the reciprocal of focal length (P=1/f). The dioptre (D) is the common unit for optical power. One dioptre is equal to one inverse meter. For a single spherical surface (Figure 3.2.a) the refractive power P (D) is given by:

$$P = \frac{n'}{f'} = \frac{n' - n}{r} \qquad \text{Eq. 3.2}$$

Where n and n' are the refractive indices of the surrounding media and r is the radius of curvature of the surface. For a system of two spherical surfaces separated by a distance t, such as a thick spherical lens (Figure 3.2.b.) the refractive power P in (D) is given by:

$$P = \frac{n_3}{f'} = \frac{n_2 - n_1}{r_1} + \frac{n_3 - n_2}{r_2} - \frac{t}{n_2}\left(\frac{n_2 - n_1}{r_1}\right)\left(\frac{n_3 - n_2}{r_2}\right) \qquad \text{Eq. 3.3}$$

Where r_1 and r_2 are the radii of curvature of the surfaces separated by a distance t, n_2 is the refractive index of the lens matter and n_1 and n_3 are the refractive indices of the surrounding media.

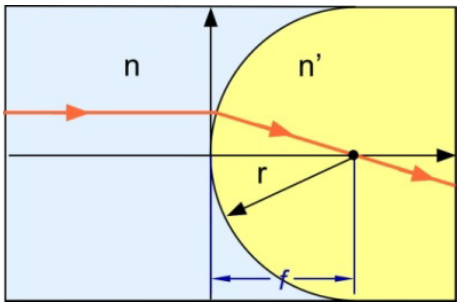

Figure 3.2: Refractive power of a single spherical refractive surface.

3.3. The paraxial power of the crystalline lens: effect of the index gradient

The lens has an onion-like layered structure (Figure 2.1b) with the oldest innermost layers under increasing compression. The growth pattern of the lens produces a non-uniform refractive index distribution (Figure 3.3) with a peak value (typically around 1.40 to 1.41) in the center and a lower value at the lens surfaces (typically around 1.37 to 1.38) (Pierscionek et al 1988, Pierscionek and Chan 1989, Jones *et al*, 2005).

A.

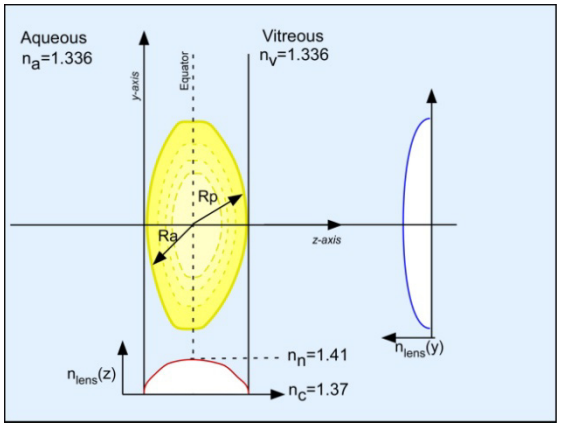

B.

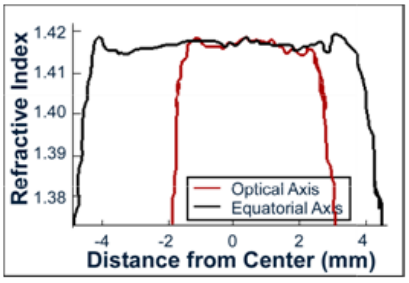

C.

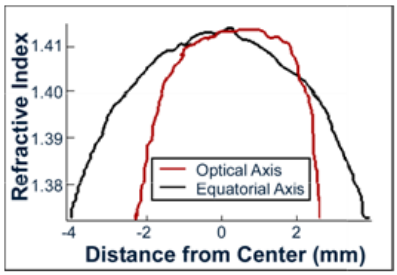

Figure 3.3: Gradient refractive index distribution of the lens in the axial and equatorial directions. The refractive index distribution of an 8 (B) and 82 (C) year old lens measured *in vitro* using an MRI technique (Jones et al, 2005).

Since the lens does not have a uniform refractive index, equation 3.3 cannot be directly applied to calculate the lens power. To circumvent this problem it is customary to introduce the concept of an equivalent refractive index. The equivalent refractive index (Neq) is defined as the uniform refractive index value that is required inside the lens to provide a power equal to the actual crystalline lens power if all other parameters (surface curvatures and thickness) remain equal (Equation 3.4). The refractive power of the equivalent crystalline lens P_{EQ} is given by:

$$P_{EQ} = \frac{N_{eq} - N_a}{R_a} + \frac{N_v - N_{eq}}{R_p} - \frac{t}{N_{eq}}\left(\frac{N_{eq} - N_a}{R_a}\right)\left(\frac{N_v - N_{eq}}{R_p}\right) \qquad \text{Eq. 3.4}$$

where N_a and N_v are the refractive index value of the aqueous and the vitreous respectively (typically both are assumed to be 1.336), R_a and R_p are the radii of the anterior and posterior surfaces and t is the central axial thickness of the lens. Typically the values of the biometric parameters (t, Ra, Rp) have been obtained from indirect *in vivo* measurements or direct *in vitro* techniques (Brown 1974, Mutti et al 1992, Dubbelman and Van der Heijde 2001). The equivalent refractive index has been determined indirectly from in vivo measurements of ocular dimensions and total ocular refractive state. The ocular dimensions are used to develop a customized eye model. The equivalent refractive index is then calculated so that the refractive state of the customized eye model matches the refractive state of the in vivo eye. Calculations typically result in an equivalent refractive index higher than the peak refractive index within the lens. Published values of the equivalent refractive index of the human crystalline lens vary from 1.416 to 1.422 (Bennett and Rabbetts 1998).

3.4. Schematic models of the crystalline lens

3.4.1. General description

Several paraxial schematic optical models of the lens have been developed based on measurements and calculations. Typically for the purpose of first order optical modeling of lens equivalent power, these models assume spherical surfaces and a uniform equivalent refractive index which may be valid for an average human eye (Liou and Brennan 1996). More complex models take into account the gradient refractive index, age, or accommodation dependent changes of the lens. Current schematic models do not describe the continual growth of the lens or the continual changes in the lens shape during accommodation.

3.4.2. The Gullstrand-Emsley Schematic Eye

The Gullstrand No. 1 exact schematic eye (1909) model describes the shape and power of the lens in the unaccommodated and accommodated states with four spherical surfaces. The four surfaces include the anterior and posterior lens surfaces and two inner surfaces which define the boundaries of an inner core. The core has a higher refractive index then the outer regions of the lens (Figure 3.4). Gullstrand also developed a simplified model using a uniform refractive index throughout the lens. This model was later updated by Emsley (1952) (table 3.1).

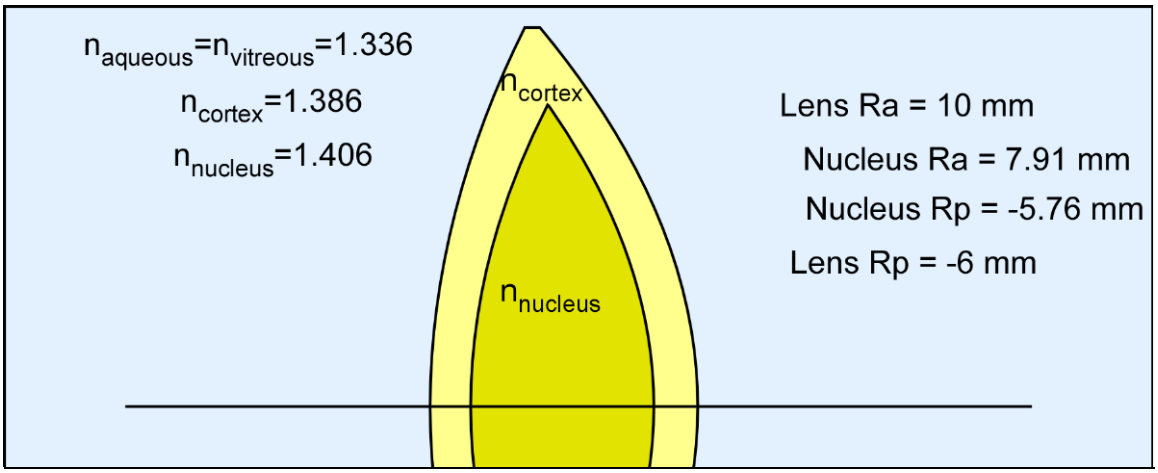

Figure 3.4: The lens of the Gullstrand No.1 Exact Schematic Eye (1909).

Gullstrand - Emsley (Emsley 1952)	Relaxed (0D)	Accommodated (8.6D)
Equivalent power (D)	21.76	32.30
Equivalent refractive index	1.416	1.416
Lens thickness (mm)	3.6	4
Anterior radius of curvature (mm)	10	5
Posterior radius of curvature (mm)	-6	-5

Table 3.1: The lens of the Gullstrand-Emsley Schematic eye.

3.4.3. The Bennett-Rabbetts Schematic Eye

The values presented in the Gullstrand-Emsley schematic eye were further refined by Bennett and Rabbetts (1998) to include updated ocular dimensions. The Bennett and Rabbetts schematic eye described the lens with two spherical surfaces and with an equivalent refractive index of 1.422 for the adult lens. Additional values are also given for an elderly and an infant lens. In this model the equivalent refractive index of the lens decreases from 1.49 in the infant to 1.406 in the elderly lens.

Bennett-Rabbetts (1998)	Infant	Adult Accommodative Response					Elderly
		0(D)	2.5(D)	5(D)	7.5(D)	10(D)	
Equivalent Power (D)	43.5	20.83	24.16	27.38	30.63	33.78	18.71
Equivalent Refractive index	1.49	1.422	1.422	1.422	1.422	1.422	1.406
Lens thickness (mm)	Not Given	3.7	3.825	3.93	4.02	4.09	4.45
Anterior radius of curvature (mm)	8.7	11	8.6	7	6	5.2	9.25
Posterior radius of curvature (mm)	-5.6	-6.47515	-5.909	-5.504	-5.063	-4.75	-6.13

Table 3.2: The lens of the Bennett-Rabbetts Schematic eye.

3.5. Advanced models of the lens

3.5.1. General description

The advanced lens models take into account the refractive index gradient, changes in lens shape with accommodation and/or age, and/or the asphericity of the lens surfaces. The lens surfaces are known to be aspherical. The lens surface curvatures flatten in the periphery. The aspheric surfaces of the lens are described most often by conic sections (Lotmar 1971, Howcroft and Parker 1977, Kooijman 1983, Liou and Brennan 1997, Dubbleman et al 2001). The asphericity of the lens surfaces must be taken into account in models designed to predict optical aberrations of the eye or when an exact ray trace is required.

The advanced models do not necessarily rely on accurate anatomical data. Instead the values for the lens index gradient and surface curvatures are tailored to match measurements of ocular aberrations. In other words these optical models provide an artificial equivalent lens model which is designed to predict the optical performance of the whole eye. These models therefore cannot be used to investigate the relation between the lens shape and power and their changes with age and accommodation.

A. B.

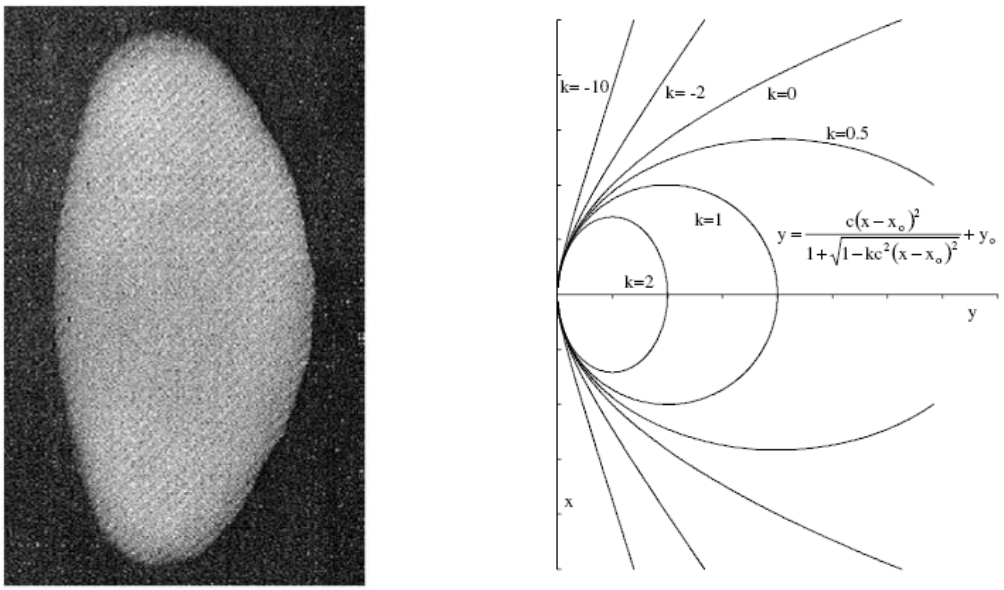

Figure 3.5: Examples of previous *in vitro* lens shape measurement studies. (A) Histological sections prepared by cryofixation technique which may affect lens shape (Howcroft and Parker 1977). B. The lens surface profiles can be described by the equation for a conic section where k is the surface conic constant or shape factor and c is the apex radius of curvature (Dubbelman et al 2005).

3.5.2. The Navarro Eye Model

The most widely used advanced optical model of the lens is from the Navarro (1985) eye model (Table 3.3). This model includes aspheric lens surfaces and accommodation dependent values for the lens shape (Table 3.3). This model is based on the Gullstrand-Emsley eye with the addition of surface asphericities obtained from the measurements of Howcroft and Parker (1977) (Figure 3.5). The accommodation dependent lens shape and refractive index values in the Navarro eye model were artificially determined to match the accommodated Gullstrand eye model (Navarro 1985). No age dependence for the lens shape, refractive power or gradient was given in the original Navarro eye model.

Navarro et al (1985)	Relaxed (0D)	Accommodation dependent model	Accommodated (10D)
Equivalent power (D)	21.79*		34.55
Equivalent refractive index	1.42*	$1.42 + 9x10^{-5} \cdot (10 \cdot A + A^2)$	1.438
Lens thickness (mm)	4*	$4 + 0.1 \cdot \ln(A + 1)$	4.24
Anterior radius of curvature (mm)	10.2*	$10.2 - 1.75 * \ln(A + 1)$	6.00
Anterior surface asphericity (Qa)	-3.13**	$-3.13 - 0.34 - \ln(A + 1)$	-3.95
Posterior radius of curvature (mm)	-6*	$-6 + 0.2294 * \ln(A + 1)$	-5.45
Posterior surface asphericity (Qp)	-1**	$-1 - 0.125 - \ln(A + 1)$	-1.30

Table 3.3: The lens described by the Navarro eye model. *Values obtained from the Gullstrand- Emsley schematic eye. **Values obtained from Howcroft and Parker 1977.

3.5.3. Gradient refractive index models of the lens

Two important lens optical models have been developed with a gradient refractive index for the lens (Smith et al 1991 and Liou and Brennan 1998). These models incorporate in vitro gradient refractive index distribution measurements acquired with a laser ray tracing approach (Pierscionek and Chan 1989) (Figure 3.6). In this technique a thin beam enters the lens parallel to the optical axis and is refracted by the lens. Information about the refractive index distribution can be obtained by predicting and tracing the path of the beam within the lens. Pierscionek and Chan (1989) and Smith et al (1991) among others studied the human lens with this technique. The analysis and interpretation of experimental results from laser ray tracing requires the use of mathematical models to describe the gradient distribution (Navarro et al 2007). This requires assumptions and simplifications which may be invalid (Smith 2003).

A.

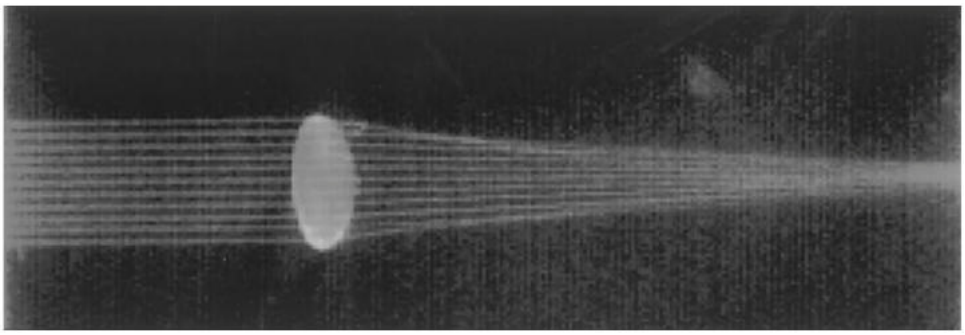

B.

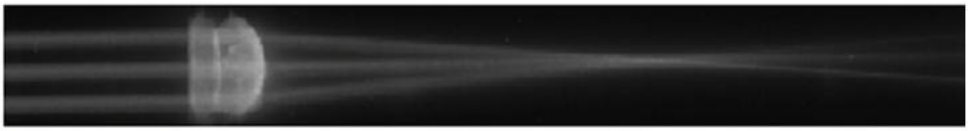

Figure 3.6: In vitro refractive power of the lens measured with a laser ray tracing technique. Glasser and Campbell 1998 and 1999 (A.) Jones et al 2005 (B.)

Recently the refractive index distributions of *in vitro* lenses have been mapped with an MRI technique (Figure 3.7) (Moffat et al 2002, Jones et al 2005). This technique has been used to show that the refractive index distribution is age dependent (Jones *et al,* 2005). A similar recent in vivo study (Kasthurirangan et al 2008) found that the shape of the central refractive index plateau changes with age and accommodation. However, the MRI technique is limited by low resolution (~0.2mm) and low signal-to-noise ratio.

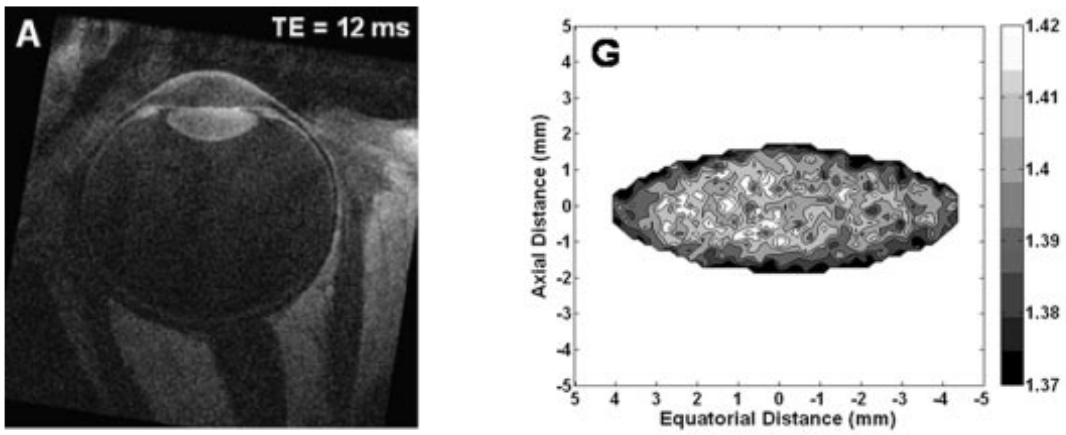

Figure 3.7: Examples of in vivo high resolution MR images of the lens (Kasthurirangan et al. 2008). The images are 256x256pixels in size and have a 40mm field of view and a 3mm slice thickness. The 2D image resolution is 0.156mm.

3.5.4. The Liou and Brennan Eye Model

Liou and Brennan (1997) developed an eye model with aspheric lens surfaces and a gradient refractive index for the lens. This model is not age or accommodation dependent. This study incorporated in vivo lens shape measurements obtained by Brown (1974) utilizing a Scheimpflug slit-lamp biometry technique (Figure 3.8). Brown measured the shape of the relaxed lens in 200 emmetropic patients between the ages of 3 and 82 years. Liou and Brennan reanalyzed the original images obtained by Brown to obtain an average anterior and posterior surface asphericities. However, they did not provide age dependence for the surface curvatures or asphericity. Most importantly the Scheimpflug technique originally developed by Brown suffers from optical distortions. These distortions must be corrected to obtain accurate biometric data of the lens (Dubbelman and Van der Heijde 2001).

Liou and Brennan 1997	
Gradient refractive index profile	$n(w,z) = n_{00} + n_{01}z + n_{02}z^2 + n_{10}w^2$
Anterior Lens thickness (mm)	1.59
Anterior radius of curvature (mm)	12.4
Anterior surface asphericity Qa	-0.94
Posterior Lens thickness	2.43
Posterior radius of curvature (mm)	-8.1
Posterior surface asphericity Qp	0.96

Table 3.4: The lens of the Liou and Brennan (1997) eye model. In this model the gradient refractive index distribution is parabolic and obtained from Pierscionek and Chan (1989). The model gives the value of the refractive index n(w,z) where z is the distance along the optical axis w is the radial distance from the optical axis ($w^2=x^2+y^2$).

3.5.5. The Smith Eye Model

The gradient index profile utilized by Liou and Brennan (1997) was originally developed by Smith et al (1991). The original model developed by Smith et al included

three different index profiles and age dependent lens thickness and curvature measurements from in vitro lenses (Pierscionek 1994). Recently (Smith 2003) this model has been updated to include in vivo lens shape measurements from Koretz et al 2001. This model however does not incorporate lens changes during accommodation.

Smith 1991 and 2003	
Gradient refractive index profile	elliptical, bi-elliptical or conic iso-indicial profiles
Lens thickness (mm)	3.46 + 0.013 x age
Anterior radius of curvature (mm)	11.155 - 0.02004 x age
Anterior surface asphericity Qa	-2.233 + 0.03660 x age -0.0001429 x age^2
Posterior radius of curvature (mm)	-8.267 + 0.02025 x age
Posterior surface asphericity Qp	+0.9402 + 0.002863 x age - 0.000008929 x age^2

Table 3.5: The lens described by the Smith 1991 and 2003 eye models.

3.5.6. The Dubbelman Eye Model

Scheimpflug imaging has been used to describe changes in the lens shape as a function of age Brown (1974). This technique has been improved by the use of image processing correction. This technique has been used for lens shape measurements as a function of accommodation stimulus (Dubbelman and Van der Heijde 2001; Dubbelman et al 2005; Rosales et al 2006; Koretz et al 1987 a and b, 1988). The results have been used to develop an age and accommodation dependent model of the crystalline lens (Norby 2005). In vivo geometric lens shape data obtained from this technique is limited to the central 6mm of the lens surfaces because the iris obscures the lens periphery, the zonules and the ciliary body (Figure 3.8). The main limitation of in vivo Scheimpflug imaging is that it requires an assumption on the lens equivalent refractive index to calculate the shape of the posterior lens surface. In addition the lens power cannot be

directly measured in vivo. The lens power must be calculated from measurements of ocular dimensions and refractive state. Even though a recent study showed that this technique provides relatively accurate values of the central radii of curvature (Rosales et al 2006), it does not provide direct measurements of the lens refractive power or refractive index gradient contribution.

A. B.

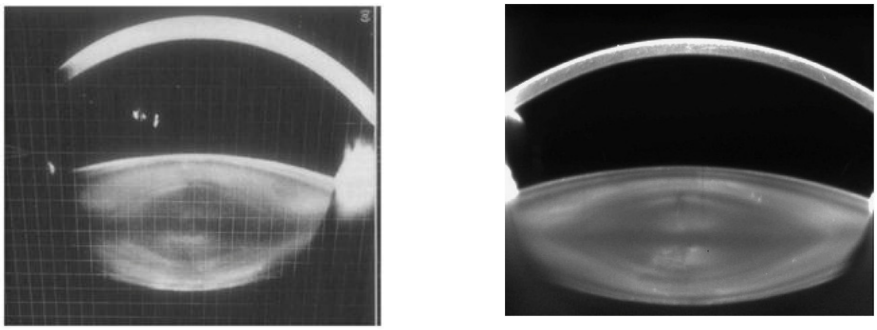

Figure 3.8: Uncorrected Scheimpflug images of a 29 year old unaccommodated subject (Brown 1974) and a 28 year old subject (Hermans et al 2008). Once corrected this technique allows for accurate measurements of lens shape and internal structure.

Dubbelman et al 2001, 2005 and Norby 2005	
Equivalent refractive index (Neq)	1.441 - 0.00039A + 0.0013D
Lens thickness (mm)	2.93 + 0.0236A + D(0.058 - 0.0005A)
Anterior radius of curvature (mm)	1/[1/(12.9 - 0.057A) + 0.0067D]
Anterior surface asphericity Qa	-(4 + 0.5D)
Posterior radius of curvature (mm)	1/[1/(6.2 - 0.0012A) + 0.0037D]
Posterior surface asphericity Qp	-3

Table 3.6: The lens described by the Dubbelman eye model. Where 'A' is the age in years (valid from 16-65 years of age) and 'D' is the accommodative state in Diopters.

3.5.7. Non-human primate crystalline lens as a model for the human lens

Non-human primates have been used as models for myopia, emmetropization and accommodation (Törnqvist 1966, Kaufman *et al.* 1979, Bito *et al.* 1982, Koretz *et al*. 1987 A, B and 1988, Glasser and Kaufman 1999, Qiao-Grider *et al.* 2007). Monkeys are

the only species that are known to accommodate like humans do. Most notably, the accommodative apparatus and age-dependent changes in the accommodative ability of the rhesus monkey have been shown to be similar to those of humans (Figure 3.9) (Bito *et al.* 1982, Koretz *et al.* 1987a &b, Neider *et al.* 1990, Croft *et al.* 1998, Glasser and Kaufman 1999, Croft *et al.* 2006, Wendt *et al.* 2008). For these reasons a number of intraocular implants and surgical procedures to correct presbyopia are being evaluated in the cynomolgus and rhesus monkey (Parel 1986, Haefliger and Parel 1994, Nishi *et al.*1998, and Koopmans *et al.* 2006).

Despite these general similarities, there are key interspecies differences in lens shape and power between humans and monkeys (Qiao-Grider *et al.* 2007). It has been suggested that there may be different underlying causes of presbyopia in monkeys and humans due to species differences in lens growth and ciliary body aging (Strenk *et al.* 2006). Since the monkey eye is often used as a model for the human eye in physiological optics, it is important to precisely quantify the optical and biometric properties of the monkey eye and to better characterize the interspecies differences.

One of the goals of this study is to characterize the shape and the optical properties of crystalline lenses from three non-human primate species (rhesus monkey, cynomolgus monkey and hamadryas baboon) as a function of age and accommodation. The results will be compared to the results from human lenses and to determine if the non-human primate is a good model for accommodation and presbyopia research.

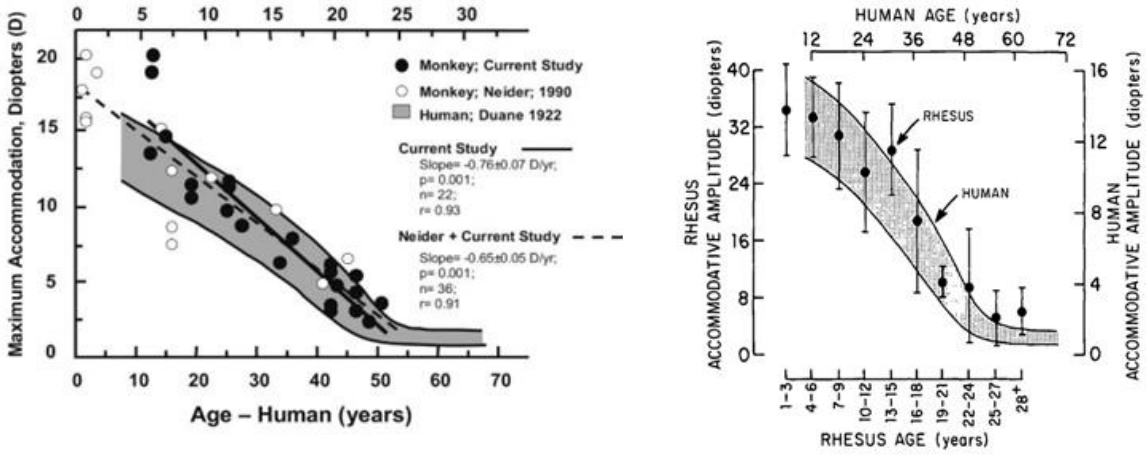

Figure 3.9: The age-dependent loss in accommodative amplitude in human and non-human primates (Left - Croft *et al* 2006, Right - Bito et al 1982).

3.6. Summary and conclusion

Many investigators have presented in vivo data on the shape of the lens and its changes with accommodation and age. This data has been used to develop optical models of the eye. However, one key issue with in vivo lens data is that the shape and refractive power of the lens cannot be measured directly. During in vivo measurements the lens is imaged through the cornea and the posterior lens surface is imaged through the anterior lens surface and the internal lens structure. The refractive components of the eye anterior to the lens surfaces cause optical distortions which limit the accuracy of the measurement. Furthermore the optical models that have been developed have been optimized to match the optical performance of the whole eye. In these models the lens shape and optical parameters have been adjusted to this affect. These models cannot be used to provide a true relation between changes with lens shape and power. A complete description of the effects of age and accommodation on the lens shape and power is

critical for the basic understanding of the accommodative mechanism, presbyopia and for the restoration of accommodation.

The purpose of this study is to develop an accurate age and accommodation dependent optical model of the lens from direct measurements of lens shape and power. Direct measurements of lens shape and power will be performed on isolated lenses free of external forces and lenses mounted in an ex vivo accommodation simulation system (lens stretching) on fresh human and non-human primate tissue samples. Ex vivo lens stretching experiments will also provide measurements of the age-dependent optomechanical response of the lens and the force required to stretch and to dissaccommodate the lens. This model will describe:

-the age-dependent changes in lens shape and power during accommodation

-the lens surfaces refractive contributions during accommodation

-the refractive contributions from the gradient refractive index

-the surface and the gradient refractive contributions to the lens power change

-and the changes in the lens shape and power which contribute to the progressive loss of accommodative ability of the lens

Ultimately the information obtained from this study will be compiled into an optical model of the primate crystalline lens which will be used in the development of the Phaco-Ersatz procedure.

CHAPTER 4. DEVELOPMENT OF IN VITRO CRYSTALLINE LENS MEASUREMENT TECHNIQUES

4.1. Objective

The goals of aims 1 and 2 are to measure and characterize the age-dependence of *in vitro* crystalline lens shape and power in the isolated state free of external forces and during simulated accommodation in the EVAS lens stretching system. These studies require the development of several lens shape and power measurement techniques as well as an optical model of the lens. This chapter describes the design and development of:

-in vitro lens power measurement systems (section 4.2)

-in vitro lens shape measurement techniques (section 4.3)

-and optical modeling techniques (section 4.4)

4.2. In vitro lens refractive power measurements

4.2.1. General description

Measurements of the refractive power of *in vitro* lenses are performed while the lens is submerged in an aqueous preservation medium. This medium helps maintain the natural hydration state of the lens and simulates the *in vivo* situation where the lens is surrounded by aqueous humor (n=1.336) on the anterior side and vitreous humor (n=1.336) on the posterior side. The refractive power of the lens is always specified with values of the surrounding media refractive index set equal to those of the aqueous and vitreous humor (n=1.336). Refractive power measurement systems measure either the effective refractive power or the back vertex power of the crystalline lens.

The effective refractive power (P_{EQ}) of the equivalent crystalline lens is given by: (see chapter 3.3)

$$P_{EQ} = \frac{N_v}{efl} = \frac{N_{eq} - N_a}{R_a} + \frac{N_v - N_{eq}}{R_p} - \frac{t}{N_{eq}}\left(\frac{N_{eq} - N_a}{R_a}\right)\left(\frac{N_v - N_{eq}}{R_p}\right) \quad \text{Eq. 4.1}$$

Where N_V is the refractive index of the vitreous, *efl* is the effective focal length in meters N_a is the refractive index of the aqueous, N_{eq} is the lens equivalent refractive index, R_a and R_p are the anterior and posterior lens surface curvatures and *t* is the lens thickness. The equivalent refractive power uses the second principal plane as the reference for measurement of the focal length (*efl*). However the exact position of the second principal plane is not always known. In these cases the equivalent refractive power can be estimated by setting an arbitrary location for the second principal plane.

The systems which measure back vertex power do so by directly measuring the distance from the lens posterior surface to the focus. The back vertex power (P_B) is given by:

$$P_B = \frac{N_v}{bfl} = \frac{N_v}{efl - d} \quad \text{Eq. 4.2a.}$$

Where d is the distance between the second principal point and the posterior lens vertex. Equation 4.2 can be written:

$$P_B = \frac{N_v}{efl} \cdot \frac{1}{1 - \frac{d}{efl}} = P_{EQ} \cdot \frac{1}{1 - \frac{d}{efl}} \quad \text{Eq. 4.2b.}$$

Equation 4.2b shows that when $d << efl$, the back vertex power can be assumed to be equal to the effective refractive power. Since the lens is biconvex, the distance *d* will always be less than the thickness of the lens. The highest power lenses are young isolated monkey lenses with a power of approximately 60 D and a thickness on the order of 4 mm. With these values which correspond to a worst case scenario, the relative difference between the effective and the back vertex power is on the order of 22 % (13 D). For human lenses the error is expected to be less than 5 % (<1 D).

The following is a description of several devices which have been adapted or specifically designed to measure the effective or the back vertex refractive power of in vitro crystalline lenses while submerged in a preservation media. Different refractive power measurement devices were required to measure the in vitro lens at different states of dissection and in a full range of accommodative states. These systems include:

- a modified commercial lensmeter which measures the isolated lens equivalent power
- a Scheiner lensmeter which measures the equivalent power of the lens during simulated accommodation in a lens stretching system
- a Scheiner lensmeter which measures the back vertex power of the lens during simulated accommodation in a second generation lens stretching system
- and a Badal lensmeter which was used to measured the effects of the accommodative framework on the lens equivalent power

4.2.2. Zeiss humphrey lensmeter – Isolated lens power

Refractive power measurements of the isolated lens were performed with a commercial lensmeter (Lens Analyzer 350, Zeiss Humphrey, Dublin, CA) (Figure 4.1) modified to allow measurements of isolated crystalline lenses. This system allows for quick, accurate and precise lens power measurements with little manipulation to the lens. This system delivers four parallel beams arranged in a 4.24mm or a 5.83mm square pattern on the test lens. The four parallel light beams are passed through a rotating chopper disk which allows only one light ray to pass at a time. With no test lens present the beam strikes a photodetector at a given reference position. When a test lens is present the lens refracts the incident beams and causes a displacement of the read position on the photodetector. The prism power (P_p) of the test lens is then calculated from

the horizontal displacement (d_1) of the beam and the distance (x) between the test position and the measurement position.

$$P_p = \frac{d_1}{x} \quad \text{Eq. 4.3}$$

The beam displacement and prism power is measured at all four locations. The lens equivalent refractive power (P_{EQ}) is then calculated by use of Prentice's Rule:

$$P_{EQ} = \frac{P_p}{d_2} \cdot x \quad \text{Eq. 4.4}$$

Where d_2 is the distance from the lens optical axis and the center of the test beam. The system gives the equivalent refractive power of a thin lens placed at the test position. This measurement is an estimate of the thick crystalline lens equivalent refractive power.

The system was originally designed for measurement of spectacle lenses (2.83mm entrance beam height) and contact lenses (2.21mm entrance beam height) and has a manufacturer calibrated measurement range of -45 to 45D. A custom designed testing cell filled with tissue preservation media was designed to allow for measurements of isolated crystalline lenses (Denham et al 2003 44: E-Abstract 244). The lens was positioned on a rubber o-ring for stability. This lensmeter system was calibrated on a set of plano-convex lenses in the range of 4 to 53 D. The calibration measurements were repeated three times with a precision of ±0.19D between repeated measurements. The system had a measurement error ranging from -1.98 to 0.86D with an RMS error 0.66 D

A

B

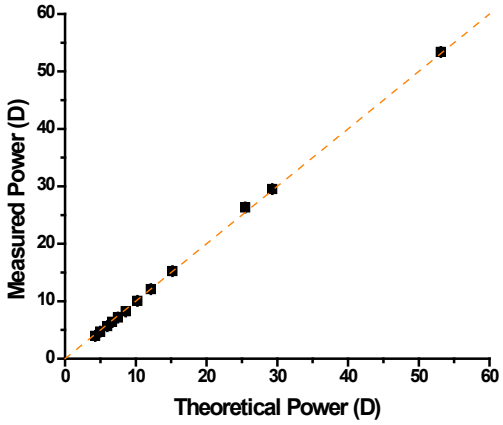

C

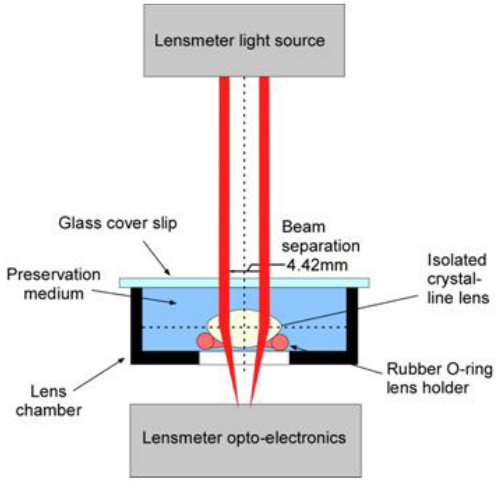

Figure 4.1: A. Isolated lens refractive power measurement with a commercial lensmeter (Lens Analyzer 350, Zeiss Humphrey, Dublin CA). B. The isolated lens testing cell consisted of a clear Petri dish filled with a lens preservation medium. C. Calibration on glass lenses submerged in water.

4.2.3. Lensmeter based on the Scheiner principle

Two custom lensmeter systems were developed at the Ophthalmic Biophysics Center for refractive power measurements of in vitro crystalline lenses during simulated accommodation. The systems measure the optical power of in vitro crystalline lenses while mounted in either the first or second generation EVAS lens stretcher systems. Both optical systems are based on the Scheiner principle (Manns et al 2007, Figure 4.2).

In the first generation lens stretcher (EVAS I) system light from a laser diode is coupled into a single mode fiber. The light from the fiber is collimated into a parallel beam by a 25mm

focal length achromat lens. The collimated beam passes through a metal disk with 0.3mm diameter holes placed in a 3mm square pattern. The four parallel laser beams are delivered at normal incidence to the lens. The parallel beams are focused by the lens. A camera mounted on a vertical translation stage is positioned behind the testing chamber. The stage is moved until the camera is located at the point of convergence of the four incident beams. This location corresponds to the focal plane of the lens. The effective refractive power of the lens immersed in the testing chamber is calculated using a formula derived from a paraxial optical model of the system. This system assumes that the principal point of the test lens is located at the plane of the lens equator. This optical system was calibrated on the same plano-convex lenses as the Humphrey system in the range of 12 to 53 D. The system had a measurement error ranging from -1.8 to 2.9D (average 1.5D).

The second generation lens stretcher system (EVAS 2) utilizes the beam delivery system of a custom designed optical coherence tomography system (OCT). The OCT beam delivery system consists of a fiber coupled superluminescent diode, emitting at 830nm. The light from the optical fiber is collimated and refocused into a beam with a long depth of focus and a 60μm beam waist diameter. The parallel beam is passed through an X-Y scanning system which is programmed to produce a 3mm annulus. The annulus is placed incident on the test lens (Figure 4.3). The refractive power of the test lens focuses the annulus into a spot. Similar to the first generation Scheiner system, a camera mounted on a vertical translation stage is positioned behind the testing chamber, at the location of convergence of the annulus. This location corresponds to the focal plane of the lens. The back vertex refractive power of the lens immersed in the testing chamber is calculated using a formula derived from a paraxial optical model of the system. This system is able to directly measure the distance from the back vertex of the lens to

the focal plane from the OCT cross sectional images of the lens. This optical system was calibrated on the same plano-convex lenses in the range of 12 to 53 D. The system had a measurement error ranging from -1.6D to +1.9D.

A.

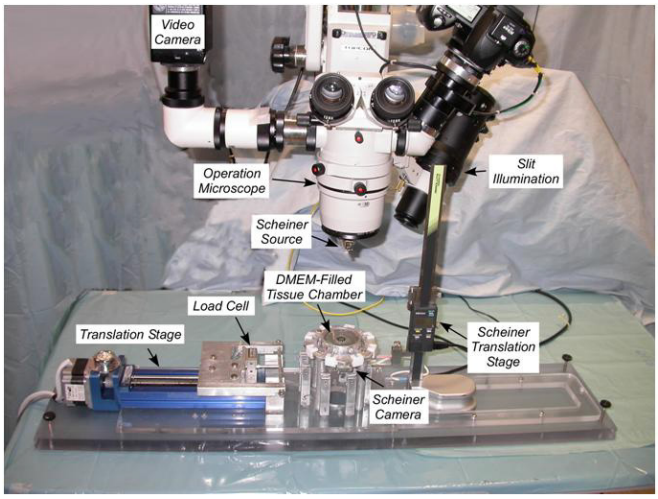

B.

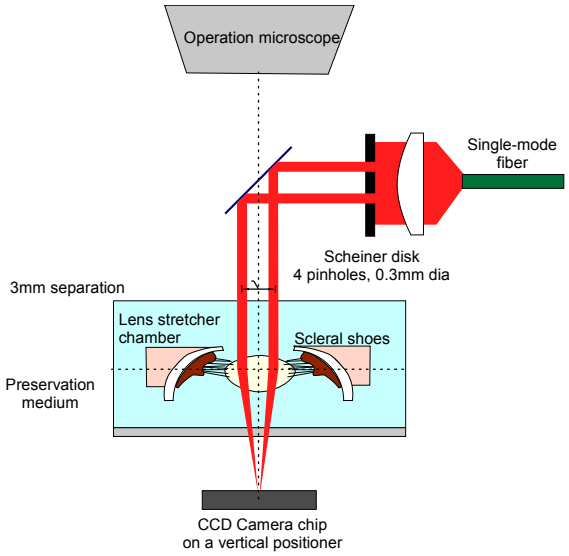

C.

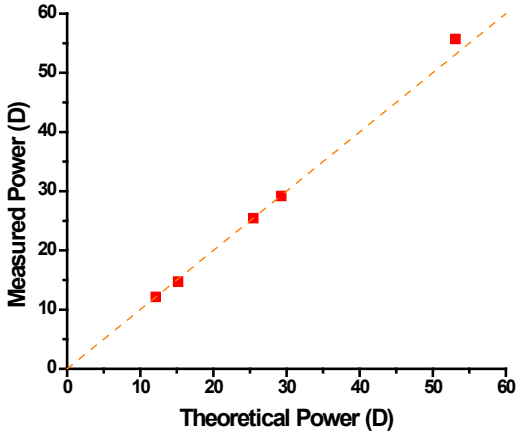

Figure 4.2: A. In vitro lens power measurement with a Scheiner system (Manns et al 2007). B. Four parallel beams are directed by a 45° mirror into the vertical direction coaxially with the optical axis of the in vitro lens. A CCD chip mounted on a vertical position is used to visualize and record the location of the focus. C. Calibration on glass lenses submerged in water produced power measurements that were within -1.8D to 2.9D of the manufacturer specifications.

A.

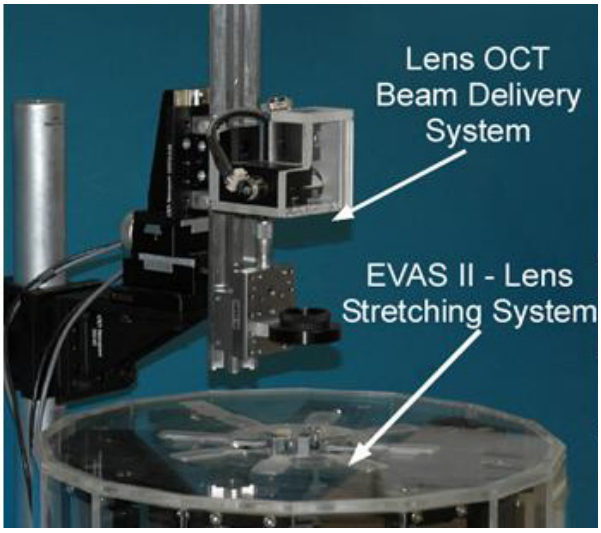

B.

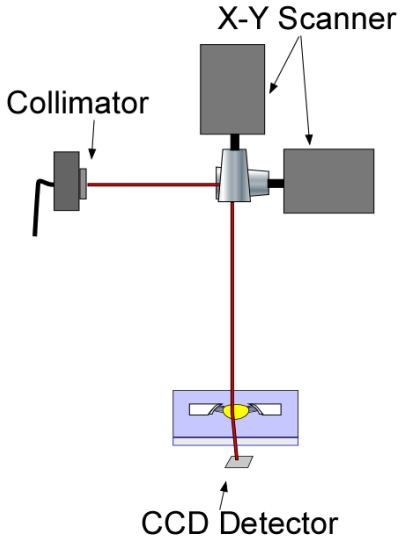

C.

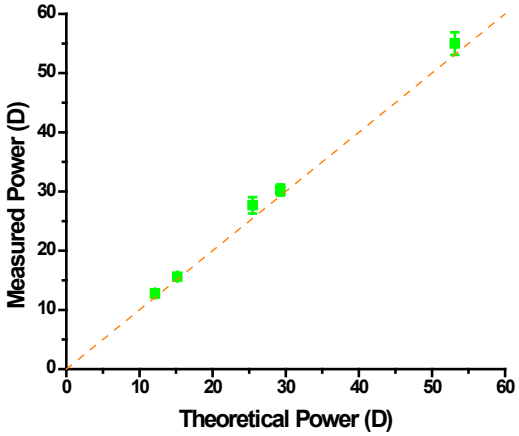

Figure 4.3: A. The OCT beam delivery system used as a light source for EVAS II power measurements. B. The X-Y scanners are programmed to deliver a 3mm diameter parallel ring onto the lens. The annulus is focused by the refractive power of the lens. A CCD camera on a vertical translation stage is used to detect the location of the focus. C. Calibration on glass lenses submerged in water produced power measurements that were within -1.6D to +1.9D of the manufacturer specifications.

4.2.4. A custom designed lensmeter based on the Badal principle

The three previous lensmeter systems were designed for either isolated lenses or lenses mounted in a lens stretching system. Several human lenses from older donors could not be measured due to light scattering caused by cataracts which significantly increased the spot size and reduced the measurement precision. An optical system was developed specifically to measure refractive power of highly scattering lenses. This lensmeter system was designed based on the Badal principle (Bennett and Rabbets 1998).

The custom-built Badal lensmeter was designed to measure excised as well as partially dissected monkey and human lenses with an entrance pupil diameter of 3.0 mm. Figure 4.4 shows a graphical representation of the Badal measurement system. The system collimates the image of a multi-mode optical fiber with a projection lens and produces an image of the fiber tip onto a CCD beam profiler camera. A specially designed immersion cell is used to place the isolated lens in the collimated beam path at the back focal plane of the projection lens. The refractive power of the test lens defocuses the image of the fiber on the CCD beam profiler. The image of the fiber is re-focused onto the CCD beam profiler camera by increasing the distance (x) from the tip of the fiber to the projection lens. The optical power of the test lens is proportional to the squared power of the projection lens and the distance from the object (x) (Bennett and Rabbets 1998):

$$P_{\text{Test Lens}} = x \cdot P^2_{\text{Projection Lens}} \qquad \text{Eq. 4.5}$$

where x is the displacement of fiber required to re-focus the fiber tip on to the camera, P_{TestLens} is the power of the test lens, and $P_{\text{ProjectionLens}}$ is the power of the projection lens.

A.

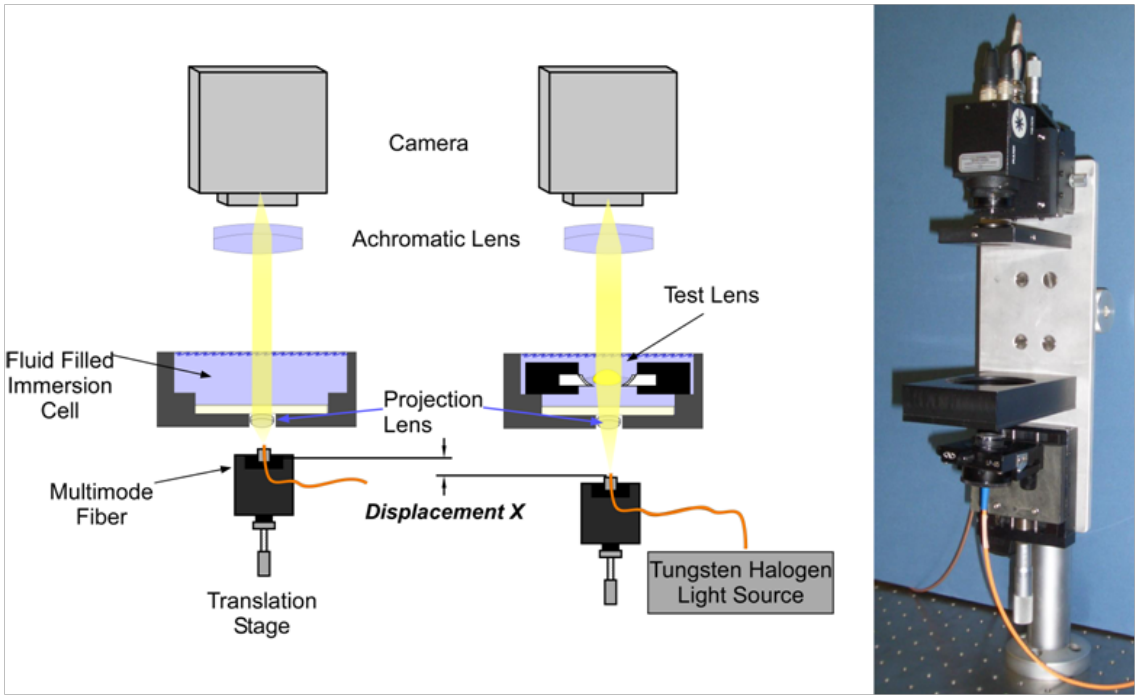

B.

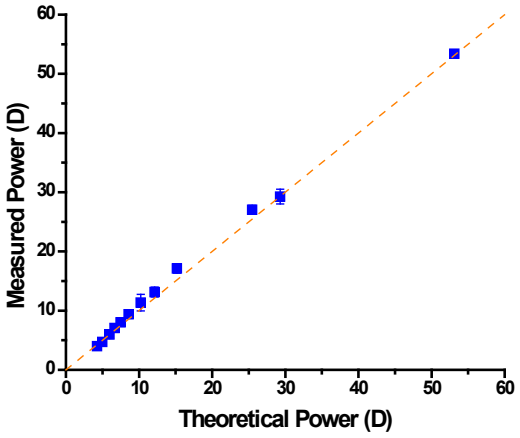

C.

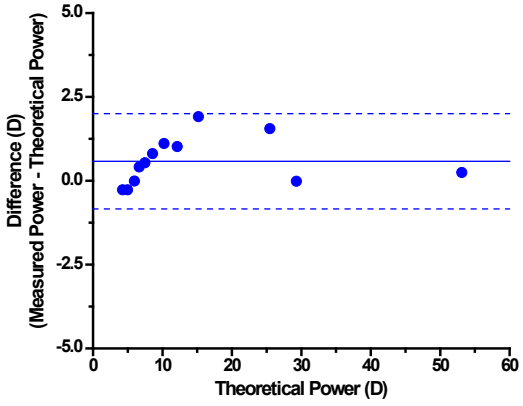

Figure 4.4: A. Optical layout of the custom-built Badal lensmeter. Light from an optical fiber is collimated by a high power projection lens and the light source is re-imaged onto the camera by an achromatic lens. The image of the light source is defocused when a test lens is placed in the system. The displacement (X) of the light source needed to re-focus the image of the fiber onto the camera is related to the optical power of the test lens by Eq. 4.5. The refractive power measurement (B.) and measurement error (C.) of the system for a set of plano-convex calibration lenses.

4.2.5. Calibration and comparison of lensmeter performance

To compare the three systems, a Bland-Altman analysis was performed on 17 human (age: 26 to 82 years; average age: 54 years) and 13 cynomoglus monkey (age: 2.7 to 11 years; average age: 7.7 years) in vitro crystalline lenses where one eye was measured with the commercial lensmeter and the Badal lensmeter and the contralateral eye was measured with the EVAS I Scheiner lensmeter system. The mean measurement difference between the commercial lensmeter and the Scheiner lensmeter was 1.1 ±2.2 D with the commercial lensmeter providing the higher average value (Figure 4.5). The mean measurement difference between the commercial lensmeter and the Badal lensmeter was 0.56D ± 2.0D with the commercial lensmeter providing the higher average value. This difference is within the expected accuracy and variability of the measurements on in vitro crystalline lenses.

A.

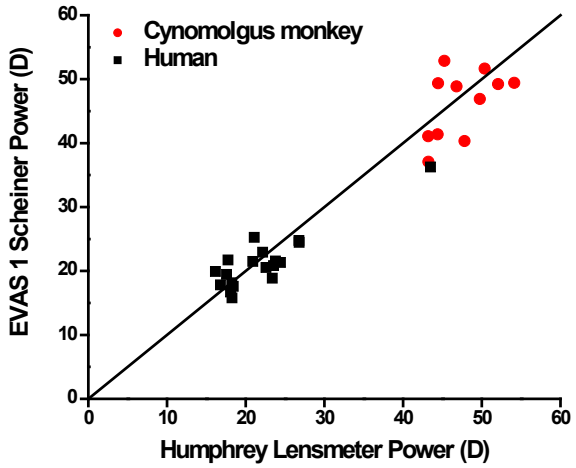

B.

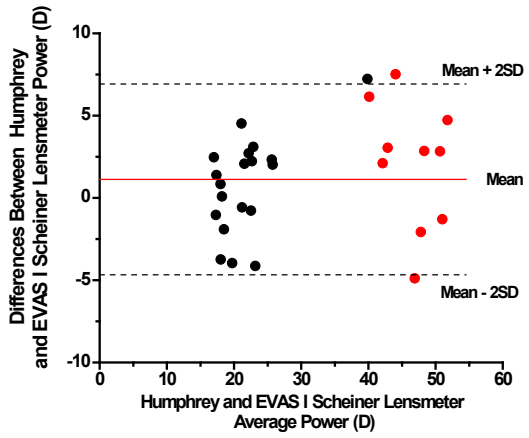

C.

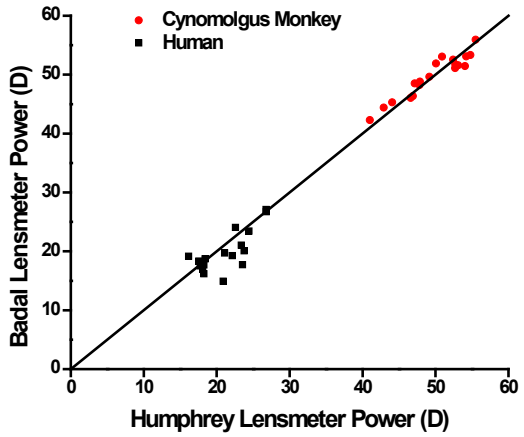

D.

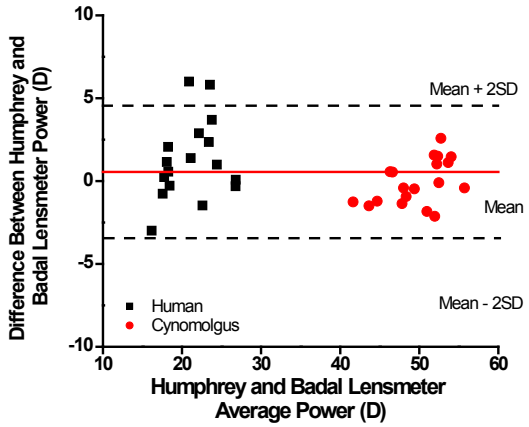

Figure 4.5: (A.) A comparison of *in vitro* crystalline lens optical power measurements obtained from the EVAS I Scheiner system and the Humphrey lensmeter. (B.) A Bland-Altman analysis of 17 pairs of human lenses and 13 pairs of cynomolgus monkey lenses were one lens was measured with the commercial lensmeter and the contralateral lens was measured in the custom Scheiner lensmeter. Most of the measurements were within two standard deviations of the mean measured power value. (C.) A comparison of in vitro lens optical power measurements obtained with the Badal lensmeter and the Humphrey lensmeter. (D.) A Bland-Altman analysis depicting the difference between the Badal and the Humphrey lensmeter measurements. This analysis shows all three systems produce comparable results.

4.3. In vitro lens shape measurements

4.3.1. General description

In this project three techniques were developed for or applied to in vitro lens shape measurements. The first technique, shadowgraph imaging, allows for undistorted profile images of the lens and is well established for in vitro lens shape measurements (Rosen et al 2006). The second technique utilizes a custom designed time-domain optical coherence tomography (OCT) system to produce cross-sectional images of the lens (Uhlhorn et al 2008). Custom image processing software was written to obtain lens shape information from the OCT images. The final technique utilizes the Scheimpflug principle to create an image of the lens cross sectional profile. The three techniques are described in the following sections.

4.3.2. Shadowgraph imaging

Shadowgraph images are magnified projected images of an object profile created with the use of an optical comparator. An optical comparator is an optical system, usually used in industry, for the inspection of machined parts. An optical comparator produces undistorted magnified views of the object profile on a viewing screen using a telecentric optical projection system. A commercially available optical comparator (Figure 4.6, Topcon BP-30S, Tokyo, Japan) was modified to allow for profile imaging of tissue samples maintained in a preservation medium (Denham et al 1989). This modified optical comparator has been used in the past to image corneal tissue samples and isolated crystalline lenses (Pflugfelder et al 1992, Denham et al 1989, Rosen et al 2006, Augusteyn et al 2007).

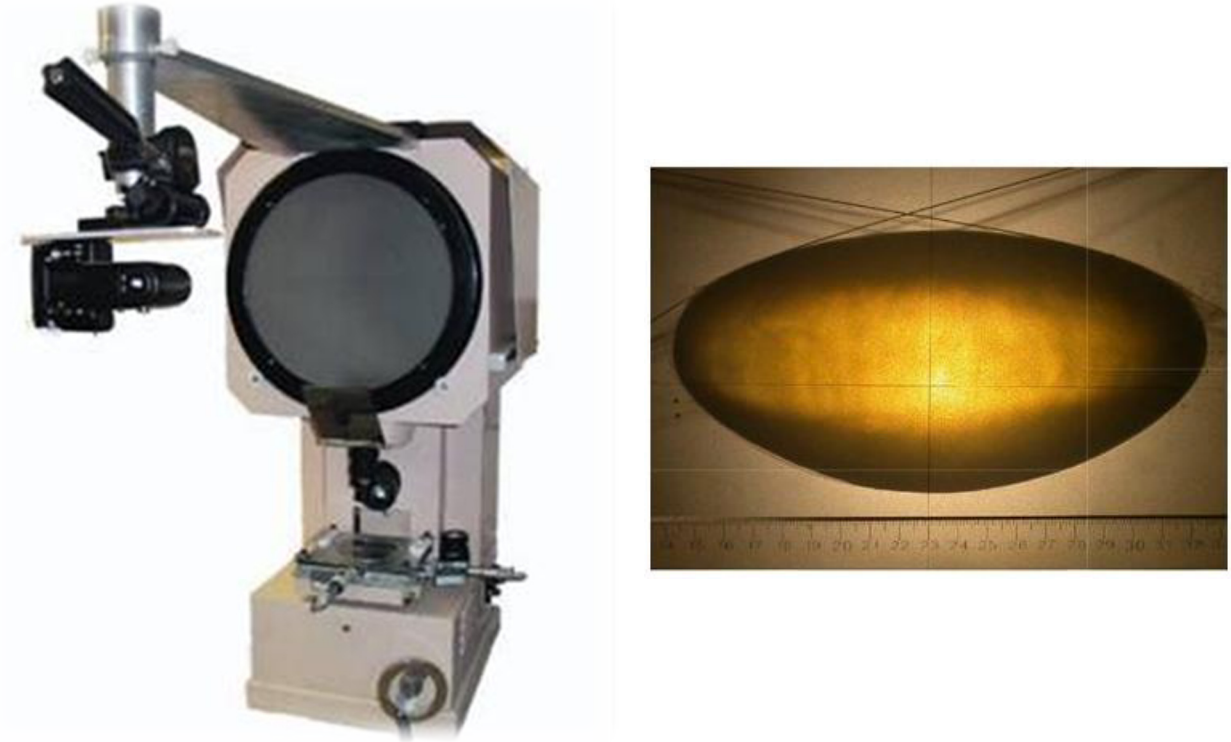

Figure 4.6: Non-contact biometric measurements were obtained from a customized optical comparator (Topcon BP-30S, Tokyo, Japan). Images of the sagittal views of the lens were acquired with a 4.0Mp Nikon Coolpix 4500 digital camera (Tokyo, Japan). For calibration purposes, a drafting ruler with 1:1 cm scale (1376T-25, Keuffel & Esser Co., Hoboken, New Jersey) was included in each digital photograph. The resolution of the camera and the 20x magnified projected comparator images provided an image resolution of approximately 12μm/pixel. Since the resolution depends on how much lens profile fills the image, optical zoom was used until the camera's view was completely filled by the lens profile on the screen. Commercial imaging software (Canvas 8.0, Deneba Software, Miami, FL) was used to digitally measure the lens anterior, posterior and total thickness in the sagittal lens profile images.

In this study, digital shadowgraph images of isolated crystalline lenses were recorded at 20X magnification (Rosen et al 2006). During these measurements the lens was positioned in an immersion chamber filled with Dulbecco's Modified Eagle's Medium (DMEM). DMEM is an organ culture medium which has been shown to preserve the hydration state of isolated crystalline lenses (Auguysten et al 2007). The lens was supported by a meshwork of 10-0 nylon monofilament sutures. The central lens thicknesses (t) and equatorial diameter (d), as well as the anterior and posterior surface profiles, were obtained from the shadowgraph images (Figure 4.6).

The surface profiles were fit with conic functions (Figure 4.7, Eq. 4.6) over the central 6mm zone to calculate the radii of curvatures (R) and asphericities (Q) (Rosen *et al,* 2006 and Manns *et al*, 2004):

$$z = z0 - \frac{(x - x_0)^2}{R + \sqrt{R^2 - (Q+1)(x - x_0)^2}} - f_3(x - x_0)^3 \qquad \text{Eq. 4.6}$$

where z and x are the axial height and radial position of the lens surface, respectively, z_0 and x_0 are the axial and radial shifts of the conic section with respect to the origin of the coordinate system, R is the apex radius of curvature, and Q is the asphericity of the conic section. The third-degree term in x (f_3) was added to account for potential asymmetry of the lens surface. In previous studies this term increased the accuracy of curve fits at the periphery of the lens (Manns et al 2004, and Rosen et al 2006). For the purpose of optical modeling it is convenient to describe the lens surfaces with a conic section such as in Eq.4.6. The asphericity, Q is a continuous variable which determines the type of conic section: hyperbola, parabola, sphere or an ellipse (Figure 4.8).

A.

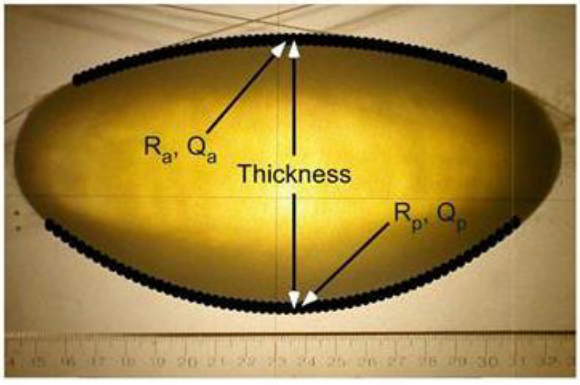

B.

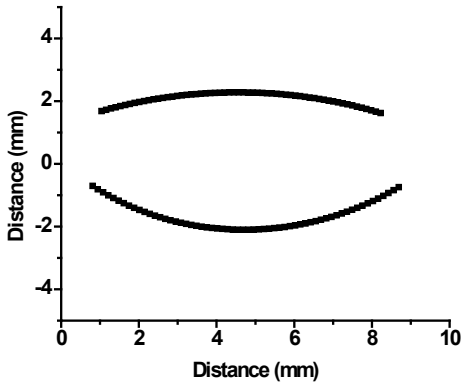

Figure 4.7: (A.) A sample image of a sagittal view of a human lens with an overlay of the detected and fit surface profiles. A program was written in Matlab to fit conic sections to the lens surfaces in the digital photographs. A custom Canny edge detection algorithim written in Matlab (R14, Mathworks, Inc., Natick, MA) detected anterior and posterior lens profiles on the sagittal view shadowgraph images. (B.) The output of this edge detection algorithim was an ordered pair corresponding to the axial and radial positions of the anterior and posterior lens surfaces.

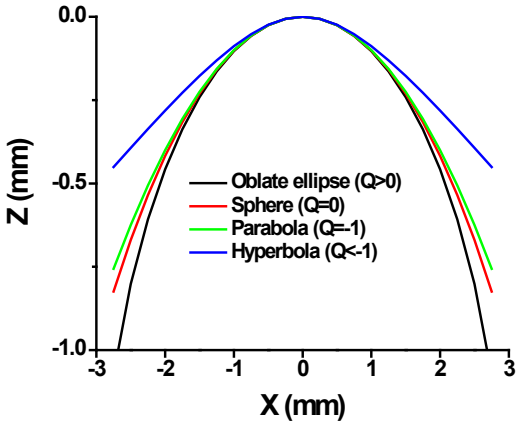

Figure 4.8: The aspheric surfaces of the lens can be described by a conic section given by equation Eq. 4.6. The value of the parameter Q determines the type of conic section:

- a hyperbola when $Q < -1$;
- a parabola when $Q = -1$;
- a prolate ellipse when $-1 < Q < 0$;
- a circle when $Q = 0$;
- and an oblate ellipse when $Q > 0$.

When $Q < 0$: the curvature is highest at the apex and decreases toward the periphery (prolate conic section). When $Q > 0$: the curvature is lowest at the apex, and increases toward the periphery (oblate conic section).

The accuracy and precision of the measurement and analysis technique was quantified using a stainless steel ball bearing with a radius of curvature of 4.763 mm, (asphericity of Q=0 for a sphere). The measured apex radius was 4.722 mm and the shape factor was p=0.95. This corresponds to a measurement error of 0.87 % for the radius measurements and 5 % for the shape factor measurements.

4.3.3. Optical coherence tomography

4.3.3.1. General description

A custom designed time-domain OCT system was developed at the OBC for cross-sectional imaging of the lens during simulated accommodation in the EVAS II lens stretcher (Uhlhorn *et al,* 2008). The system consists of a superluminescent diode (SLD) with an 825 nm central wavelength and a 25 nm bandwidth, a fiber-optic interferometer and a scanning delay line with a tele-centric beam delivery system (Uhlhorn *et al,* 2008) (Figure 4.9). The system produces axial a-scan interferograms at a rate of 20A-lines/s with a resolution 12 μm in the axial direction. The system has an axial scan length in air of 10 mm air and in 7.1 mm water. A

custom digital image processing program was written to read, filter and convert the 500x5000 64bit A-scans to produce 8 bit gray scale images with the proper aspect ratio and square pixels. A custom written edge detection program was written and used to detect the contours of the lens surfaces and to measure the lens thickness and diameter. The resulting anterior and posterior lens surface profiles were fitted with a conic function (Equation 4.6) to obtain anterior and posterior radii of curvature (R) and asphericities (Q).

The OCT system allows for measurements of isolated lenses shape as well as lenses mounted in the EVAS II lens stretching system. During lens stretching experiments the OCT system also provides measurements of the position lens surface with respect to the cell window. This distance is used to calculate the back vertex power of the lens (Figure 3.1).

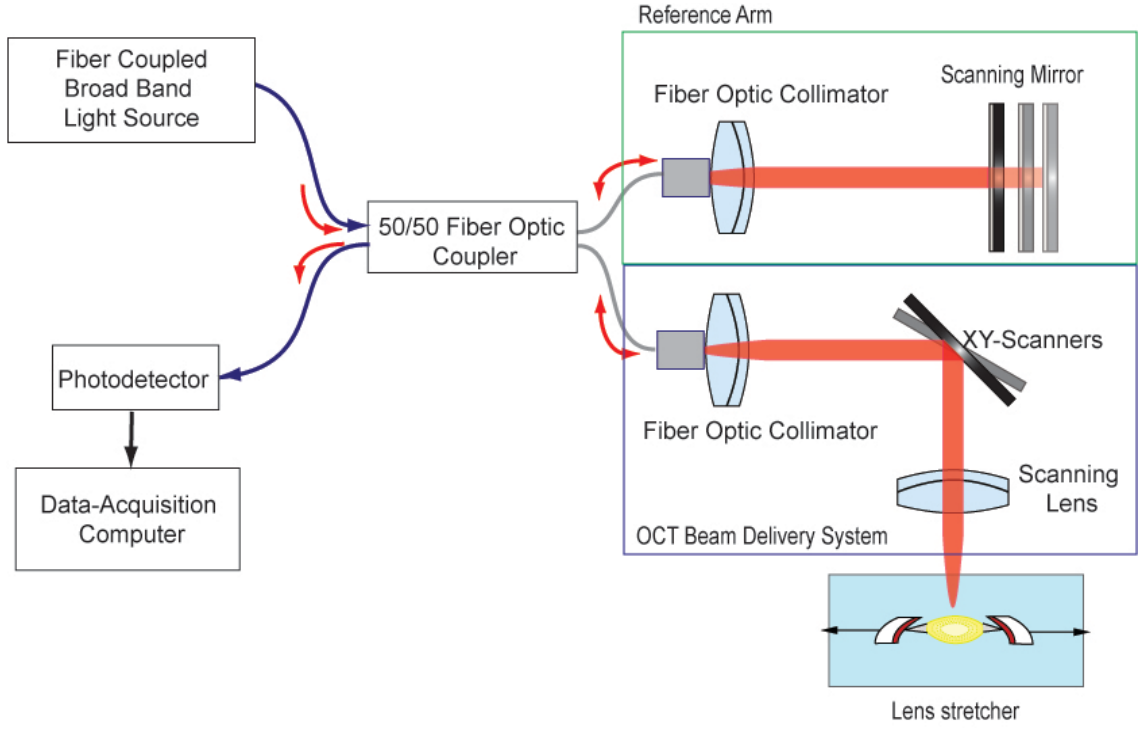

Figure 4.9: Optical schematic of the lens OCT system. Light from a fiber coupled superluminescent diode is split equally into a reference arm and a sample arm. The sample arm is composed of the beam delivery optics and XY scanners. The light from both the reference arm and the sample arm return to the fiber optic coupler and travel to the photodetector. An interference signal is detected by the photodetector when the optical path length of the reference matches that of the sample arm. The data acquisition computer samples the photodetector and builds up the OCT image.

4.3.3.2. Refractive distortions during OCT imaging of the in vitro lens

A paraxial optical analysis was performed to determine the error induced by refractive displacement of the OCT beam caused by refraction at the anterior lens surface. During time-domain OCT imaging an image is generated one A-line at a time similar to an ultrasound technique. Each A-line is generated along the direction of the incident OCT beam (Figure 4.10). The refractive properties of the crystalline lens cause refraction of the incident OCT beam. The paraxial angle of refraction θ' of the OCT beam can be solved by the geometric refraction equation:

$$n'\theta' - n\,\theta = -hPa \qquad \text{Eq. 4.7}$$

where θ and θ' are the incidence and refraction angles of the OCT beam at the anterior lens surface, n is the refractive incidence of the surrounding medium (n=1.336), n' is the refractive index of the lens, h is the entrance beam height and Pa is the refractive power of the anterior lens surface:

$$Pa = \frac{n' - n}{Ra} \qquad \text{Eq. 4.8}$$

where Ra is the lens anterior surface radius of curvature. With the telecentric design, the entrance beam is normal to the lens optical axis (θ=0). If we assume all of the refraction occurs at the anterior lens surface (that is $n'=n_{eq}=1.42$) we find:

$$\theta' = \frac{-hPa}{n_{eq}} = -\frac{h(n_{eq} - n)}{R_a \cdot n_{eq}} \qquad \text{Eq. 4.9}$$

From Figure 4.10 it can be seen that the ray displacement in the x and y directions are given by:

$$\Delta y = t \cdot \cos\theta' - t, \text{ and } \Delta x = t \cdot \sin\theta' \qquad \text{Eq. 4.10}$$

In the paraxial region we can use the small angle approximation ($\sin\theta = \theta$ and $\cos\theta = 1$) to simplify equation 4.10:

$$\Delta y = 0, \text{ and } \Delta x = t \cdot \theta' \qquad \text{Eq. 4.11}$$

The values of these displacements for typical human and monkey lens shapes assuming a thickness of 4.5mm (worst case scenario) are shown in Figure 4.10. These figures show that the distortions are within the spatial resolution of the OCT system except at the periphery of the lenses with the steepest anterior surface.

A.

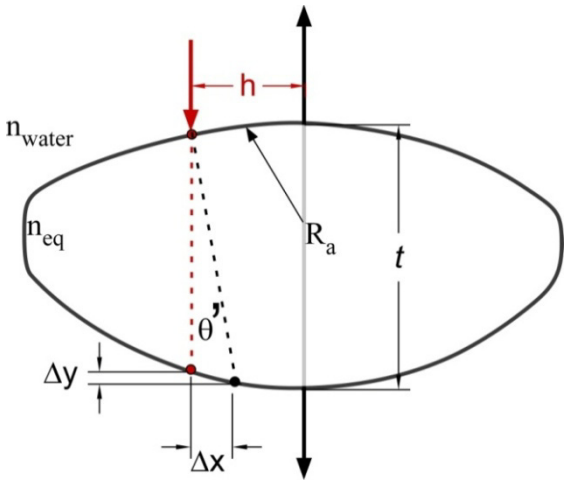

B.

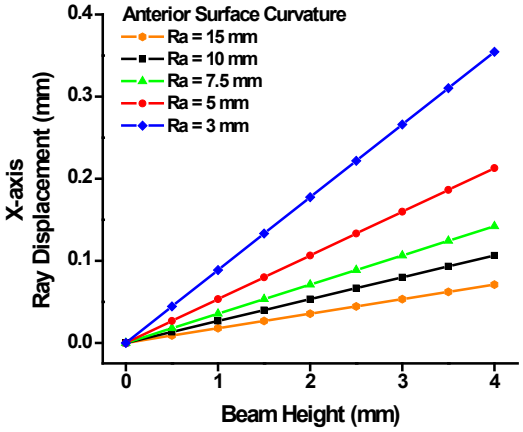

C.

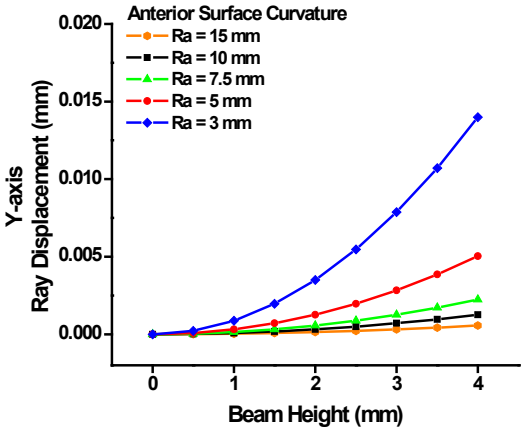

Figure 4.10: Error analysis of refractive distortions during OCT imaging of an in vitro crystalline lens. The analysis was performed for an in vitro lens in water (n=1.336) with equivalent refractive index of 1.42 and a central lens thickness of 4.5 mm. The anterior lens surface radius of curvature was varied from 3 to 15mm. The entrance beam height was varied from 0 to 4 mm. The OCT beam (parallel to the optical axis) was refracted by the anterior lens surface. The OCT beam displacement in the x (B.) and y (C.) directions were plot as a function of entrance beam height. This analysis represents a worst-case scenario because it assumes an extreme thickness and assumes that all of the refraction occurs at the anterior lens surface. Even with these assumptions the distortions are near spatial resolution of the system except at the periphery of the steepest lenses (3 and 5mm).

To confirm that distortions are negligible, a study on 15 human and was performed to assess the OCT cross-sectional image distortions induced during in vitro lens biometry. OCT cross-sectional images were obtained on isolated human and cynomolgus monkey lenses. The lens cross-section was first imaged through the anterior lens surface (Anterior-Up OCT). The lens was then flipped over and the lens cross-section was then imaged through the posterior lens surface (Posterior-Up OCT). For comparison the undistorted cross-sectional profile images of the same group of crystalline lenses were measured using an optical comparator which projects an undistorted magnified profile image of the lens. The anterior and posterior surface profiles were obtained from each image using an edge detection algorithm and fit with a conic section function to determine the radii of curvature and asphericity of the lens surfaces. Any significant optical distortions of the lens surfaces during OCT imaging would result in measurable differences in radii of curvature results obtained from the OCT system and the shadowgraph technique.

A one-way analysis of variance (One-way ANOVA) was performed to determine if there were any significant differences on the measured thickness, anterior and posterior radii of curvature from the three different measurement techniques (Shadowgraph, Anterior Up-OCT, and Posterior Up-OCT). Bland – Altman statistical analysis was performed to determine any systematic dependencies on the differences between the results obtained from the Shadowgraph and the two OCT techniques. The Bland-Altman analysis plots the difference between the measurement values obtained with two different techniques as a function of the average measurement values (Figures 4.11 and 4.12).

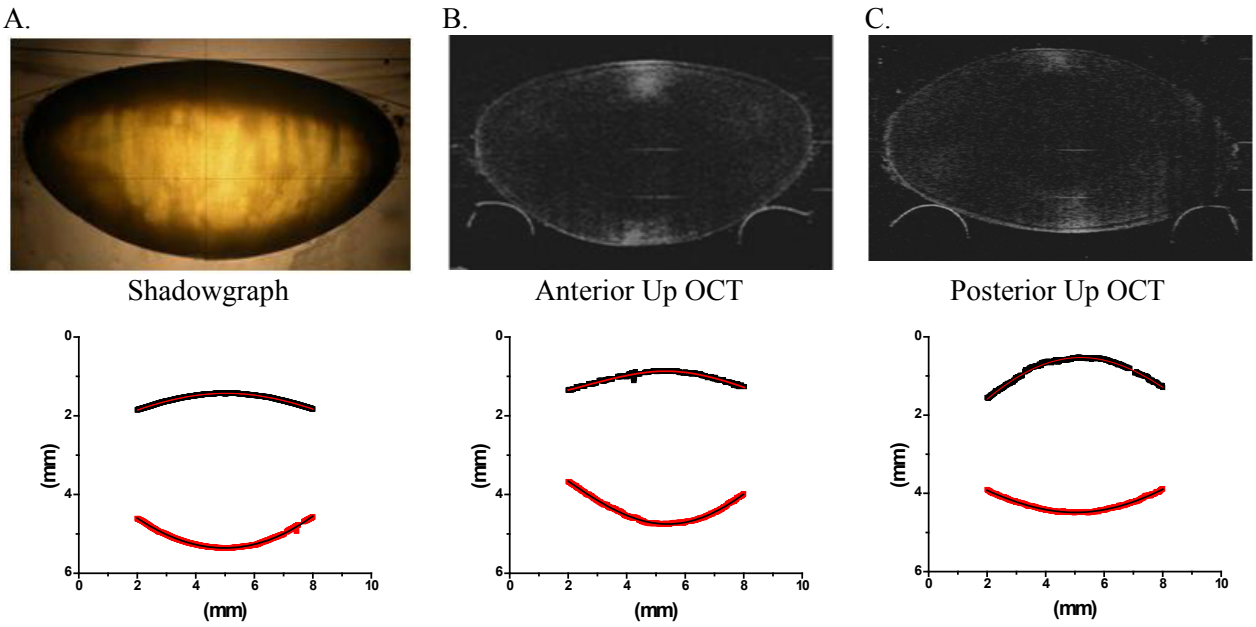

Figure 4.11: Example shadowgraph and OCT images of a 41 year old human crystalline lens (PMT= 96 hours). Radii of curvature measurements from the undistorted shadowgraph images (A.) were compared with those from OCT images. OCT images were taken in two orientations one with the anterior surface (B.) facing the incoming beam and one with the (C.) posterior surface facing the incoming beam.

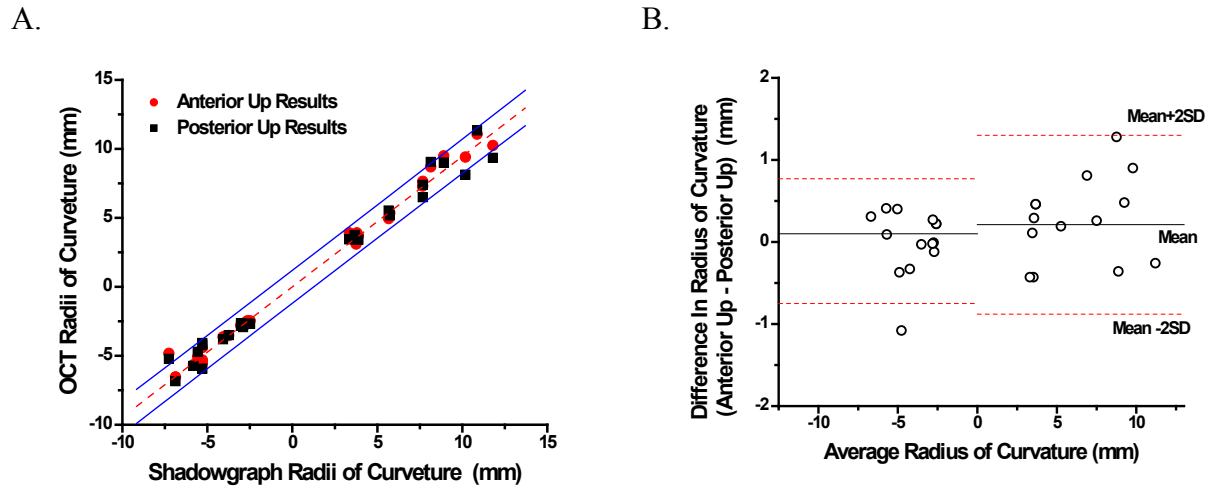

Figure 4.12: (A.) Radii of curvatures were measured with the OCT and the Shadowgraph system on 15 lenses human cadaver lenses. (B.) A Bland-Altman analysis demonstrated that most of the surface curvature measurements were within 2 standard deviations of the mean measurement error. The mean measurement error was 0.21 ± 0.55mm for the anterior surface and 0.01 ± 0.38 mm for the posterior surface. These results indicate both the shadowgraph system and the OCT system accurately measure the undistorted shape of the isolated crystalline lens.

The analysis of variance demonstrated that (at the p=0.05 level) the mean radii of curvature measurement results are not significantly different between the shadowgraph and OCT techniques. The results of the OCT and Shadowgraph comparison study (Figures 4.11 and 4.12) validate the use of OCT imaging as an accurate technique for in vitro lens biometry.

4.3.4. Scheimpflug Imaging

The first generation EVAS system utilizes a slit-lamp illumination and operation microscope for imaging of the lens cross-section. In this slit-lamp system the lens cross section is illuminated by a thin slit of light (Figure 4.13). The obliquely illuminated cross-section of the lens is imaged by a microscope system. The limited depth of focus of the microscope and the illumination system does not allow for simultaneous and sharp imaging of the anterior and posterior lens surfaces. In addition the standard slit-lamp illuminates the lens obliquely. The microscope therefore does not image a meridional plane and it is not possible to accurately measure the lens shape. A Scheimpflug slit-lamp microscope system is proposed as a solution which could improve the depth of focus allowing for simultaneous sharp imaging of the anterior and posterior lens surfaces (Figure 4.14). The system requirements are high resolution digital images of the central lens cross section acquired at video frame rates from which accurate measurements of the lens shape (thickness, radii of curvature and asphericities) can be made during simulated accommodation.

A.

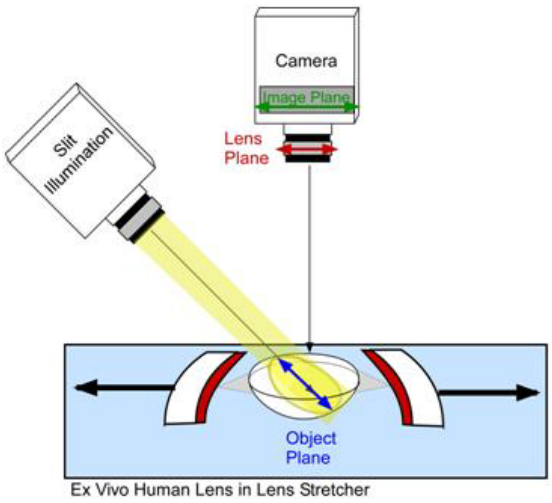

B.

Figure 4.13: A. The first generation EVAS system created an obliquely illuminated cross section of the lens. An operational microscope system with a video camera produced images of the lens with a limited depth of focus. B. A sample slit-illuminated image of a human crystalline lens during simulated accommodation in the first generation EVAS system.

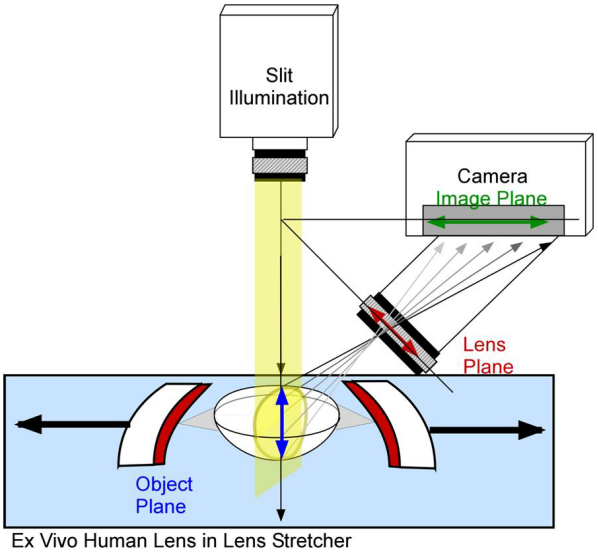

Figure 4.14: Diagram of the Scheimpflug system for cross sectional imaging of the lens during simulated accommodation. The system consists of a slit lamp illumination system, a digital camera and a lens system. A co-axial slit illumination system illuminates a central cross-section of the lens mounted in the second generation lens stretcher system. Images are acquired with an oblique digital camera. The illumination, lens and camera system together satisfy the Scheimpflug principle. A detailed description of the design and development of the Scheimpflug system is given in chapter 5.

Chapter 5 describes the design and development of the Scheimpflug imaging system for cross sectional imaging of the ex vivo lens during simulated accommodation. Figure 4.15 presents sample uncorrected Scheimpflug images of lenses from a 39 year old human (2 days post mortem), a 3 year old hamadryas baboon (1 day post mortem) and an 8 year old cynomolgus monkey (3 hours post mortem). The tissue samples were prepared by attaching (with cynoacrylate glue) the whole globe onto an aluminum annulus ring. The Scheimpflug system was focused on the central cross section of the in vitro lens.

A.

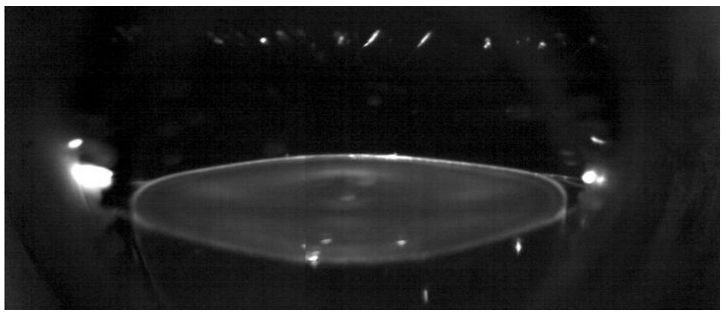

B.

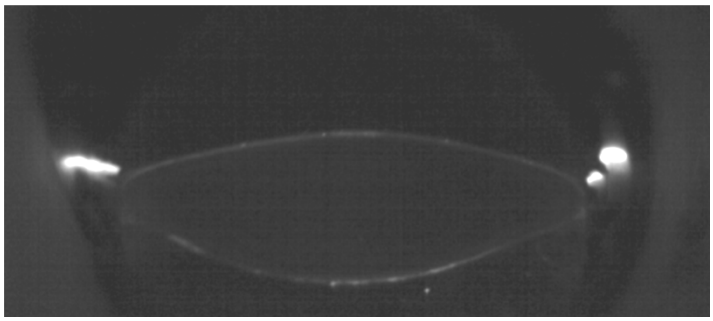

C.

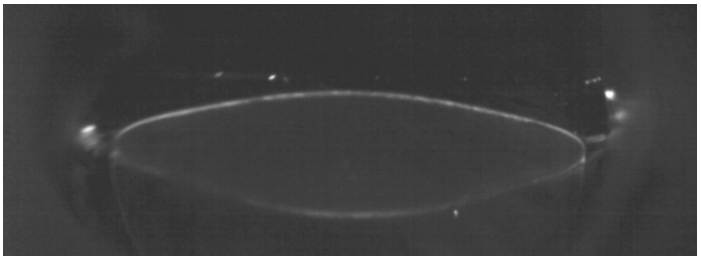

Figure 4.15: Sample Scheimpflug images of a human lens (A.) (Age= 39 years, post mortem time = 2 days) a hamadryas baboon lens (B.) (Age=3 years, post mortem time = 1 day) and a cynomolgus monkey lens (C.) (7.5 years old, 3hours postmortem).

4.4. Optical Modeling

4.4.1. Purpose

The devices described in the previous sections measure the lens shape and power. To derive the contribution of the lens gradient from these measurements optical models must be developed. The following sections describe the development of these optical models.

4.4.2. Contributions of surface refraction to total refractive power

The refractive contributions of the lens aspheric surfaces were quantified by calculating the power of each measured lens assuming a uniform refractive index equal to the cortex refractive index. Based on the data of Jones et al using MRI, the age-independent refractive index of the cortex was assumed to be n=1.3709 (Jones et al 2005) independent of age. The calculations were performed with a commercial optical ray tracing software (OSLO LT, Lambda Research, Littleton, MA). The ray tracing simulation incorporated isolated crystalline lens thickness, surface curvatures and asphericity measurements obtained using the OCT, Scheimpflug or shadowgraph technique. The refractive index of the surrounding medium (DMEM) was assumed to be equal to the refractive index of water (n_{DMEM}=1.334 at 635nm). To simulate the experimental conditions, a ray with a height of 1.5mm (Scheiner and Badal) or 2.24mm (commercial lensmeter) was traced entering the lens. The position of the focal plane was determined by the location of the intersection point of the ray with the optical axis (Figure 4.16).

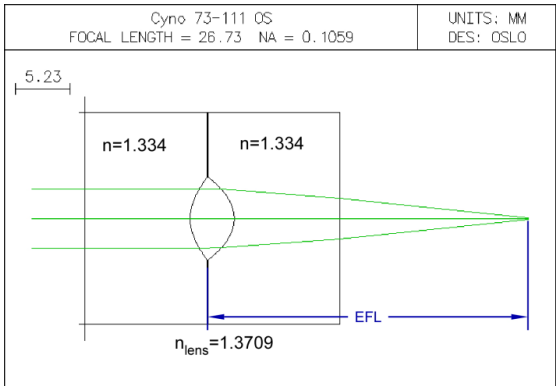

Figure 4.16: Optical ray tracing simulation used to evaluate the refractive power of the isolated lens aspheric surfaces assuming a refractive index of 1.3709 for the surfaces and 1.336 from the aqueous and vitreous.

4.4.3. Equivalent refractive index

The equivalent refractive index (N_{eq}) is defined as the uniform refractive index value that is required inside the lens to provide a power equal to the actual crystalline lens power if all other parameters (radii of curvatures, surface asphericities and central thickness) remain constant. To calculate the equivalent refractive index for each lens an optical ray tracing simulation of the power measurement setups, incorporating the chamber and the measured lens biometric data (lens radii of curvature, asphericities and thickness) was performed with a commercial optical ray tracing software (OSLO LT). The refractive index of the simulated lens was adjusted iteratively until the power of the lens corresponded to the measured power (Figure 4.17).

The technique to calculate the equivalent refractive index was calibrated using a 61D plano-convex glass (SF5, n=1.6683) lens, a 36.7D plano-convex glass (BK7, n=1.5150) lens and a 19.2D plano-convex glass (BK7) lens. The shape of the lenses was measured from shadowgraph images following the same procedure as that of the isolated lenses. The refractive index calculated from the measured equivalent power, thickness, diameter and radius of curvature, was within 0.006 to 0.013 of the specified value at 635nm. An analysis of the sources of error shows that the error in the value of the refractive index comes mainly from the error in the power measurements.

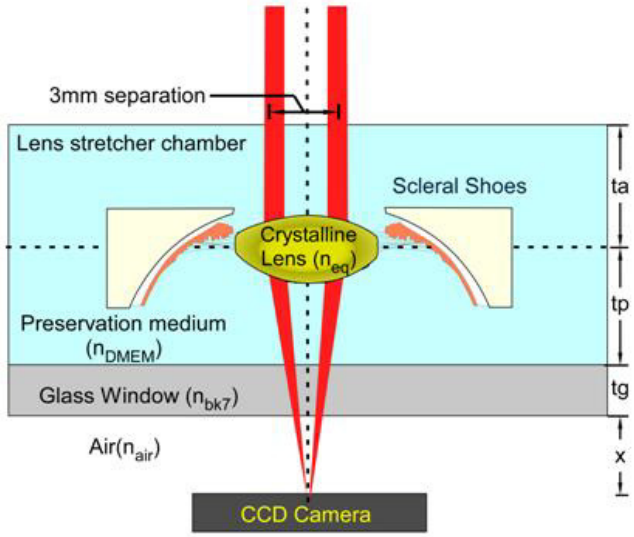

Figure 4.17: Optical ray tracing simulation used to evaluate an equivalent refractive index for the isolated lens measured with the Scheiner Principle. The simulation places a reference plane at the location of the measured focal length. An iterative process is used to determine an equivalent refractive index which would produce a lens with the measured optical power. Similar ray tracing simulations were conducted for the commercial lensmeter and the custom Badal lensmeter.

4.5. Summary

The goal of this dissertation is to develop an age-dependent optical model of the lens and its changes during accommodation. This optical model will be built on direct measurements of the lens shape and power in the isolated state free of external forces as well as during simulated accommodation in the EVAS lens stretching system. These measurements require the development of several lens shape and power measurement techniques as well as optical modeling techniques. In this chapter we described techniques which were developed for measurements of:

- isolated lens refractive power (using a custom Badal lensmeter and a modified commercial lensmeters)
- the isolated lens shape (using a shadowgraph technique)
- the refractive power of the in vitro lens during simulated accommodation (using a Scheiner system)
- the shape of the in vitro lens during simulated accommodation (using an OCT system and a Scheimpflug system)

- the refractive contribution of the lens surfaces and the internal refractive index gradient with an optical modeling technique.

In the next chapter we will describe the design and development of the Scheimpflug imaging system for acquisition of cross sectional images of the lens during simulated accommodation.

CHAPTER 5. EX VIVO LENS SCHEIMPFLUG IMAGING SYSTEM

5.1. Objective

This section describes the development of a custom designed Scheimpflug camera system for cross sectional imaging of the ex vivo lens during simulated accommodation.

5.2. General description

A Scheimpflug slit-lamp microscope system was designed to have sufficient depth of focus to allow for simultaneous imaging of the anterior and posterior lens surfaces (Figure 5.1) during ex vivo simulated accommodation. The goal is to obtain high resolution digital images of the central lens cross section acquired at video frame rates from which accurate measurements of the lens shape (thickness, radii of curvature and asphericities) can be made during simulated accommodation.

The design of the Scheimpflug system consists of:

- the optical and camera system design
- the slit-lamp Kohler illumination system design
- and the development of the Scheimpflug digital image correction algorithm

The design criteria include:

- a 10mm horizontal and a 15mm vertical field of view to provide images of the whole lens
- a working distance no less than 100mm to leave space for mounting the components
- a high resolution, high sensitivity digital camera
- a Kohler illumination system which creates a high intensity 100 μm wide by 15mm long focused rectangular beam of light with a 10mm depth of focus

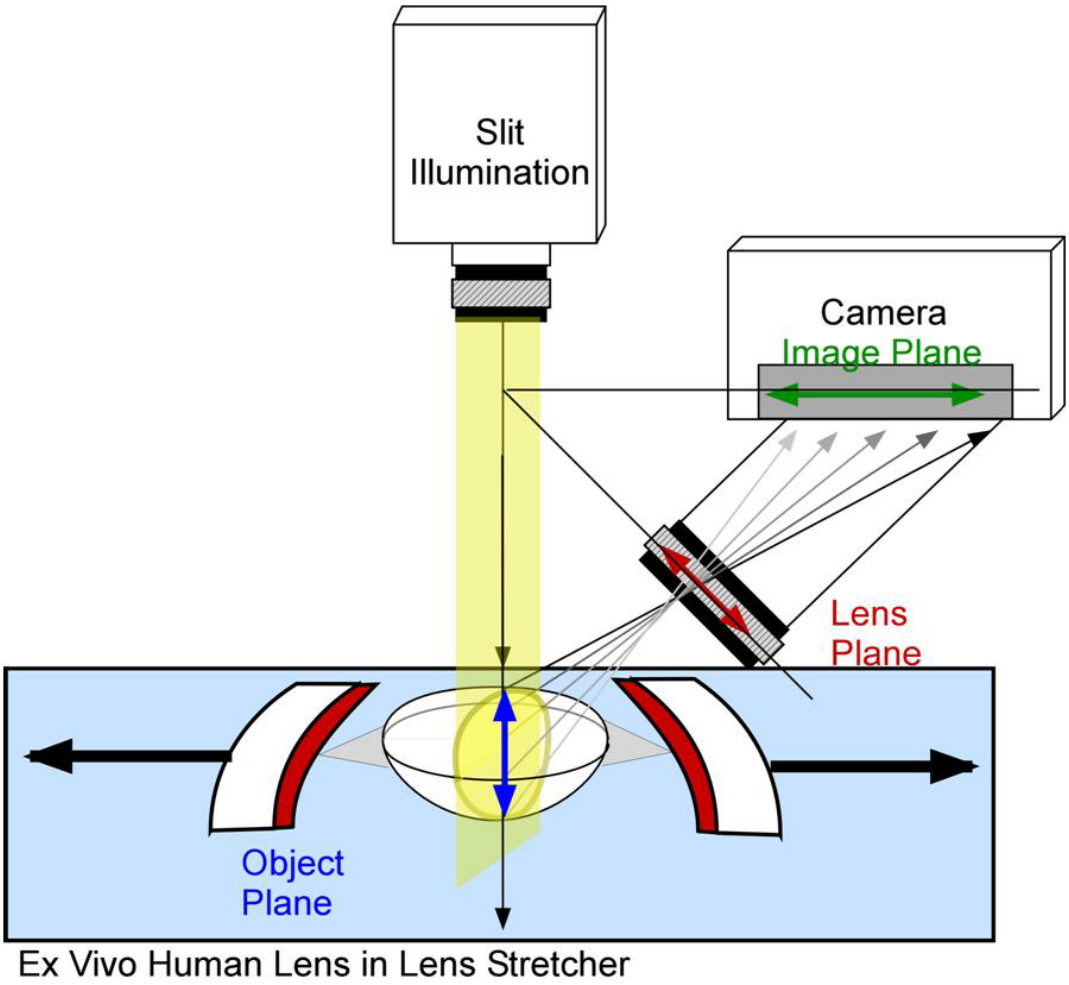

Figure 5.1: Diagram of the Scheimpflug system for cross sectional imaging of the lens during simulated accommodation. The system consists of a slit lamp illumination system, a digital camera and a lens system. A co-axial slit illumination system illuminates a central cross-section of the lens mounted in the second generation lens stretcher system (EVAS II). Images are acquired with an oblique digital camera. The illumination, lens and camera system together satisfy the Scheimpflug condition.

5.3. Design of the Scheimpflug imaging system

5.3.1. The Scheimpflug principle

The Scheimpflug principle is a photography technique used to maximize the depth of focus of a camera (Scheimpflug 1906). This technique has been applied to anterior segment imaging in the eye to produce sharp focused imaging of the entire anterior chamber (Figure 5.2.c). In the proposed system the Scheimpflug principle is utilized to create a sharp image of the ex-vivo lens anterior and posterior surfaces and the internal lens structure simultaneously.

Typically in an imaging system the object plane, lens plane and image planes are parallel to each other and normal to the optical axis. In this case the depth of field is a limited region defined by the range of object distances which produce an acceptable blur size in the image plane (Figure 5.2.a). According to the Scheimpflug principle, the depth of focus can be extended to a virtually infinite range by arranging the optical system in such a way that the image plane, lens plane or both are tilted with respect to the object plane and intersect at a common axis (Scheimpflug 1906) (Figure 5.2b). In this case the object plane and image plane are conjugate to each other. This technique was initially developed for surveying and imaging tall buildings. In the field of ophthalmology, this technique has been combined with slit-lamp microscopes for the purpose of simultaneous imaging of the cornea and the lens.

The Scheimpflug condition introduces distortion because the object distance varies object since the object plane is tilted with respect to the objective lens plane. A varying object distance produces a varying magnification. This distortion can be corrected by digital image post-processing. In addition, during Scheimpflug imaging of the lens, the position and shape of the posterior surface are distorted due to the refractive power of the anterior lens surface and the effect of the internal optics of the lens itself (Figure 5.2.c). Several investigators have shown that

it is possible to correct these distorted Scheimpflug images to obtain accurate quantitative values of the lens shape (Richards et al 1988, Dubbleman and Van der Heijde 2001).

A.

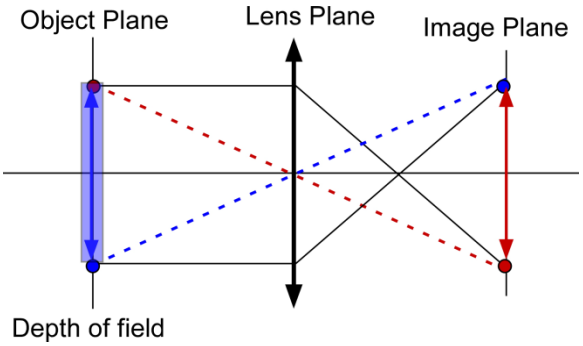

B.

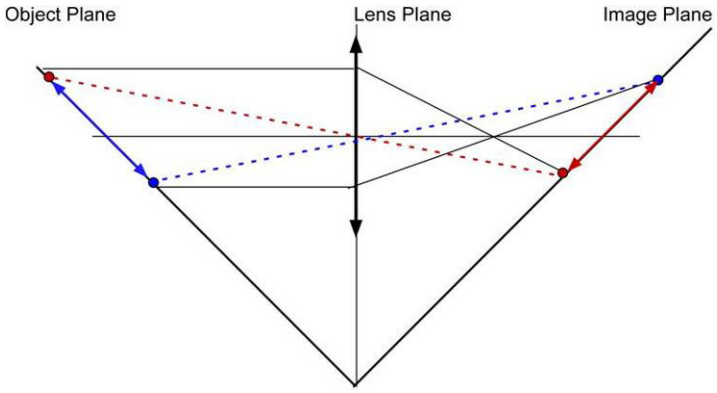

C.

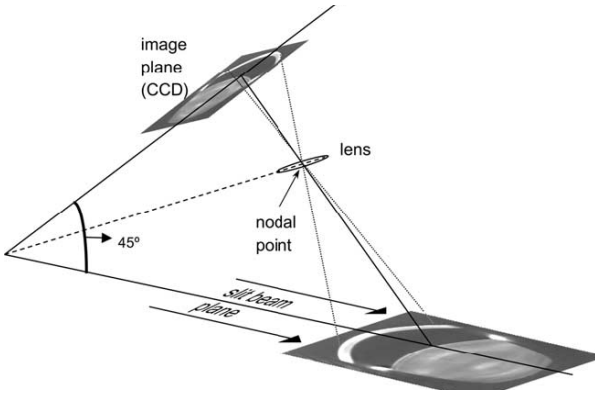

Figure 5.2: (A.) A ray tracing through a normal optical system. A ray tracing of the Scheimpflug principle (Smith 1966). This 2D representation demonstrates how a tilted object is rendered sharp when the object plane, the lens plane, and the image plane all meet at a single point. In the case of the Scheimpflug modified slit lamp, the object plane is illuminated by a thin slit beam. The tilted image and lens plane system creates a sharp cross sectional image from the cornea to the posterior lens surface (Dubbelman *et al,* 2005).

5.3.2. Derivation of the required Scheimpflug angle

In a Scheimpflug system, the object and image planes are tilted with respect to the objective lens (Figure 5.3). The first step of the optical design is to determine the values of the tilt angles of the object and image planes, α and β in Figure 5.3, as a function of the desired magnification. There are two different magnifications in a Scheimpflug system: the magnification between the two tilted planes and the magnification in the transverse direction.

The magnification (M_S) between the two tilted planes is equal to.

$$M_S = \frac{l'}{l} \qquad \text{Eq. 5.1}$$

Where l and l' are the object and image height measured in the direction of the tilted conjugate planes. The magnification in the transverse direction varies along the optical axis of the Scheimpflug objective lens. This magnification is equal to the lateral magnification M_V of the objective lens.

$$M_V = \frac{h'}{h} = \frac{s'}{s} \qquad \text{Eq. 5.2}$$

Where h is the lateral object height, h' the lateral image height, s is the object distance and s'is the image distance (Figure 5.3). For the point P_0, located on the optical axis of the imaging lens, the lateral magnification is equal to:

$$M_{V0} = \frac{h_0'}{h_0} = \frac{s_0'}{s_0} \qquad \text{Eq. 5.3}$$

From the geometry of Figure 5.3 we have:

$$h = l \cdot \cos\alpha \qquad \text{Eq. 5.4}$$
$$h' = l' \cdot \cos\beta$$

Which gives the following relation between the magnification in the tilted planes and in the transverse direction:

$$M_S = M_{V_0} \frac{\cos\ \alpha}{\cos\ \beta} \qquad \text{Eq. 5.5}$$

In addition from Figure 5.3 we have the following relation between the angles and the object and image distances:

$$\tan\alpha = \frac{s}{OD} \qquad \text{Eq. 5.6}$$
$$\tan\beta = \frac{s'}{OD}$$

Eliminating OD from these two equations gives the following relation between the transverse magnification and the two tilt angles:

$$M_V = \frac{\tan\beta}{\tan\alpha} \qquad \text{Eq. 5.7}$$

Equations 5.5 and 5.7 give the relation between the Scheimpflug angles and the desired magnifications. For any value of the tilt angle of the object plane and desired magnification these equations provide the value of the tilt angle of the image plane. In practice it is convenient to use object and image planes which are perpendicular to each other to facilitate mounting and fabrication. In that case we have:

$$|\alpha| + \beta = \frac{\pi}{2}$$

which gives:

$$\mathrm{M_V} = \tan^2\alpha$$
$$\mathrm{M_S} = M_{V_0} \cdot \cot\alpha \qquad \text{Eq. 5.8}$$

From equation 5.8 the required Scheimpflug angle for any given magnification is then equal to:

$$\therefore |\alpha| = Arctan(\frac{1}{\sqrt{|M_V|}}) \qquad \text{Eq. 5.9}$$

In particular, these equations show that when α = β = 45º, both the transverse magnification and the magnification of the tilted planes are both equal to 1.

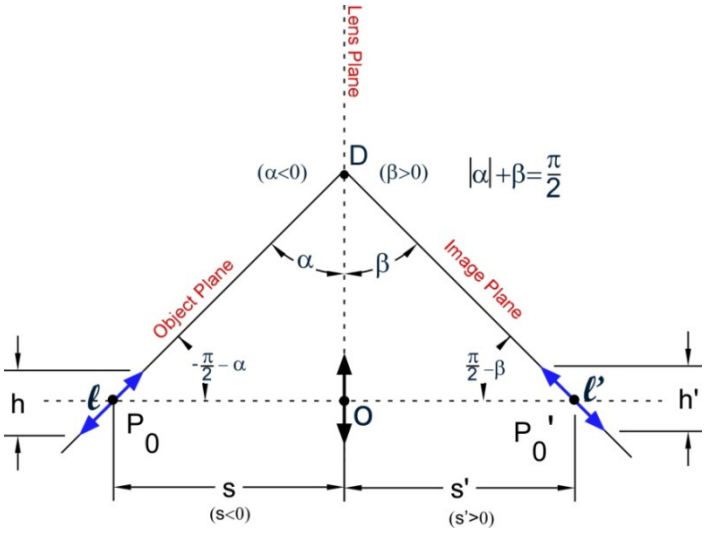

Figure 5.3: The derivation of the image plane and object plane angles required for the field of view, depth of focus and magnification needed to image the cross-sectional view of the lens.

5.4. Optical – Mechanical system design

The equations derived in the previous section were used to select the optimal lenses, camera sensor and system dimensions. In the case of the crystalline lens mounted in the EVAS lens stretcher, the largest object dimensions are the stretched ciliary ring diameter in the equatorial direction and the unstretched lens thickness in the axial direction. Taking into account positioning tolerances the corresponding field of view is 10 by 15 mm. The camera is mounted in such a way that the largest dimension is parallel to the equatorial plane. The tilted object plane is typically a sagittal plane which passes through the center of the lens. The distance ℓ in Figure 5.3 therefore corresponds to the crystalline lens thickness and the distance ℓ' corresponds to the smallest dimension of the imaging sensor.

To provide high resolution and high sensitivity the selected imaging sensor is a 6 megapixel, 16bit, 1 inch CMOS camera (PL-A781, PixelLINK, Ottawa Canada). The size of the sensor is 12.5 x 16 mm. Given that the desired object field of view is 10 x 15mm a magnification of 1:1 was selected for the imaging system corresponding to a Scheimplfug angle: $\alpha = \beta = 45°$.

The objective was designed using a matched achromatic doublet (f_1=f_2=100mm, MAP101001A1, Thorlabs, Newton, NJ) (Figure 5.4). The system was mounted on a micropositioner translation stage (UMR5.25, Newport Irvine, CA) for fine focus adjustments. The objective and camera were mounted together onto an aluminum base and covered with a custom designed enclosure which avoids the detection of stray light (Figure 5.5).

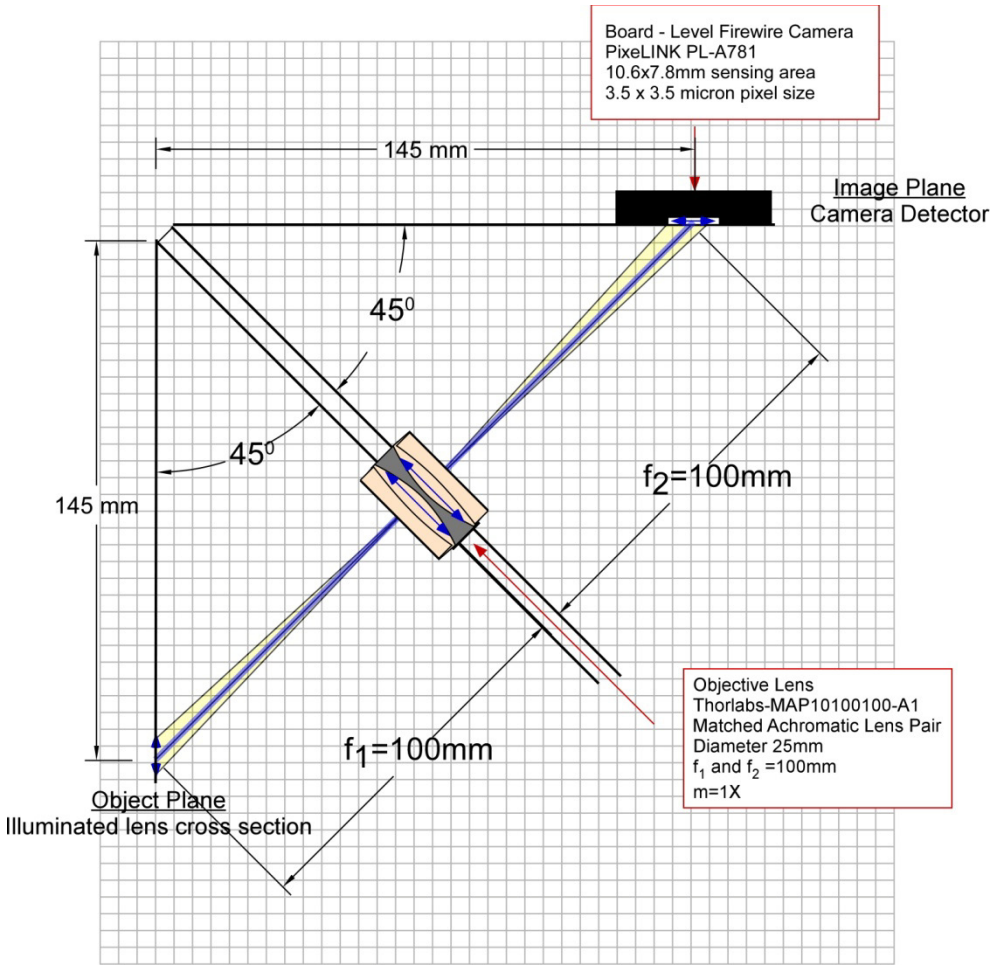

Figure 5.4: Optical schematic of the Scheimpflug imaging system. The camera is positioned at the back focal plane of the objective lens. The object is positioned at the front focal plane of the objective lens.

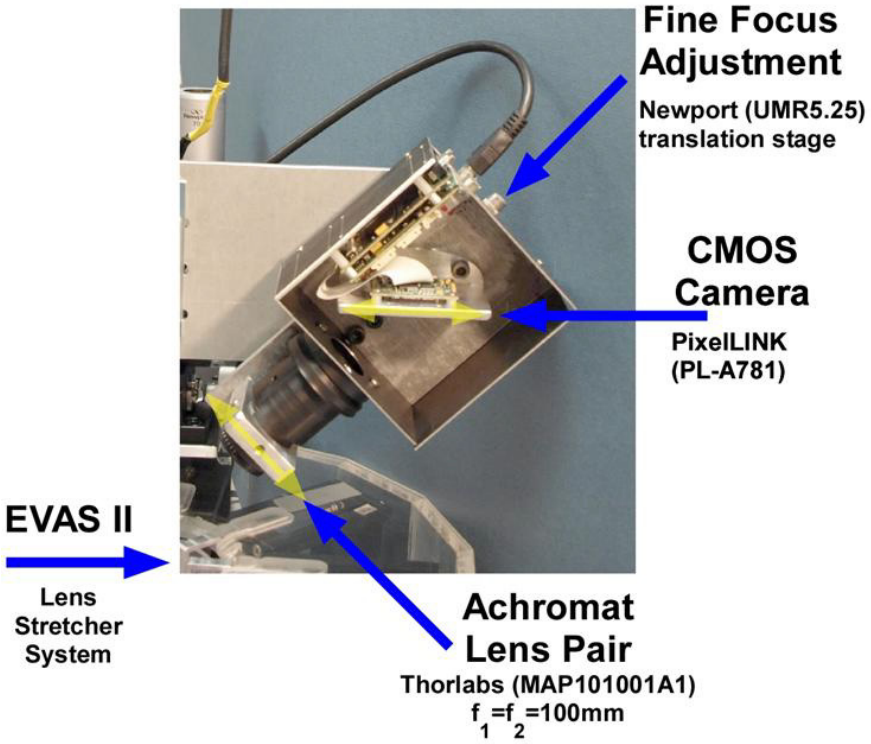

Figure 5.5: The prototype Scheimpflug system positioned in place over EVAS II lens stretching system. Stray light is removed from the system by covering the system with a black anodized aluminum box (removed for the photograph). The camera and lens system can translate together for fine focus adjustment.

5.5. Design of a Kohler illumination system

5.5.1. General description

The illumination system is designed to produce a narrow and uniformly illuminated bright line which is in focus from the lens anterior surface to the lens posterior surface (Figure 5.6). The illumination system is designed to generate a line 100µm wide by 10mm long with a depth of focus of 7mm in air (5.25mm in water and 5mm in the lens). The system consists of:

- A high power (50W) tungsten halogen bulb (filament dimensions of 3.3mm x 1.5mm)
- A 16mm focal length 3 element condenser lens (clear aperture of 22.5mm, NA =0.69)
- A custom made 100µm x 12.5mm slit aperture (National Aperature, Inc. Salem, NH)
- And a pair of 160mm matched achromatic lenses for the projection lens (NA =0.067)

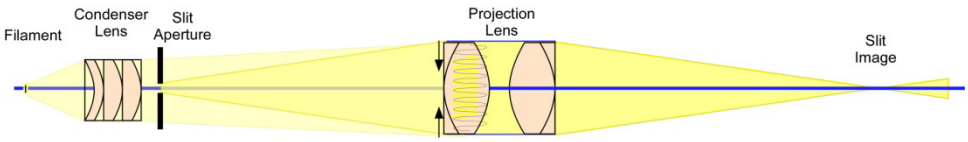

Figure 5.6: Kohler illumination system. The light emitted from a filament is imaged by a condenser lens through a slit aperture onto the entrance aperture of a projection lens. The projection lens re-images the slit aperture onto the target.

The arrangement of a Kohler illumination system was selected to insure uniform illumination intensity (Figure 5.6). In the Kohler illumination system a condenser lens forms an image of a lamp filament in the aperture of a projection lens (Kingslake 1983). A slit aperture is placed close behind the condenser lens where it is uniformly illuminated. The projection lens then forms an image of the slit aperture on the desired target.

The Kohler illumination system is designed to illuminate the lens cross section with sufficient light to produce high contrast images on the camera. Only a small proportion of the light from the illuminated target (lens cross section) reaches the camera due the off-axis orientation of the Scheimpflug optics. The irradiance (the flux per unit area) of the lens cross sectional image on the camera is dependent on the irradiance of the slit image on the crystalline lens and the optics of the Scheimpflug camera. The irradiance of the slit image which illuminates the lens is dependent on the brightness of the light source and the optics of the Kohler illumination system. The depth of focus of the slit image is dependent on the numerical aperture of the illumination system.

The first step in the design of the Kohler illumination system is to determine an expression for the irradiance of the slit image on the target (crystalline lens). This expression will be based on the optics of the Kohler system and the brightness of the light source. Next an expression for the irradiance of the image of the illuminated lens cross section on the camera sensor will be derived. This expression will be based on the optics of the Scheimpflug system

and the brightness of the slit image. This expression will give the minimum brightness of the light source needed to illuminate the crystalline lens to produce high contrast images on the camera. Finally an expression for the depth of focus of the illumination system will be derived to select the optimal lenses for the Kohler illumination system.

5.5.2. Radiometric Calculations of the Kohler Illumination system

5.5.2.1. Irradiance of the slit image

In this section an expression for the irradiance in the plane of the crystalline lens will be derived. This expression will be used to determine the minimum light source brightness and optimize the optics of the illumination system to maximize the light collected by the camera.

The irradiance of the slit image is a function of the brightness of the filament light source, the transmission and the acceptance angle (numerical aperture) of the condenser lens and the transmission of the projection lens (Figure 5.7). The irradiance E_s in [W·cm^{-2}] at the slit aperture illuminated by a source with brightness B_0 [W·sr^{-1}·cm^{-2}] and condenser lens with transmission *Tc* and half angle aperture θ_c (Kingslake 1983) is:

$$E_s = T_c \cdot \pi B_O \cdot \sin^2\theta_c \qquad \text{Eq. 5.10}$$

The projection lens of the Kohler system re-images the slit aperture onto the target. The irradiance on the target is a function of the brightness of the slit aperture B_{slit}.

The condenser images the filament on the projection lens. All of the light collected by the condenser lens and transmitted through the slit is therefore also transmitted to the image plane except for the transmission losses of the projection lens. The irradiance [W·cm^{-2}] of the slit image on the target is then simply determined by magnification factor M and transmission T_p of the projection lens:

$$E_{slit\ image} = \frac{T_p \cdot T_c \cdot \pi B_O \sin^2(\theta)}{M} \qquad \text{Eq. 5.11}$$

From Eq. 5.11 it can be seen that the irradiance of the slit image is proportional to the square of the condenser lens numerical aperture (sin θ) and the brightness of the light source, and inversely proportional to the magnification *M*. The choice of the magnification M is a tradeoff between the brightness of the slit image and the depth of focus (Section 5.5.2.6). A 1:1 magnification (M=1) was selected for the design.

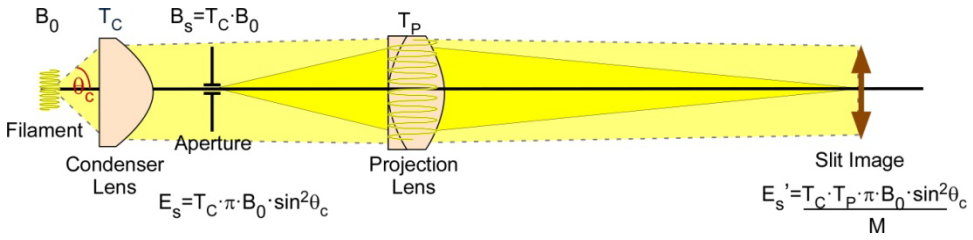

Figure 5.7: Brightness of the slit image of a Kohler illumination system.

5.5.2.2. Irradiance of the Scheimpflug image

The Kohler system is designed to illuminate a thin cross section of the lens. The light reflected by the lens surfaces are collected by the Scheimpflug imaging system. To calculate the irradiance in the plane of the camera sensor, we need to first determine the amount of the light reflected by the lens surfaces. If we assume that the lens is a diffuse Lambertian reflector then the reflectance R(θ) from the lens surfaces can be written:

$$R(\theta) = R_0 \cdot \cos\theta \qquad \text{Eq. 5.12}$$

Where R_0 is the reflected light at normal incidence and θ is the viewing angle. The reflected light is then collected and re-focused on the camera sensor by the Scheimpflug imaging system. The Scheimpflug system is an off-axis imaging system. The image irradiance (E_{image}) of an off-axis imaging system is dependent on the irradiance of the object (E_{source}), the imaging system numerical aperture (NA) and the angle (γ) between the object and the imaging system (Kingslake 1983, modified by integrating over the off-axis collection angle (θ_S).

$$E_{Scheimplfug\ image} = E_{slit\ image} \cdot R_0 \cdot \cos^4(\gamma) \cdot T_S \cdot \theta_S \cdot \sin 2\theta_S \quad \text{Eq. 5.13}$$

Where T_s is the transmittance of the Scheimpflug imaging system, γ is the Scheimpflug angle, θ_s is the angular aperture of the Scheimpflug imaging system. In our case the imaging system is at an angle of $\gamma = 45°$, with a numerical aperture of $\theta_s = 0.11$ rad. We assume the system has a transmittance of $T_s = 80\%$ and that $R_0 = 0.03\%$ (specular reflection at normal incidence between aqueous and the lens capsule). With these values the irradiance in the plane of the Scheimpflug image is:

$$E_{Scheimplfug\ image} = 1.45 \times 10^{-6} \cdot E_{slit\ image} \quad \text{Eq. 5.14}$$

5.5.2.3. Minimum system irradiance

The camera manufacturer (Pixelink Ottawa, CA) specifies the minimum radiant exposure [J·cm^{-2}] which the sensor can detect (Noise equivalent exposure). This value is wavelength dependent and given at by the manufacturer at a wavelength of 600nm to be 225 pJ·cm^{-2}. Direct comparison with the previous calculations requires this value to be converted into units of W·cm^{-2}. In the worst case scenario, the minimum irradiance required for the camera sensor at its shortest integration time (40 ms at 15frames per second) is:

$$E_{CAMERA\ min} = 5.63 \times 10^{-9}\ W/cm^2 \quad \text{Eq. 5.15}$$

Based on these results and Eq. 5.14 we can now calculate the minimum irradiance of the slit image needed to create an image of the lens with the Scheimpflug camera.

$$E_{min} = \frac{E_{CAMERAmin}}{1.45 \times 10^{-6}} = 3.9 \times 10^{-3}\ W/cm^2 \quad \text{Eq. 5.16}$$

The camera manufacturer also lists the camera sensor's maximum energy density which will completely saturate the sensor (saturation equivalent exposure = 153.5 nJ·cm^{-2}. A similar

calculation can be performed to show the maximum irradiance of the slit image which will saturate the camera:

$$E_{max} = 0.11\ W/cm^2 \qquad \text{Eq. 5.17}$$

E_{max} and E_{min} are dependent on several factors which are adjustable through the camera software. These values are given for 10bit images, 40ms integration times, 15 frames per second and no electronic gain. These parameters will be adjusted for each image to produce the highest contrast.

5.5.2.4. Radiometric evaluation of the Kohler system

Direct irradiance measurements of the custom designed Kohler illumination system were performed with a calibrated light meter connected to an irradiance detector head (VL-3701-4, Gigahertz-Optik GmbH, Germany). For comparison direct irradiance measurements were repeated on a commercial Zeiss Kohler slit-lamp. The maximum measured irradiance of the slit image was well above the minimum required irradiance (E_{min}). Based on these results the custom designed Kohler slit-lamp produces ample irradiance for Scheimpflug imaging of the lens (Figure 5.8). With the values assumed for the calculation the slit irradiance is approximately two orders of magnitude above the saturation threshold for the specular reflection from the anterior lens surface. This high intensity is desired since one of the ultimate goals is to image the much dimmer diffuse reflections from the internal lens structures.

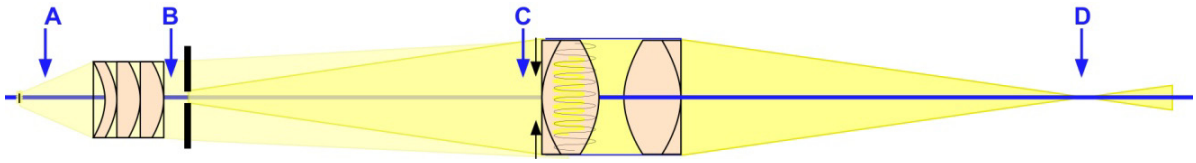

Measured Irradiance - E (W/cm^2)

	Position	Zeiss	Custom
A	Filament	933	5103
B	Aperture	616.8	43.8
C	Projection Lens	4.71	6.4
D	Slit Image	9.97	**16.15**

Figure 5.8: Direct irradiance measurements of commercial slit-lamp illumination system (Zeiss) and a custom designed slit-lamp. The custom designed illumination system has a larger filament combined with a larger condenser lens numerical aperture which helps to produce almost twice the irradiance of the commercial system.

5.5.3. Depth of focus of the Kohler illumination system

The depth of focus of the Kohler illumination system is dependent on the focal length of the projection lens and the diameter of the collimated light beam entering the projection lens. The beam diameter is dependent on the magnification of the light source filament by the condenser lens, which re-images the filament onto the entrance pupil of the projection lens (Figure 5.9).

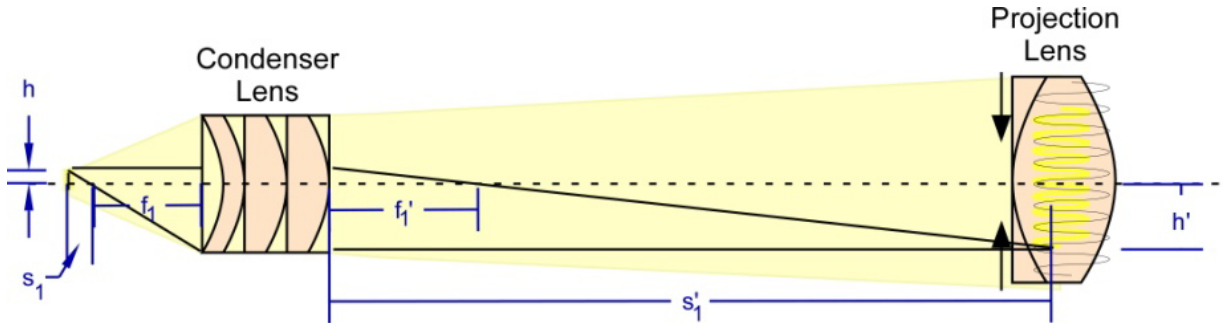

Figure 5.9: The condenser lens of the Kohler illumination system collects light from the filament and re-images the filament onto the projection lens. The depth of focus of the Kohler system is dependent on the magnification of the filament by the condenser lens.

From the conjugation formula it can be seen that the magnification of the light source filament is given by:

$$m_1 = \frac{h'}{h} = \frac{s'_1}{s_1} \qquad \text{Eq. 5.18}$$

Where s_1 is the distance from the filament to the condenser, s'_1 is the distance from the condenser to the image of the filament, h' is the height of the filament image and h is the height of the real filament. The projection lens has a diameter (h') of 22. 5 mm and the filament has a length (h) of 3.3 mm which gives a required magnification of ~6.75X. The location of the image is given by:

$$\frac{1}{s_1'} = \frac{1}{f_1} + \frac{1}{s_1} \qquad \text{Eq. 5.19}$$

where f_1 is the focal length of the condenser lens. The condenser lens chosen for this system is a 3 element 16mm focal length condenser lens (NA=0.69). The object distance s_1 is 18.5 mm from the condenser lens which places the properly magnified image of the filament at 120 mm from the condenser lens.

In the Kohler illumination system a thin slit aperture (12.5 mm X 100 μm) is placed close to the back surface of the condenser (Figure 5.10). The uniformly illuminated aperture is re-imaged by the projection lens onto the target with 1:1 magnification. The depth of focus of the projected image is dependent on the focal length projection lens and the entrance beam diameter (Figure 5.11). The entrance beam diameter is assumed to be the height of the filament image in the plane of the projection lens (h' =22.5 mm). A matched pair of achromatic lenses (f= 160 mm) was selected for this projection lens system. The combination of these two lenses gives the projection lens system an effective focal length of 80 mm. Unity magnification can be achieved by placing the slit-aperture at the front focal length of the first achromat lens ($s_2 = s_2' = 160$ mm, Figure 5.10).

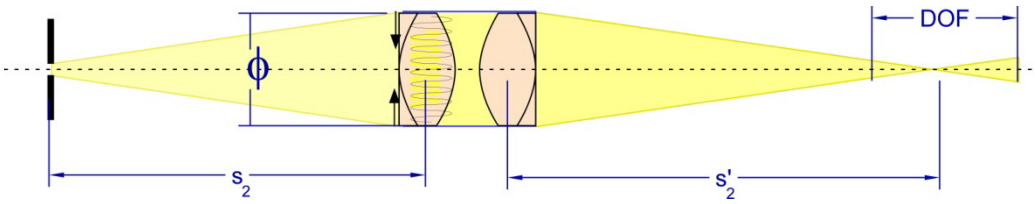

Figure 5.10: The projection lens of the Kohler illumination system re-images the uniformly illuminated slit-aperture onto the target with 1:1 magnification.

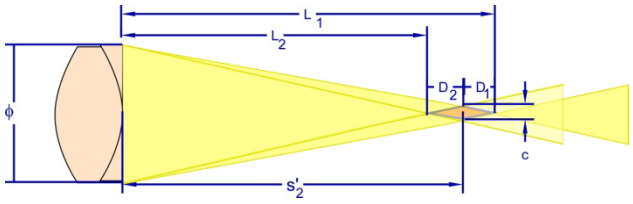

Figure 5.11: The location of the near (L_2) and far (L_1) depth of focus limits of the Kohler illumination system. Preliminary experiments showed that a blur diameter of 0.25mm in the object space was acceptable.

The depth of focus of the Kohler illumination system is defined as the distance along the optical axis in the neighborhood of the slit image where the width of the out-of-focus slit image is within an acceptable limit. Preliminary experiments showed that images with acceptable quality could be obtained with a 250μm slit. This value was chosen as the blur size defining the depth of focus. With the notation of Figure 5.11 the equation for the depth of focus is given by (Kingslake 1986):

$$DOF = L_1 - L_2 \qquad \text{Eq. 5.20}$$

where L_1 and L_2 are given by:

$$L_1 = \frac{s}{1 - \frac{C(s-f)}{\emptyset \cdot f}} \; and \; L_2 = \frac{s}{1 + \frac{C(s-f)}{\emptyset \cdot f}} \qquad \text{Eq. 5.21}$$

where $s=s'_2$ is the distance between the lens and the slit image, f is the focal length, C is the maximum allowable image diameter and Φ is the entrance beam diameter. With the selected design parameters the depth of focus is equal to 10.8mm in air. This depth of focus is barely sufficient to sharply illuminate the whole lens immersed in water.

5.6. The complete Scheimpflug system

The completed system was designed to integrate with the EVAS II lens stretcher system (Figures 5.12 and 5.13). The design involved a mechanical system design carried out in a three-dimensional computer design software (Solidworks, Concord, Mass). The Scheimpflug camera and illumination system were mounted on a small aluminum plate. The plate was then mounted on a three axis micro-positioner stage (123-4750 65mm Dovetail XYZ Stage, OptoSigma, Santa Ana, CA) to allow position adjustment. The completed system was attached to a rotating arm (Newport, Irvine, CA) which allows the camera to swing in place over the EVAS II lens stretching system.

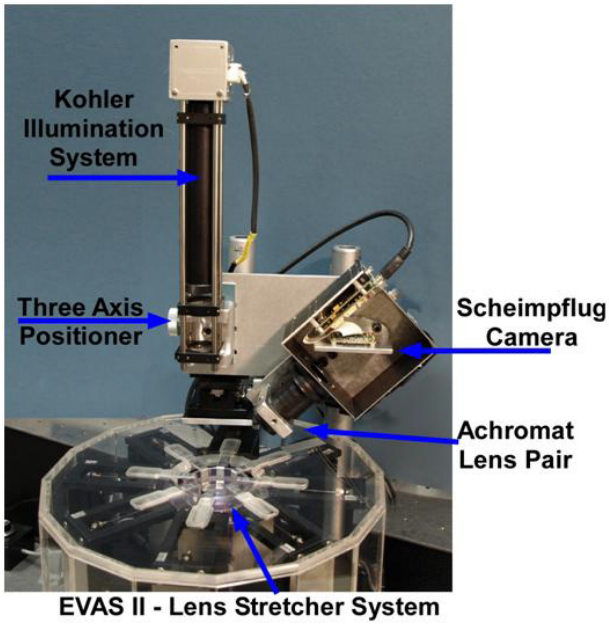

Figure 5.12: The Scheimpflug camera system and Kohler slit illumination system positioned over the EVASII lens stretcher system. The camera cover was removed for illustration purposes.

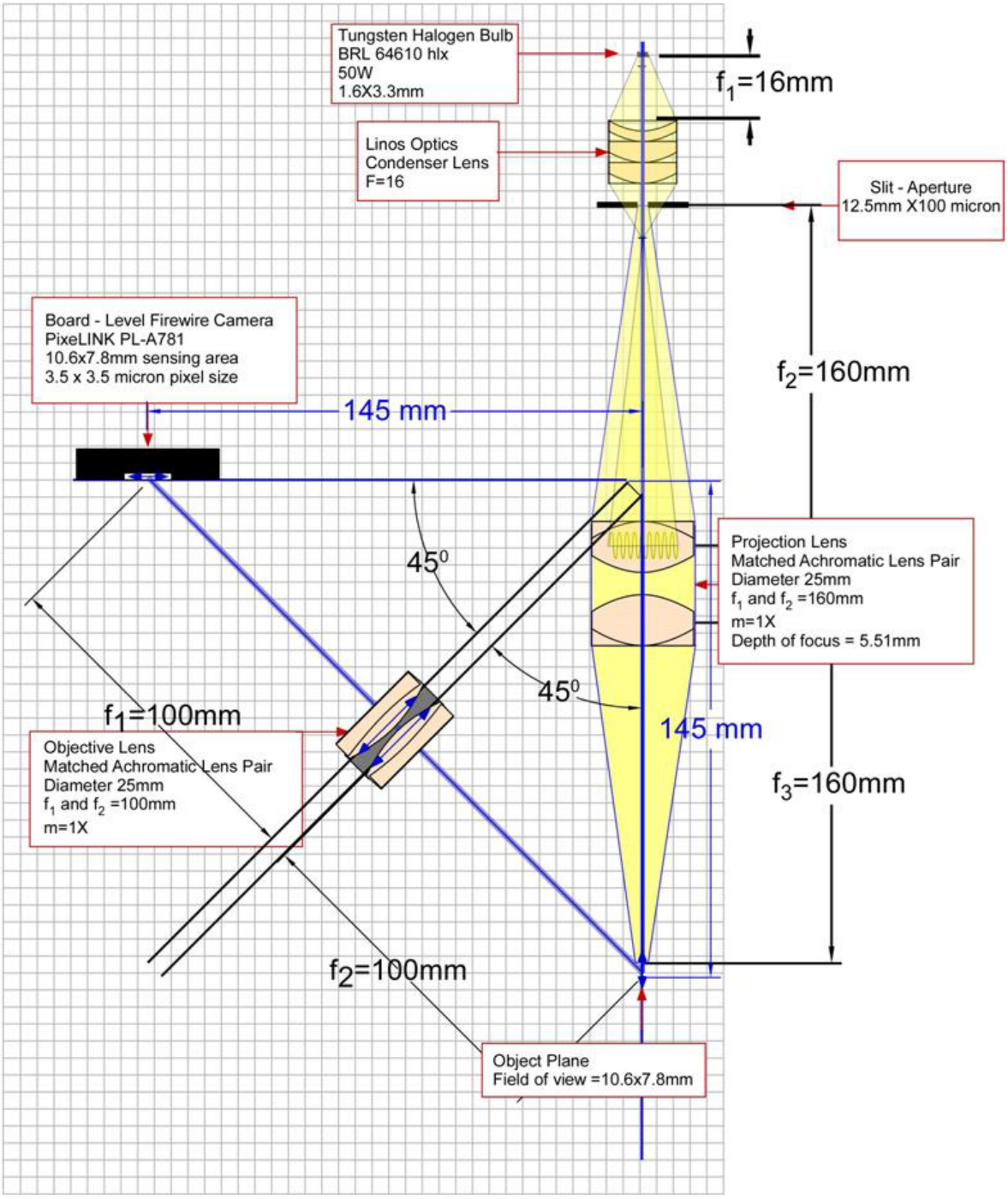

Figure 5.13: A two dimensional schematic of the Scheimpflug camera system and Kohler slit illumination system.

5.7. Preliminary testing

Preliminary tests on a cynomolgus monkey lens demonstrated that the completed system is able to acquire cross sectional images in vitro lenses. Figure 5.14 shows a typical image produced by the Scheimpflug system compared to a shadowgraph image of the same lens. Clearly the lens central thickness is thinner in the distorted Scheimpflug image compared to the undistorted shadowgraph image. This distortion is due to two optical factors. First, imaging systems using the Scheimpflug principle cause keystone distortion because the magnification varies across the field of view. Second, the image of the posterior lens surface is distorted by the anterior lens surface and the gradient refractive index. The correction of these inherent distortions is the topic of the following section.

A. B.

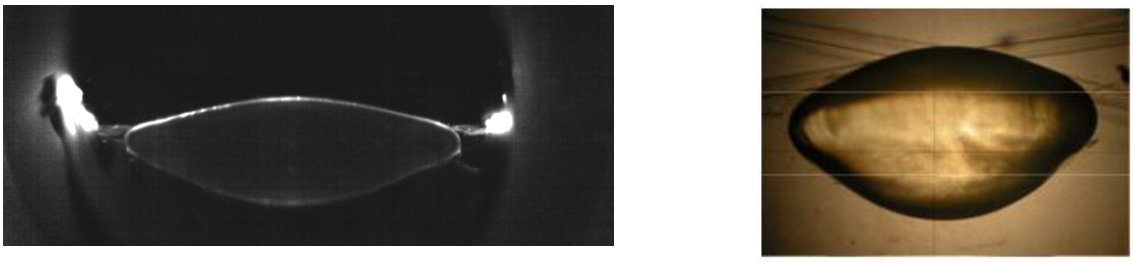

Figure 5.14: (A.) A sample uncorrected Scheimpflug image of an unstretched 7.5 year old cynomolgus monkey lens with zonules and cilliary body still attached. (B.) A shadowgraph image of the same isolated lens after removal from the zonules and cilliary body.

5.8. Correction of distortions of the Scheimpflug imaging system

5.8.1. Purpose

The goal of this section is to correct the imaging distortions of the Scheimpflug system to obtain accurate measurements of the lens shape from the Scheimpflug images. A digital image processing algorithm was developed in MatLab 7.1, to correct the distorted Scheimpflug images. The correction algorithm is based on a ray tracing technique first developed by Richards et al (1988) for the correction of in vivo Scheimpflug images. During in vivo Scheimpflug imaging,

the geometry of the system and the eye's refractive surfaces anterior to the lens distort the image of the lens. Recently similar techniques have been used by Dubbleman and Van der Heijde, (2001) to accurately measure the lens thickness and surface curvatures. The correction algorithm developed for this system has been modified for the in vitro case where the cornea and iris are removed and the lens is submerged in a preservation medium.

5.8.2. General description

The Scheimpflug image correction algorithm traces rays from each pixel on the image plane to its corresponding and originating location on the object plane. The correction algorithm takes into account and corrects for the refraction of each ray at the water-air interface of the tissue chamber and the refraction at the anterior surface of the lens. An age-dependent uniform refractive index is assumed for each measured lens during the correction algorithm. The correction algorithm can be divided into the following steps:

- Step 1: A coordinate system is created based on the dimensions of the Scheimpflug system.
- Step 2: Rays are traced from each image pixel corresponding to the air-water boundary through the nodal points until they reach the object plane. This ray trace corrects the image of the air-water boundary.
- Step 3: Rays are traced from each image pixel corresponding to the anterior (or posterior) lens surfaces through the nodal point until they reach the air-water boundary.
- Step 4: The refraction of these rays at the air-water boundary is calculated.
- Step 5 (anterior lens surface only): The refracted rays are traced from the air-water boundary until they reach the object plane.

- Step 5 (posterior lens surface only): The refracted rays are traced from the air-water boundary until they intersect the anterior lens surface.
- Step 6 (posterior lens surface only): The refraction of these rays at the anterior lens surface is calculated.
- Step 7 (posterior lens surface only): The refracted rays are traced from the anterior lens surface until they reach the object plane.

Steps 1 and 2 of this algorithm correct for the geometric imaging distortions during Scheimpflug imaging. These two steps of the correction algorithm were validated on Scheimpflug images of high precision stainless steel ball bearings. Steps 1 through 5 correct for the distortions of imaging an object through water. These steps of the correction algorithm were validated by imaging the same set of high precision stainless steel ball bearings while submerged in water. Steps 6 through 8 of the algorithm correct for the distortions of imaging the posterior lens surface through the anterior lens surface. These steps of the algorithm will produce accurate measurements of lens thickness and surface profiles. The correction algorithm for the posterior lens surface was validated on a set of bi-convex glass lenses. Finally the completed algorithm was validated on a group of crystalline lenses. The corrected Scheimpflug measurement results of this group of lenses were compared with the results obtained from the shadowphotogrametry (Section 3.3.1) technique and the optical coherence (Section 3.3.2) tomography technique.

5.8.3. Creation of the coordinate system

The first step in the correction algorithm is to establish a three-dimensional coordinate system (Figure 5.15). We define the origin of this coordinate system at the center of the object plane. The plane of illumination defines the z-axis. The image plane is parallel to the x-y plane and the object plane is the x-z plane (y=0). The centers of the image plane, lens plane and object

plane are all located on the y-z plane (x=0). The nodal points of the imaging system are located in the y-z plane. Their position was calculated using a paraxial optical analysis of the imaging system implemented in ZEMAX (ZEMAX Development Corporation, Bellevue, WA). From Figure 5.15 it can be seen that the coordinates of the nodal points are:

$$x_n=0,\ y_n = z_n = \frac{N}{\sqrt{2}} \qquad \text{Eq. 5.22}$$

$$x_{n'}=0,\ y_{n'} = z_{n'} = \frac{N'}{\sqrt{2}}$$

Where N =112.5mm and the N'= 101.5mm are the distances from the first nodal point to the origin and from the second nodal point to the center of the image plane, respectively. The center of the image plane has the following coordinates:

$$y_i = z_i = \frac{N+N'}{\sqrt{2}} \qquad \text{Eq. 5.23}$$

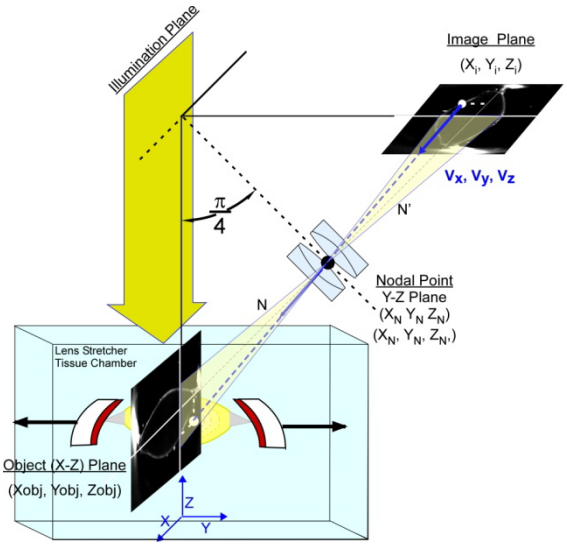

Figure 5.15: Optical schematic of the Scheimpflug system. The images acquired have geometrical distortions due to the geometry of the system and optical distortions due to imaging the lens through a surface of water and through the lens itself. The goal of the correction algorithm is to calculate the undistorted size and shape of the object. The location of the nodal point and the location of the image on the image plane are calculated from the optical design of the system. The ray tracing algorithm traces rays from the image plane through the nodal point to the originating location of the ray on the object plane. At the scale of the drawing the nodal points N and N' are superimposed.

Coordinate system locations (mm)		**(x, y, z)**
Origin of the system and the center of the object plane	$(x_{obj}, z_{obj}, y_{obj})$	(0, 0, 0)
First nodal point N	(x_N, y_N, z_N)	(0, 77.9, 77.9)
Second nodal point N'	$(x_{N'}, y_{N'}, z_{N'})$	(0, 87.3, 87.3)
Center of the image plane	(x_i, y_i, z_i)	(0, 166.7, 166.7)

5.8.4. Tracing rays from the image plane to the object plane

According to geometrical optics a ray passing through the first nodal point (N) of an optical system will have a conjugate ray which passes through the second nodal point (N') without undergoing a change in direction (Figure 5.16). A ray connecting a point in the image plane to the second nodal point will have a conjugate with the same direction cosines that passes through the first nodal point and meets the object plane at the conjugate object point. The equation of a line (or a ray) from a point on the image plane (x_i, y_i, z_i) to the second nodal point ($x_{N'}$, $y_{N'}$, $z_{N'}$) is:

$$\begin{aligned} x_{n'} &= x_i + v_x \cdot D_1 \\ y_{n'} &= y_i + v_y \cdot D_1 \\ z_{n'} &= z_i + v_z \cdot D_1 \end{aligned} \qquad \text{Eq. 5.24}$$

Where D_1 is distance from the point on the image plane to the second nodal point and v_x, v_y, v_z are the direction cosines of the ray, which together make up the unit vector of the propagating ray. The direction cosines of the propagating ray are given by:

$$\begin{bmatrix} v'_x \\ v'_y \\ v'_z \end{bmatrix} = \frac{1}{\sqrt{(x_{n'} - x_i)^2 + (y_{n'} - y_i)^2 + (z_{n'} - z_i)^2}} \cdot \begin{bmatrix} x_{n'} - x_i \\ y_{n'} - y_i \\ z_{n'} - z_i \end{bmatrix} \qquad \text{Eq. 5.25}$$

The line which connects a point on the image plane to the second nodal point has the same direction cosines as a line which connects the conjugate point on the object plane to the first nodal point.

$$\begin{bmatrix} v_x \\ v_y \\ v_z \end{bmatrix} = \begin{bmatrix} v'_x \\ v'_y \\ v'_z \end{bmatrix} \qquad \text{Eq. 5.26}$$

The coordinates for the intersection of the propagating ray with the object plane are given by:

$$\begin{aligned} x_{obj} &= x_n + v_x \cdot D_0 \\ y_{obj} &= y_n + v_y \cdot D_0 \\ z_{obj} &= z_n + v_z \cdot D_0 \end{aligned} \qquad \text{Eq. 5.27}$$

where each point on the object plane will lie on the y axis ($y_{obj} = 0$), which gives:

$$D_0 = -\frac{y_n}{v_y}$$

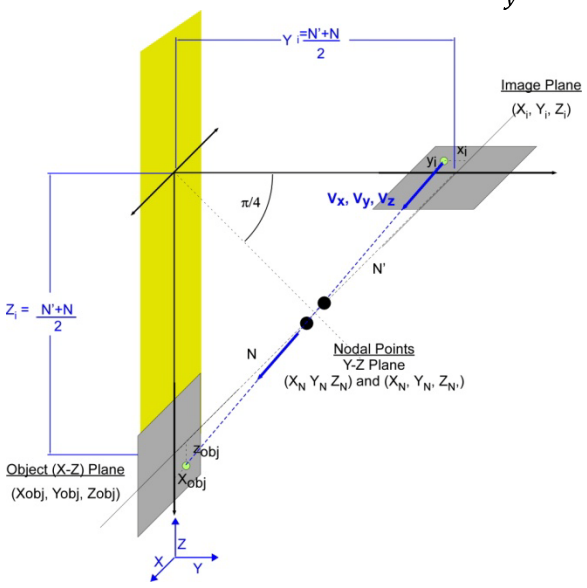

Figure 5.16: Coordinate system for the correction of Scheimpflug images. The first step in the correction process is to define a three-dimensional coordinate system. In this case the object location is selected as the origin of the coordinate system. The z-axis is in the plane of illumination. The object plane is on the x-z plane. The image plane is on the x-y plane. The nodal point and image plane are at known distances from the object location.

The conjugate location of each image point (x_i, y_i, z_i) in the object plane (x_{obj}, y_{obj}, z_{obj}) can now be calculated for every image point location using equations 5.24 through 5.27. These steps correct for the Scheimpflug imaging distortion for direct imaging in air.

5.8.5. Scheimpflug image correction validation

Validation of the ray tracing algorithm for correction of the Scheimpflug image distortions (Eq. 5.24 - 5.27) was performed on 11 high precision stainless steel ball bearings with radii of curvature ranging from 2 to 7.5mm. The ball bearings were placed at the object plane location and illuminated with the Kohler slit-lamp illumination system. The Scheimpflug camera system was then focused on the image of the slit reflected by the ball bearings (Figure 5.17). The uncorrected surface profiles were obtained from the raw Scheimpflug images. The surface profiles were then corrected with the ray tracing algorithm. The radius of curvature of each ball bearing was measured before and after correction. The ray tracing algorithm was able to correct

the Scheimpflug images and produce radius of curvature measurements with a mean error and standard deviation of 0.14 ± 0.13 mm.

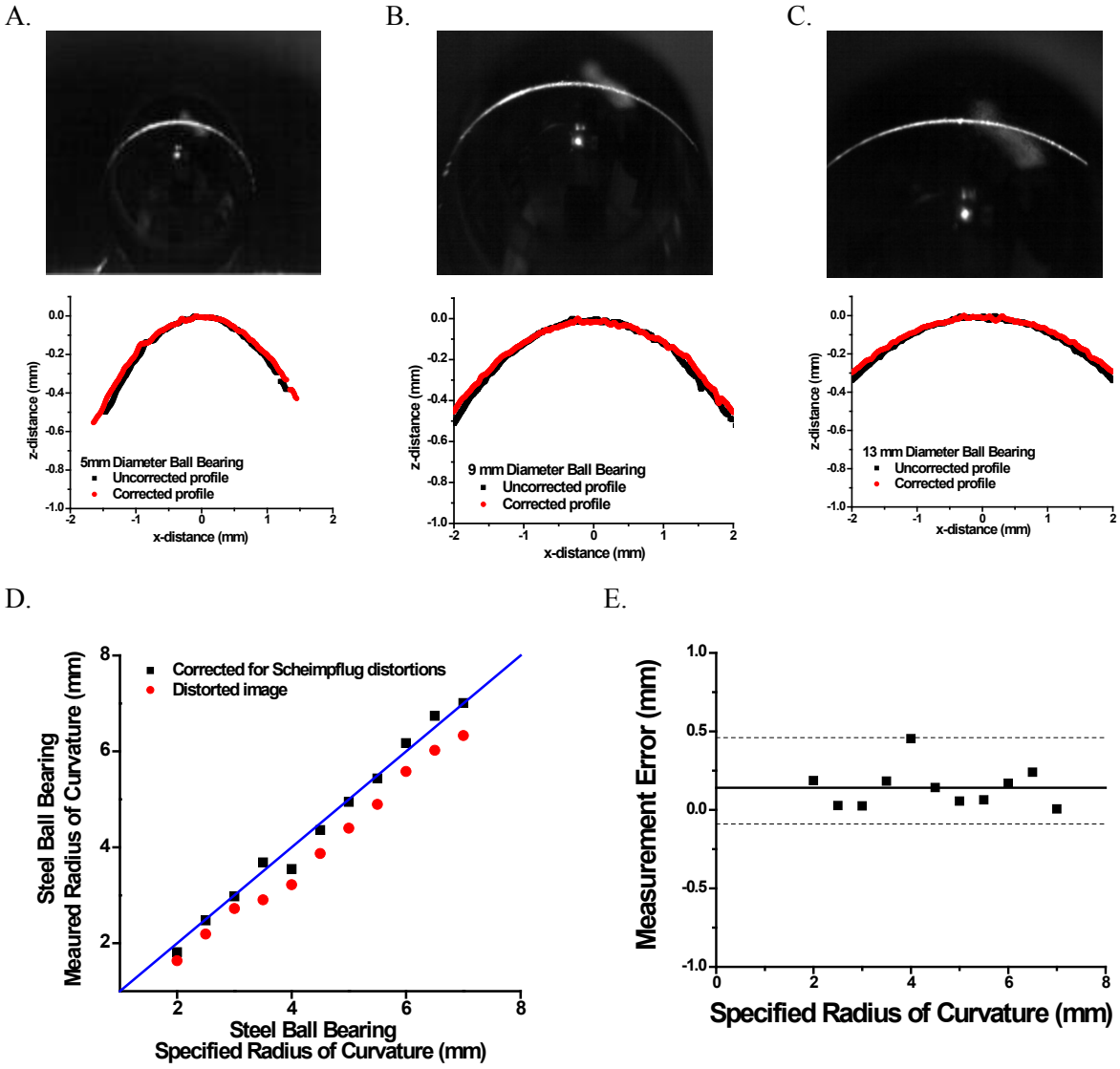

Figure 5.17: Uncorrected Scheimpflug images of a 5, 9 and 13mm diameter ball bearing and their corresponding uncorrected and corrected surface profiles. The Scheimpflug image correction algorithm produces radius of curvature measurements with an average error and standard deviation of 0.14 ±0.13mm.

5.8.6. Correction for refraction at the air-water boundary

The previous section describes the correction of the Scheimpflug distortion when the object is imaged directly and there is no additional refraction. In addition there is a distortion induced from imaging an object which is submerged under water. The rays which are traced from the image plane to the object are refracted at the air water interface (Figure 5.18). Correction of this distortion requires a skew (or 3D) ray-trace since the ray does not lie in a meridional plane (Welford 1986). This section will describe an algorithm to calculate refraction of a three-dimensional skew ray vector at the air-water boundary of the testing chamber.

A.

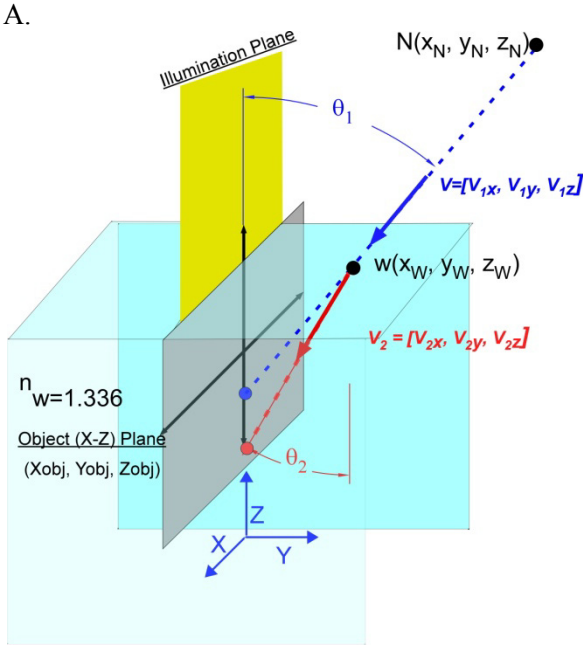

B.

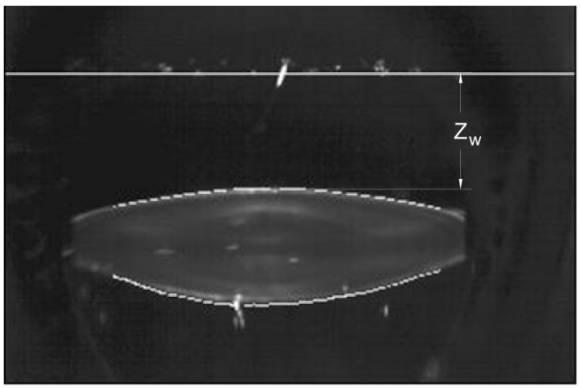

Figure 5.18: A. Refraction of a three dimensional skew ray at an interface of two different refractive index materials. During the ex-vivo accommodation simulation experiments the in vitro lens is preserved in a cell culture medium. B. A sample Scheimpflug image of a human lens while submerged in the preservation medium filled testing chamber. A bright reflection is visible at the location of the air-water interface. Imaging the lens through this medium causes distortions which can be corrected using a ray tracing technique.

The rays which correspond to the anterior and posterior lens surfaces must be traced to the first nodal point until they reach the air-water boundary. The location of the air – water boundary can be clearly seen from the Scheimpflug images of *in vitro* lenses immersed in the preservation medium filled test chamber of the lens stretcher (Figure 5.18). The undistorted location of the water-air interface (z_w) (the point on the water surface where the ray originated) can be calculated with equations 5.24 through 5.27. The point of incidence (x_w, y_w, z_w) on the water surface for the rays which correspond to the anterior and posterior lens surfaces are given by the following ray equations:

$$x_w = x_n + v_x \cdot \left(\frac{z_w - z_n}{v_z}\right)$$
$$y_w = y_n + v_y \cdot \left(\frac{z_w - z_n}{v_z}\right) \qquad \text{Eq. 5.28}$$

Refraction can now be calculated for each ray that passes through the air-water boundary. A vector form of Snell's law must be used to calculate refraction of skew rays. (Welford, 1986):

$$n_1(\vec{v}_1 \times \vec{n}) = n_2(\vec{v}_2 \times \vec{n}) \qquad \text{Eq. 5.29}$$

Where $\vec{n}$ is the unit vector which defines the surface normal at the point of incidence, $\vec{v}_1$and $\vec{v}_2$ are the unit vectors of the incident and the refracted ray, and n_1 and n_2 are the refractive indices of the medium before and after refraction. The unit vectors are composed of the direction cosines for each vector.

$$\vec{n} = (n_x, n_y, n_z)$$
$$\vec{v}_1 = (v_{1x}, v_{1y}, v_{1z}) \qquad \text{Eq. 5.30}$$
$$\vec{v}_2 = (v_{2x}, v_{2y}, v_{2z})$$

This vector form of Snell's Law (Welford 1986) can also be used to solve for the unit vector of the refracted ray ($\vec{v}_2$) as a function of the refractive index of the incident media and the unit vector of the incident ray ($\vec{v}_1$) and the surface normal ($\vec{n}$).

$$n_2\vec{v}_2 = n_1\vec{v}_1 + \vec{n}[n_2\cos(\theta_2) - n_1\cos(\theta_1)] \quad \text{Eq. 5.31}$$

The cosine of the angle of incidence (θ_1) is equal to the vector dot product of the surface normal ($\vec{n}$) and the unit vector of the incident ray($\vec{v}_1$):

$$\cos\theta_1 = \vec{v}_1 \cdot \vec{n} \quad \text{Eq. 5.32}$$

The cosine of the refracted angle can be expressed as a function of the cosine of the incidence angle using Snell's law:

$$n_2\cos\theta_2 = \sqrt{{n_2}^2 - {n_1}^2 + {n_1}^2\cos^2\theta_1} \quad \text{Eq. 5.33}$$

Once $\vec{v}_2$ is found the coordinates of the intersection of the refracted ray with the object plane location (x_{obj}, y_{obj}, z_{obj}) are given by:

$$\begin{aligned} x_{obj} &= x_w + v_{2x} \cdot D_w \\ y_{obj} &= y_w + v_{2y} \cdot D_w \\ z_{obj} &= z_w + v_{2z} \cdot D_w \end{aligned} \quad \text{Eq. 5.34}$$

where each point on the object plane will lie on the y axis (y_{obj}=0), which gives:

$$D_w = -\frac{y_w}{v_{2y}}$$

5.8.7. Validation of the underwater Scheimpflug image correction algorithm

The algorithm developed in the previous section corrects for the distortion due to refraction at the air-water interface. In section 5.8.5 the Scheimpflug image correction algorithm was validated on a set of high precision stainless steel ball bearings. In this section the same set of stainless steel ball bearings were imaged while submerged in distilled water to validate the underwater correction algorithm. The ball bearings were placed in a test chamber filled with distilled water and placed at the object plane location of the Scheimpflug system. The ball bearings were illuminated with the Kohler slit-lamp illumination system. The Scheimpflug camera system was then focused on the image of the slit reflected by the ball bearings (Figure 5.19). The position of the water level and the uncorrected surface profiles were obtained from the

raw Scheimpflug images. The location of the water level and the surface profiles were then corrected with the ray tracing algorithm. The radius of curvature of each ball bearing was measured before and after correction for the underwater distortions. The underwater Scheimpflug ray tracing correction algorithm was able to correct the distorted Scheimpflug images and produces radius of curvature measurements with a mean measurement error of -0.08mm and a standard deviation of ±0.13mm.

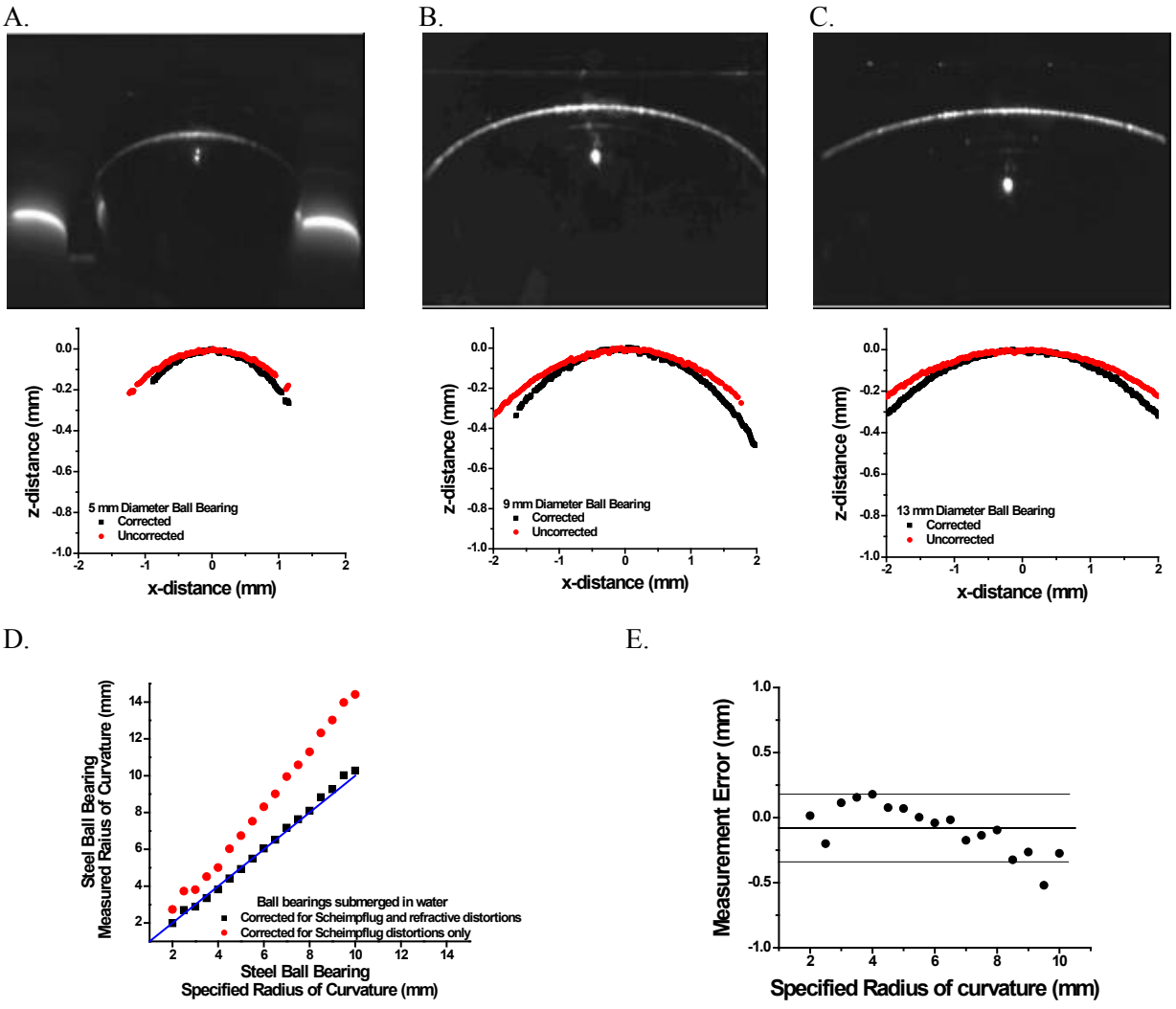

Figure 5.19: (A, B and C) Scheimpflug images of 5, 9, and 13mm diameter ball bearings submerged in water along with the uncorrected and corrected surface profiles for each ball bearing. The images are distorted due to refraction at the air-water boundary. D. The ray tracing algorithm corrects for this distortion and produces radius of curvature measurements with a mean measurement error of -0.084mm standard deviation of ±0.13mm.

5.8.8. Refraction at the anterior lens surface

5.8.8.1. General description

During Scheimpflug imaging of the crystalline lens the posterior lens surface is imaged through the anterior lens surface. The rays from the posterior lens surface are refracted at the anterior lens surface and by the internal gradient refractive index. This correction algorithm will assume the lens has a homogenous refractive index (n_{eq}) and refraction only occurs at the anterior lens surface (Figures 5.20, 5.21 and 5.22). The error introduced by this assumption is expected to be small because the difference in refractive index within the lens is small. The validity of this assumption will be evaluated by comparing Scheimpflug images of in vitro lenses with OCT and shadowgraph images of the same lenses.

The algorithm for correction of the posterior lens surface will:

-calculate the point of incidence ($P_a(x,y,z)$) of a skew ray with unit vector ($\vec{v}_2$) with the anterior lens surface

-calculate the angle of incidence ($\cos\theta_1$) and the angle of refraction ($\cos\theta_2$) and the refracted ray vector ($\vec{v}_3$)

-calculate the point of incidence of the skew ray vector ($\vec{v}_3$) with the object plane (at y=0)

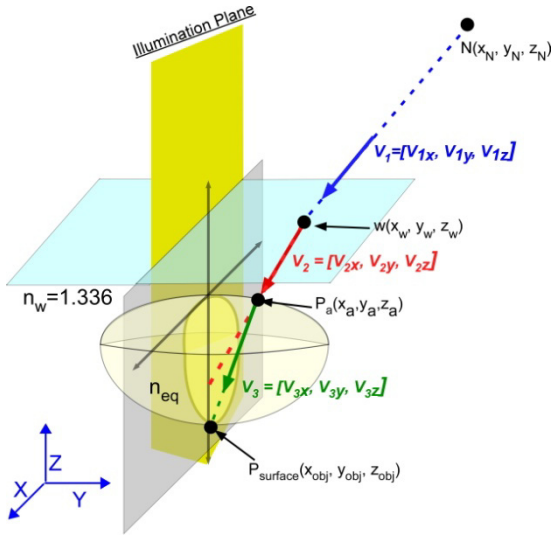

Figure 5.20: A. The image of the posterior lens surface requires correction for the Scheimpflug distortions, refraction distortions at the air-water boundary and refraction at the anterior lens surface. A surface of revolution is created from the corrected anterior lens surface profile. The ray vector ($\vec{v}_2$) is incident on the anterior lens surface at a point $P_a(x,y,z)$. The refracted ray vector ($\vec{v}_3$) travels to the undistorted object plane location of the posterior lens surface.

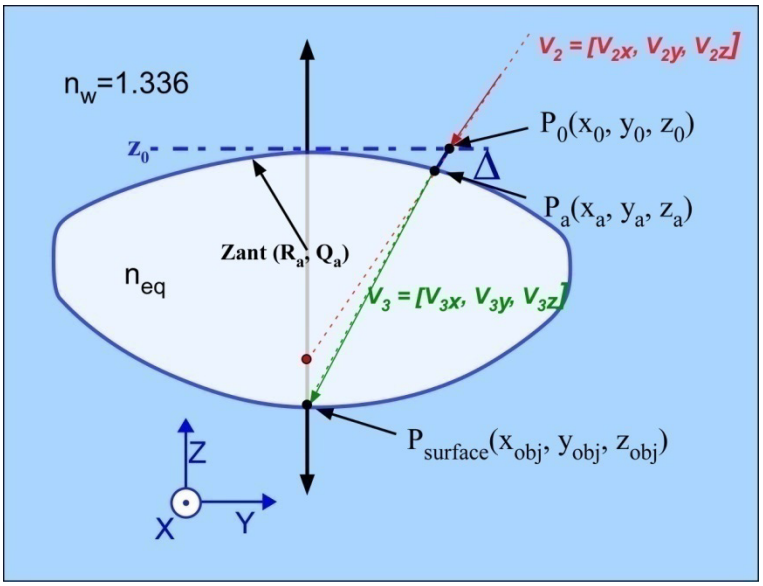

Figure 5.21: A conic surface of revolution (Z_{ant}) is created from the corrected anterior lens surface profile. The ray vector ($\vec{v}_2$) is incident on the anterior lens surface at a point $P_a(x_a, y_a, z_a)$. $P_0(x_0,y_0,z_0)$ is the intersection point of the ray with a reference plane set at the apex of the anterior lens surface. The distance Δ is the distance between the points $P_0(x_0,y_0,z_0)$ and $P_a(x_a, y_a, z_a)$. The refracted ray vector ($\vec{v}_3$) travels to the object plane were it meets the conjugate of the image point: $P_{surface}(x_{obj}, y_{obj}, z_{obj})$.

5.8.8.2. The point of incidence of a skew ray on the anterior lens surface

Figure 5.21 illustrates the path of a skew ray vector ($\vec{v}_2$). The skew ray ($\vec{v}_2$) intersects the anterior lens surface at a point $P_a(x_a, y_a, z_a)$. To solve for this point of incidence an arbitrary plane (z_0) is set at the apex of the anterior lens surface. The point of incidence $P_0(x_0,y_0,z_0)$ for the ray $\vec{v}_2$ with this arbitrary plane can be calculated by:

$$x_o = x_w + \frac{v_{2x}}{v_{2z}} \cdot (z_w - z_0) \qquad \text{Eq. 5.35}$$

$$y_o = y_w + \frac{v_{2y}}{v_{2z}} \cdot (z_w - z_0)$$

Where x_w, y_w, z_w are the coordinates of the point of incidence of the ray vector $\vec{v}_2$ (v_{2x}, v_{2y},v_{2z}) with the air-water boundary and z_0 is the z-axis location of the apex of the anterior lens surface. The point of incidence of the ray vector $\vec{v}_2$ on the anterior lens surface can be calculated by:

$$x_a = x_0 + v_{2x} \cdot \Delta \qquad \text{Eq. 5.36}$$
$$y_a = z_0 + v_{2y} \cdot \Delta$$
$$z_a = z_0 + v_{2z} \cdot \Delta$$

Where (Δ) is the distance along the vector $\vec{v}_2$ from the point P_0 to the point of incidence $P_a(x_a, y_a, z_a)$ on the anterior lens surface (Figure 5.21). To solve for Δ we use the fact that the anterior surface of the lens is described by a quadric of revolution (Welford 1986):

$$z_a = z_0 - \frac{1}{2R_a}(x_a^2 + y_a^2 + p(z_a - z_0)^2) \qquad \text{Eq. 5.37}$$

Where R_a is the anterior surface radius of curvature and p = 1+Q is the shape factor described in section 4.3.1. The unknown term Δ can be solved for by substituting equation 5.36 into equation 5.37 (Welford 1986). The solution for Δ becomes:

$$\Delta = \frac{F}{G + \{G - \frac{1}{R_a}F(1 + pv_{2z} - v_{2z}^2)\}} \qquad \text{Eq. 5.38}$$

where:

$$F = \frac{1}{R_a}(x_0^2 + y_0^2 + pz_0^2)$$

$$G = v_{2z} - \frac{1}{R_a}(x_0 v_{2x} + y_0 v_{2y} + z_0 p v_{2z})$$

The value for Δ obtained from equation 5.38 can now be substituted into equation 5.36 to solve for the point of incidence $P_a(x_a, y_a, z_a)$ of the ray vector $\vec{v}_2$ on the anterior lens surface.

5.8.8.3. The angle of incidence and refraction of a skew ray on the anterior lens surface

The angle of incidence and of refraction of the skew ray $\vec{v}_2$ on the anterior lens surface can be calculated with equation 5.32 and 5.33. However we must first calculate the surface normal of the anterior lens surface. The surface normal unit vector for a conic surface defined by equation 5.38 is given by (Welford 1986):

$$\vec{n}_{ant}\begin{cases} n_x = \dfrac{1-\frac{x_a}{\mathrm{R_a}}}{\sqrt{1-2\frac{z_a}{\mathrm{R_a}}Q}} \\ n_y = \dfrac{-\frac{y_a}{\mathrm{R_a}}}{\sqrt{1-2\frac{z_a}{\mathrm{R_a}}Q}} \\ n_z = \dfrac{1-\frac{(1+\mathrm{Q})x_a}{\mathrm{R_a}}}{\sqrt{1-2\frac{z_a}{\mathrm{R_a}}Q}} \end{cases} \qquad \text{Eq. 5.39}$$

Where x_a, y_a, z_a are the coordinates for the point of incidence of the ray vector $\vec{v}_2$ on the lens anterior surface. The surface normal vector $\vec{n}_{ant}$ can now be used to calculate the angle of incidence (Eq. 5.32), the angle of refraction (Eq. 5.33) and the directional cosines of the refracted ray vector $\vec{v}_3$ (Eq. 5.31).

5.8.8.4. The intersection of a skew ray vector with the object plane

The coordinates of the intersection of $\vec{v}_3$ with the posterior lens surface, $P_{surface}$ (x_{obj}, 0, z_{obj}), for each ray are given by:

$$x_{obj} = x_a - \frac{v_{3x}}{v_{3y}} \cdot y_a$$

$$z_{obj} = z_a - \frac{v_{3z}}{v_{3y}} \cdot y_a \qquad \text{Eq. 5.40}$$

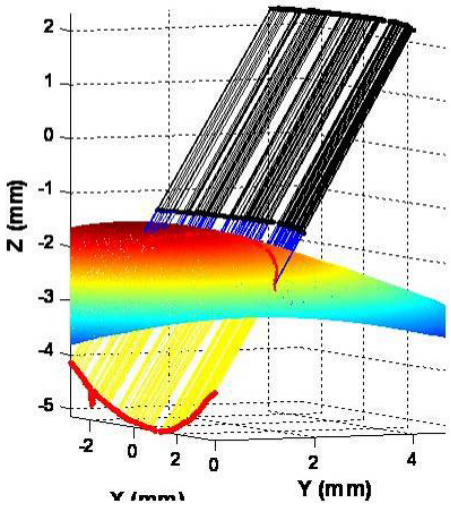

Figure 5.22: Correction of the posterior lens surface by ray tracing. The Figure shows the anterior surface (rainbow gradient) of a human lens. The ray vectors (black lines) from the air –water boundary are traced to the arbitrary plane at the apex of the anterior lens surface. The rays are then traced to the intersection with the anterior lens surface (blue lines). After refraction the rays are traced to the posterior lens surface on the y-axis (yellow lines). The skew ray tracing algorithm is now complete and gives the corrected image of the posterior lens surface (red line).

5.8.9. Posterior lens surface correction validation

The algorithm developed in the previous section corrects for the distortion due to imaging the posterior lens surface through the anterior lens surface. The correction algorithm was validated on three symmetric bi-convex glass lenses (Figure 5.23). The three bi-convex lenses had manufacturer specified radii of curvature of 4.3, 11.4 and 15.3mm. The lenses were placed on a rubber o-ring and submerged in a testing chamber filled with distilled water. The testing chamber was then positioned at the object plane of the Scheimpflug system which was then aligned and focused on the center of the test lens.

The surface profiles were detected from the raw Scheimpflug images with a canny edge detection algorithm. The correction algorithm (Section 5.8.8) was then performed on each lens surface profile. The corrected surface profiles were fit with the spherical radius of curvature function. The results were compared with the manufacturer specified radii of curvature (Figure 5.23 C). The results show that the correction algorithm was able to produce accurate surface curvature measurements for both the anterior and posterior lens surfaces. The skew ray tracing algorithm was able to correct posterior surface radius of curvature measurements with an average measurement error of 0.35mm ±0.14mm.

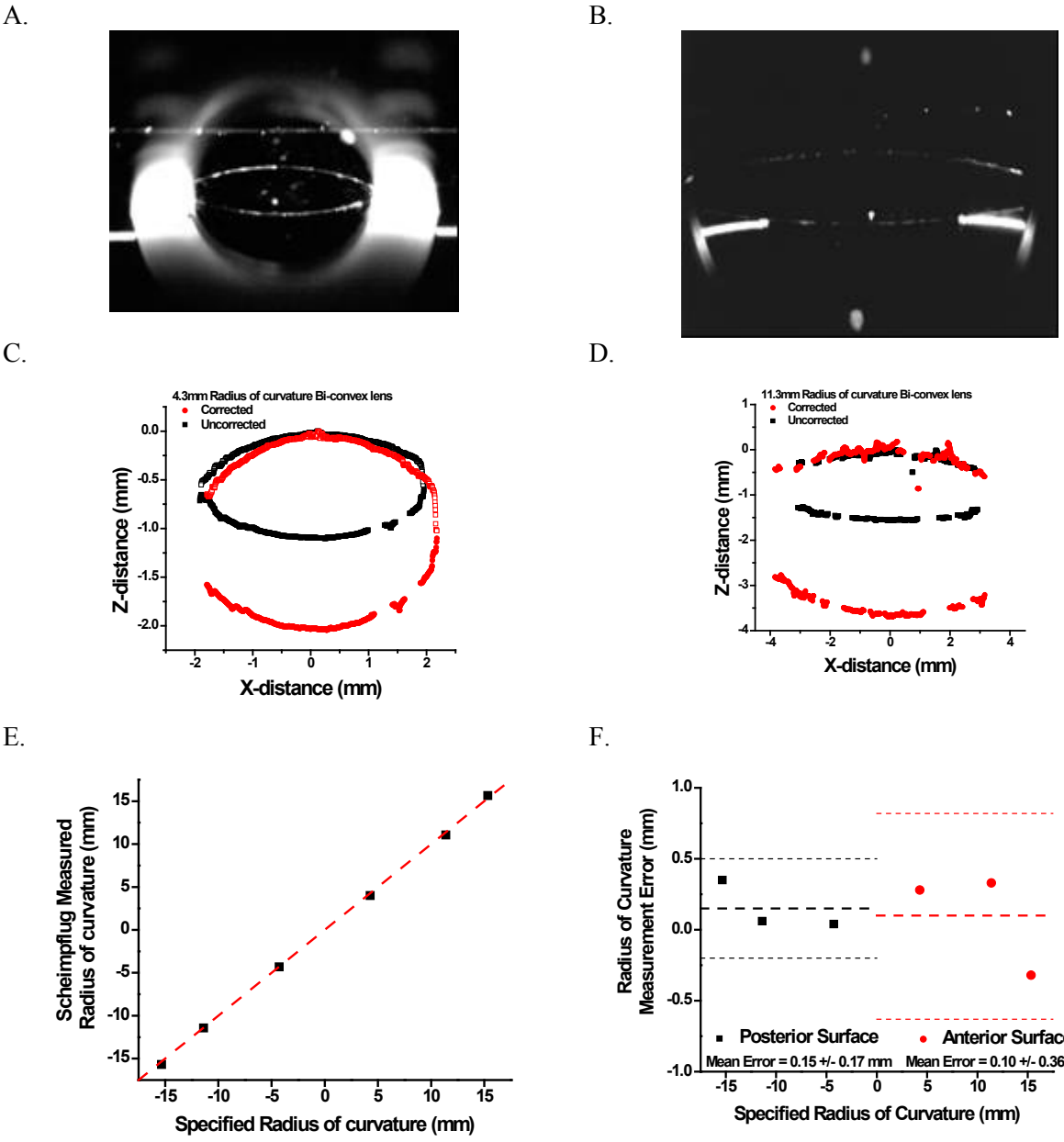

Figure 5.23: Scheimpflug images of two symetric bi-convex lenses with radius of curvatures of 4.3 mm (A.) and 11.4 mm (B.). The surface profiles were corrected for Scheimpflug and refractive distortions. The uncorrected and the corrected surface profiles of the 4.3 mm (C.) and the 11.4 mm (D.) lenses. The surface profiles were fit with a spherical function. The corrected surface curvatures corresponded well with the manufacturer specified radii of curvature. Corrected radius of curvature values for the anterior and the posterior surfaces had an mean measurement error of 0.10±0.36 mm and 0.15± 0.17 mm.

5.9. Validation of in vitro lens Scheimpflug images

A preliminary study was conducted to determine the Scheimpflug system's ability to accurately measure the surface curvatures of in vitro crystalline lenses. In this study the surface curvatures obtained from the corrected Scheimpflug images of in vitro lenses from 4 cynomolgus monkeys, 2 humans and one baboon were compared with those obtained from the undistorted shadowgraph images of the same lenses. A similar study was performed on Scheimpflug and lens OCT images from 14 lenses (from 5 human, 5 cynomolgus and 4 baboon lenses).

The tissue samples were prepared by attaching with cynoacrylate glue the whole globe onto an aluminum annulus ring. The aluminum ring had an inner radius of curvature which matches the curvature of the outer sclera at the limbus. The posterior pole, cornea and iris were then removed. The prepared tissue samples included the lens, zonules and ciliary body attached to the sclera. The tissue samples were immediately placed in a testing chamber and immersed in a hydration controlling cell culture medium (DMEM). The tissue chamber was then placed in the object plane of the Scheimpflug system. The Scheimpflug system was aligned and focused on the central cross section of the crystalline lens. The lens and testing chamber were then placed under the lens OCT system. The system was aligned with the center of the lens and a cross sectional OCT image of the lens was acquired. The lens was then isolated by cutting the remaining zonules. The isolated lens was placed in the shadowgraph testing cell filled with the lens preservation medium. Shadowgraph images of the isolated lens were acquired. A statistical analysis was performed to compare the lens biometry results from all three techniques (Figure 5.24).

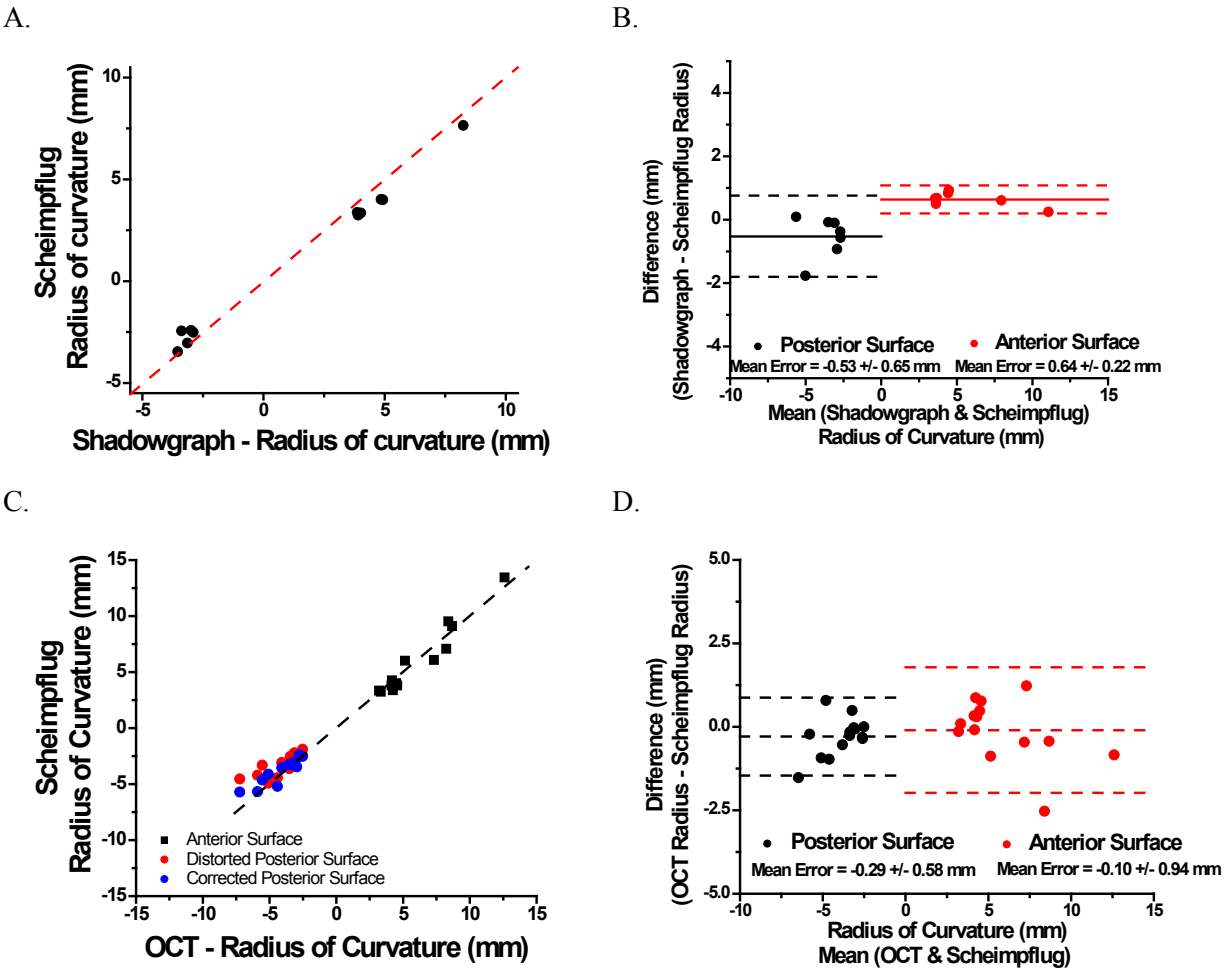

Figure 5.24: A. In vitro lens radius of curvature measurement results from 7 lenses (4 cynomolgus, 2 human and one baboon) obtained with the Scheimpflug technique were compared with those obtained on the same lens with the Shadowgraph technique. B. A Bland-Altman analysis of the Scheimpflug and shadowgraph results indicates that both techniques produce similar results with normaly distributed errors. The mean measurement difference between the Shadowgraph and Scheimpflug results was 0.64 mm for the anterior curvature and -0.53 mm for the posterior curvature. C. In vitro lens radius of curvature measurment results from 14 lenses (5 human, 5 cynomolgus and 4 baboon lenses) obtained with the Scheimpflug technique compared with those obtained on the same lens with the OCT technique. D. A Bland-Altman analysis of the Scheimpflug and OCT results indicates both systems produce simmilar results. The mean measurement difference between the OCT and Scheimpflug results was -0.1 mm for the anterior curvature and -0.29 mm for the posterior curvature.

All three measurement techniques produced comparable radius of curvature and lens thickness measurements. For the central lens thickness the mean measurement difference between shadowgraphs and Scheimpflug images was -0.04 ± 0.36 mm. A similar difference was

observed for central lens thickness measurements from the OCT and Scheimpflug technique (0.07 ± 0.30 mm).

The differences in the radius of curvature results between all three techniques were compared using a Bland-Altman analysis (Figure 5.24). The Bland-Altman analysis plots the difference between the measurement values obtained with two different techniques as a function of the average measurement values. The Bland-Altman statistical analysis assesses the agreement of two measurement techniques (Bland and Altman 1986). The mean curvature difference between shadowgraphs and Scheimpflug images was 0.64 ± 0.22 mm for the anterior curvature and -0.53 ± 0.65 mm for the posterior curvature. The absolute difference between the shadowgraphs and Scheimpflug images are similar 0.64 ± 0.22 mm and 0.53 ± 0.65 mm for the posterior curvature with the Scheimpflug system reporting the larger absalute value. This indicates that the Scheimpflug technique overestimates the radius of curvature of both the anterior and posterior surfaces compared to the shadowgraph technique. The mean measurement difference between the OCT and Scheimpflug results was -0.10 ± 0.94 mm for the anterior curvature and -0.29 ± 0.58 mm for the posterior curvature. The comparison of all three lens biometry techniques indicates that corrected Scheimpflug images of the lens can be used as a valid technique for in vitro lens biometry.

Preliminary experiments showed larger measurement differences in the asphericity between all three measurement techniques. These measurement errors may be due to systemic errors caused by assumptions made during the correcting algorithm. With the current algorithm the assumptions which may cause significant measurement errors include:

- assuming the lens is aligned and can be described with a rotationally symmetric conic section for the anterior lens surface while the lens is known to be irregular (Richards et al 1988)

- assuming all of the refraction occurs at the anterior lens surface and the refractive contributions of the gradient can be replaced with a uniform equivalent refractive index

- assuming a uniform refractive index in the equatorial plane.

The combination of these assumptions produces the measurement errors in the surface curvatures and the asphericity reported by the Scheimpflug technique. Future improvements to the system will be aimed at improving the measurement error in surface curvatures and asphericities.

5.10. Summary

In this chapter we described the design and development of a Scheimpflug imaging system. The design of this system was optimized to create accurate images of in vitro lenses mounted in the EVAS II lens stretcher system. The system was calibrated on high precision stainless steel ball bearings and validated on a sample set of in vitro crystalline lenses which were imaged and measured with the Scheimpflug, shadowgraph and OCT techniques.

The main achievements of this chapter are:

- the design and construction of the Scheimpflug imaging system

- the design of a Kohler illumination system with large depth of focus

- the development of a Scheimpflug correction algorithm based on three-dimensional ray tracing, which takes into imaging an in vitro lens submerged in preservation media and the refraction at the anterior lens surface

- and the validation of the Scheimpflug lens biometry technique using steel ball bearings, glass lenses and comparison with Shadowgraph and OCT images

In Chapter 7, the Scheimpflug technique developed in this chapter will be applied to cross sectional imaging of the in vitro lens during simulated accommodation. The biometric data obtained with the Scheimpflug system will be used to develop an optical model of the crystalline lens during simulated accommodation.

CHAPTER 6. AN AGE DEPENDENT OPTICAL MODEL OF THE ISOLATED CRYSTALLINE LENS

6.1. Objective

Aim 1 of this dissertation is to develop an age-dependent optical model for the isolated human and non-human primate crystalline lens. This model is based on direct measurements of the isolated crystalline lens shape and power over a wide age range. The isolated lens shape and power corresponds to that of the maximally accommodated lens which is free of external forces. An age-dependent optical model of the isolated lens is a preliminary step in developing an optical model of the in vitro lens during simulated accommodation. Specifically this model quantifies the age-dependence of:

-the shape (thickness, diameter, and surface curvatures)

-the refractive power

-the refractive contributions of the lens surfaces to the total refractive power

-the refractive contributions of the refractive index gradient to the total refractive power

-and the equivalent refractive index

This age-dependent optical model of the isolated lens will serve as a model for the maximally accommodated lens and its changes with age which may contribute to presbyopia.

6.2. Methods

6.2.1. General description

The refractive power and shape of in vitro human and non-human primate lenses were measured on a large number of isolated crystalline lenses over a large age range (6

to 94 years in the human lenses and from 0.75 to 27 years in the non-human primates). The maximally accommodated lens refractive power was measured with three independent techniques (section 4.2). The equivalent refractive power of the isolated lens was measured with a modified commercial lensmeter and a custom designed Badal lensmeter. In the other experiment, the dioptric power of lenses maintained in their accommodative framework (with intact zonules, ciliary body, and segmented scleral rim) and mounted in the testing cell of the EVAS II lens-stretching system under no applied tension was measured with a custom designed optical system based on the Scheiner principle. The isolated lens shape was measured from undistorted cross-sectional images of the lens obtained with a shadowphotograph technique (section 4.3). The refractive contributions of the surfaces and the internal optics of the lens were determined with an optical ray tracing simulation technique which incorporates the measured lens shape and refractive power (section 4.4).

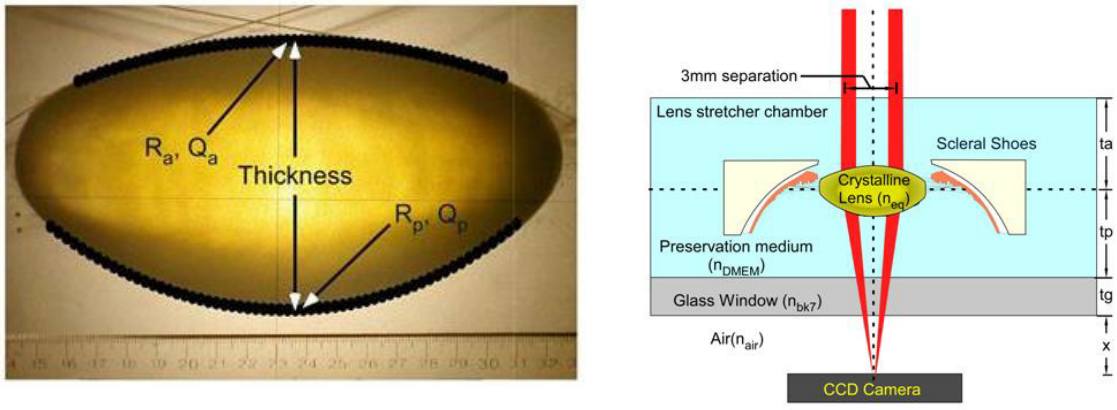

Figure 6.1: (A.) A sample shadowgraph image of a 53 year old isolated lens 2 days postmortem with the anterior and posterior surface profiles overlaid. The surface profiles were fit with conic sections to calculate the anterior and posterior radii of curvature (Ra and Rp) and asphericities (Qa and Qp). The thickness and diameter was measured directly from the images using the ruler as a calibration. (B.) *In vitro* lens power measurement with a Scheiner system (Section 4.2.3). Optical ray tracing simulation was used to evaluate an equivalent refractive index for the isolated lens measured with the Scheiner principle.

6.2.2. Donor tissue

6.2.2.1. Human tissue

All human tissue was obtained and used in compliance with the guidelines of the Declaration of Helsinki for research involving the use of human tissue. Experiments were performed on a total of 100 eyes from 72 phakic donors. The donor globes arrived in sealed, Styrofoam containers filled with ice and used between 1 and 5 days post-mortem (average: 2.8±1.6 days). The donor ages ranged from 6 to 94 years. Any lens with visible damage was excluded from the analysis (Augusteyn et al 2007). In total 24 out of the 100 lenses were discarded due to swelling from storage conditions or manipulation during the experiment.

6.2.2.2. Non-human primate tissue

All animal experiments adhered to the ARVO Statement for the use of animals in research. No animal tissue was used for the sole purpose of this study. Hamadryas baboon, cynomolgus and rhesus monkey tissue was donated by the Division of Veterinary Resources at the University of Miami as part of a tissue sharing protocol. Measurements were performed on 119 cynomolgus monkey (*Macaca fascicularis*) lenses from 65 donors within 24 hours of euthanasia (PMT = 11.8±13.7 hours, age = 2.7 to 14.3 years); 61 rhesus monkey (*Macaca mulatta*) lenses from 58 donors within 24 hours of euthanasia (PMT = 22.3±14.9 hours, age = 0.7 to 13.3 years); on 13 isolated hamadryas baboon (*Papio hamadryas*) lenses from 13 donors within 24 hours of euthanasia (PMT = 12.1±14.8 hours, ages = 5.4 to 27.3 years). Any lens with visible damage was excluded from the analysis (Augusteyn et al 2007).

6.2.3. Data and statistical analysis

There was a correlation ($r>0.65$, $p<0.05$) for the biometric and optical properties between the left and right eye from the same donor. Therefore to prevent values obtained from paired eyes biasing the statistics for age dependence, the values from left and right eyes of each donor were averaged. The average values were then used as a single point for age dependence calculations.

Each measured parameter was analyzed with a single or piecewise linear regression to determine age-dependence. A p-value of 0.05 was set as the condition for statistical significance. For the piecewise linear regressions, each data set was tested against a bi-linear model (Borja et al. 2008) using an iterative computational (non-linear regression) technique to find the break point age which divided the data set into two subsets a "lower age group" and an "upper age group". The non-linear growth parameters such as the lens thickness, diameter and volume were analyzed with an exponential growth function. A p-value of 0.05 was set as the condition for statistical significance. For each donor the OD and OS average value for each parameter was used as a single data point to characterize age dependence.

6.3. Results

6.3.1. General trends

Over the sampled age range of the human isolated lenses (6-94 years), the age dependence of equatorial diameter, central thickness, equivalent power, surface refractive power, and equivalent refractive index as well as the anterior and posterior surface curvatures appeared to be non-linear with a transition occurring approximately within the period of presbyopia onset (40-60 years). Given these apparently non-linear trends, the

age dependencies of all measured parameters were analyzed with a bi-linear model (Borja et al 2008). The bi-linear model determined the age range where a transition in age dependencies occurred.

The age-dependent trends of the non-human primate lens were similar to those of the young pre-presbyopic human lens. In general, both the pre-presbyopic human and non-human primates displayed a dramatic decrease in refractive power, flattening of the surfaces, thinning of the lens and increase in equatorial diameter (Figure 6.2).

6.3.2. Lens growth

The continual growth of the lens can be monitored from the biometric measurements of lens central thickness, equatorial diameter and the caluclated lens volume. The age dependent linear regressions of these parameters provide a description of the changes in the lens associated with aging and the onset of presbyopia (Table 6.1). The central lens thickness and equatorial diameter of isolated human lenses showed a bi-phasic age-dependence with a transition occurring between 27 to 28 years of age (Figure 6.3). Initially, the young pre-presbyopic human isolated lens grows primarily in the equatorial direction. In the lower age group, from 6 to 27 years of age, central lens thickness decreased at a rate of -0.03 mm per year and equatorial diameter increased at a rate of 0.04 mm per year. In the upper age range, the isolated human lens grows in the sagittal direction. From 27 to 94 years of age, central thickness increases at a rate of 0.02 mm per year. In this upper age range the equatorial diameter increases slowly at a rate of 0.01 mm per year.

The central thickness and equatorial diameter of the isolated non-human primate crystalline lens showed similar age dependent trends as the young human lens (Figure 6.2

and Table 6.1). Generally, over the sampled age range, the non-human primate lens equatorial diameter increased and the central lens thickness decreased. Central lens thickness is expected to increase in the older isolated non-human primate lens, similar to the trends observed in humans. However, this trend was not observed in this study due to the limited number of non-human primate samples in the presbyopic age range.

The equatorial diameter and volume of the isolated rhesus monkey lens displayed a non-linear growth in the measured age range which included samples less than a year old. Central lens thickness of the isolated rhesus monkey decreases linearly ($p<0.001$) at a rate of -0.08mm / year throughout the measured age range (Table 1). The cynomolgus monkey and hamadryas baboon isolated lenses both decrease linearly in central thickness (-0.036 and -0.05 mm/year respectively) and increase linearly in equatorial diameter (at a rate of 0.06 and 0.07mm/year respectively) throughout the sampled age range (Table 6.1).

The lenses of the cynomolgus monkeys are smaller in diameter and slightly thicker than comparably aged hamadryas baboon and rhesus monkey lenses. The cynomolgus monkey lenses are also slightly smaller in total volume than the other three primate species including the human lenses. The size and volume of the hamadryas baboons and the rhesus monkeys are similar to those of the young human lenses (Table 6.1).

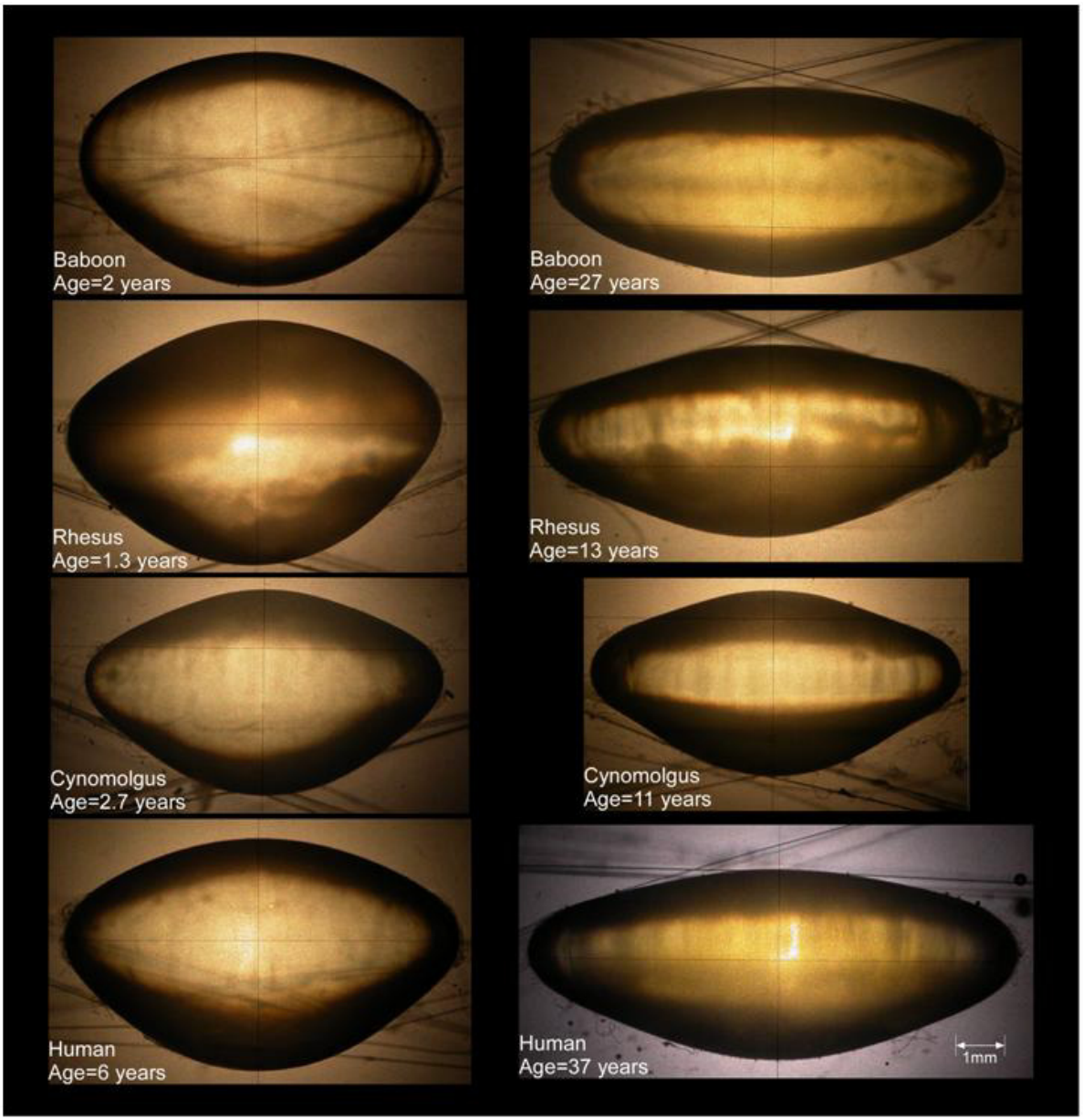

Figure 6.2: Sample sagittal (side view) shadowgraph images of young (left) and older (right) lenses from hamadryas baboons, rhesus and cynomolgus monkeys are compared with young and older human lenses (Borja *et al.* 2008). All images are at the same scale and show the crosshairs of the optical comparator and the supporting suture mesh of the immersion cell.

Species **Age Range**	**Human** (6-94 years)		**Hamadryas Baboon** (1.67 to 27.3 years)	**Cynomolgus Monkey** (1.7 to 14.3 years)	**Rhesus Monkey** (0.7 to 13.3 years)
	Lower Age Group	Upper Age Group			
Central Thickness (mm)	4.96-0.04·Age n=7, p=0.004 (6-27 years)	3.62+0.02·Age n=53, p<0.001 (27-94 years)	4.64-0.04·Age p=0.002	4.33-0.05·Age p<0.0001	4.93-0.078·Age p<0.0001
Equatorial Diameter (mm)	7.91+0.04·Age n=8, p=0.014 (6-28 years)	8.89+0.01·Age n=43, p=0.001 (28-94 years)	7.59+0.06·Age p<0.0001	6.92+0.07·Age p<0.0001	$\frac{8.82}{1+e^{-0.3(Age+4.7)}}$ r^2<0.80, χ^2=0.084
Diameter / Thickness (Aspect ratio)	1.90+0.05·Age n=8, p=0.014 (6-55 years)	2.79-0.01·Age n=43, p=0.001 (55-94 years)	1.63+0.03·Age p<0.0001	1.58+0.04·Age p<0.0001	1.46+0.07·Age p<0.0001
Calculated Volume (mm^3)	154.74+1.1·Age p<0.001		140.5+1.24·Age p=0.0026	112.59± 8.12 p=0.136	$\frac{162.8}{1+e^{-2.7(Age-0.13)}}$ r^2<0.83, χ^2=49.0

Table 6.1: Growth of the *in vitro* (maximally accommodated) lens. This table presents the age-dependent linear regression equations for lens thickness, diameter, and volume as well as the diameter to thickness ratio for *in vitro* human and non-human primate lenses.

A.

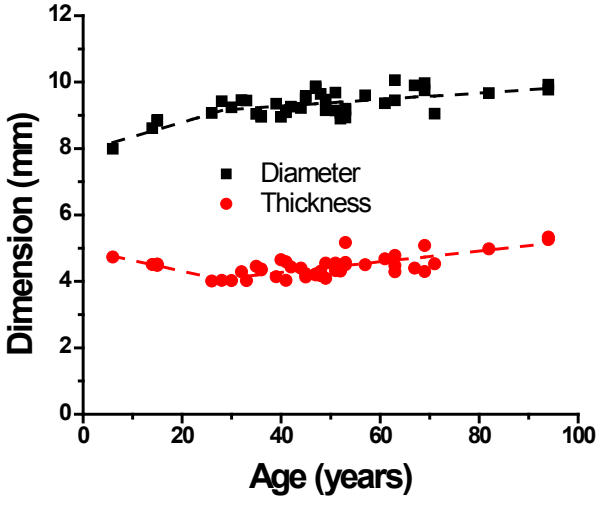

B.

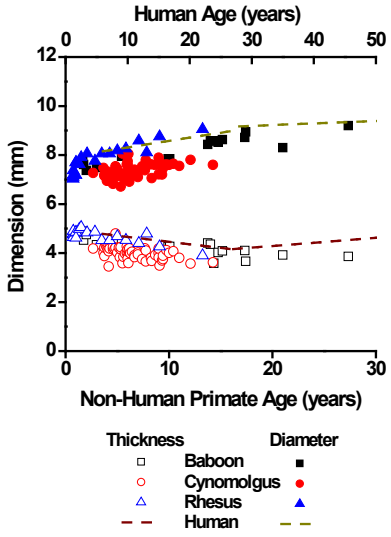

Figure 6.3: Age-dependent lens thickness and diameter of isolated human (A), hamadryas baboon, cynomolgus and rhesus monkey (B.). An age-conversion factor of 2.5 non-human primate to human years was used to compare the growth patterns of both groups.

A.

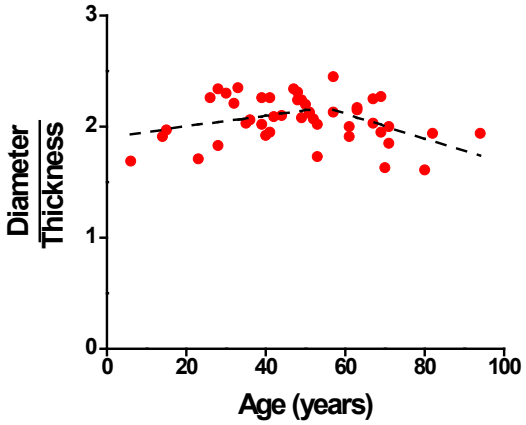

B.

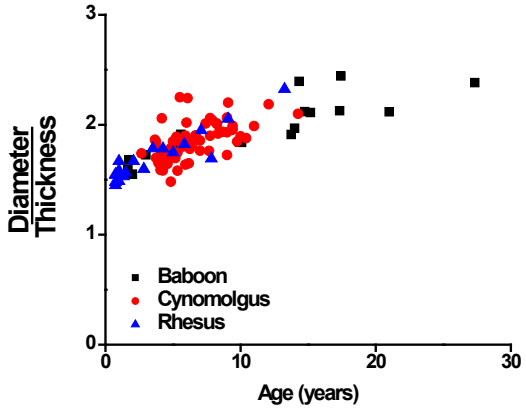

Figure 6.4: The ratio of the lens equatorial diameter to central thickness of the isolated human (A.), and non-human primates (B.) lenses. The maximally accommodated lens grows primarily in the equatorial direction prior to the onset of presbyopia. After which the lens central thickness increases while the lens diameter remains relatively constant. The young non-human primates demonstrate similar growth patterns as the pre-presbyopic humans.

A.

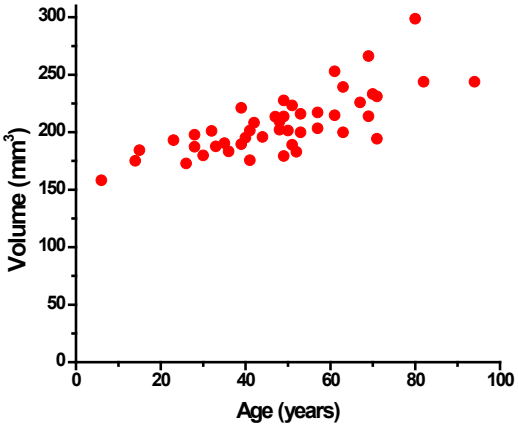

B.

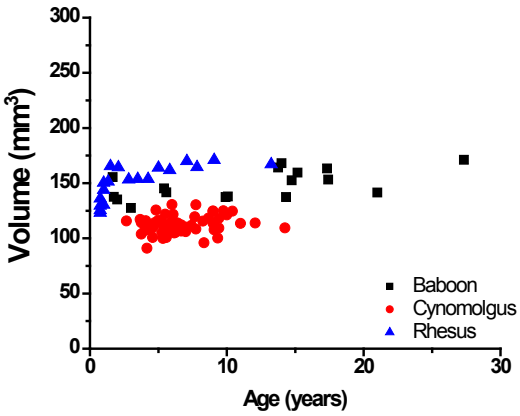

Figure 6.5: The calculated volume of isolated human (A), hamadryas baboon, cynomolgus and rhesus monkey (B.) lenses as a function of age shows the continual growth of the isolated lens throughout the measured age ranges. The cynomolgus monkey lenses were significantly smaller than comparably aged rhesus monkey and hamadryas baboon lenses.

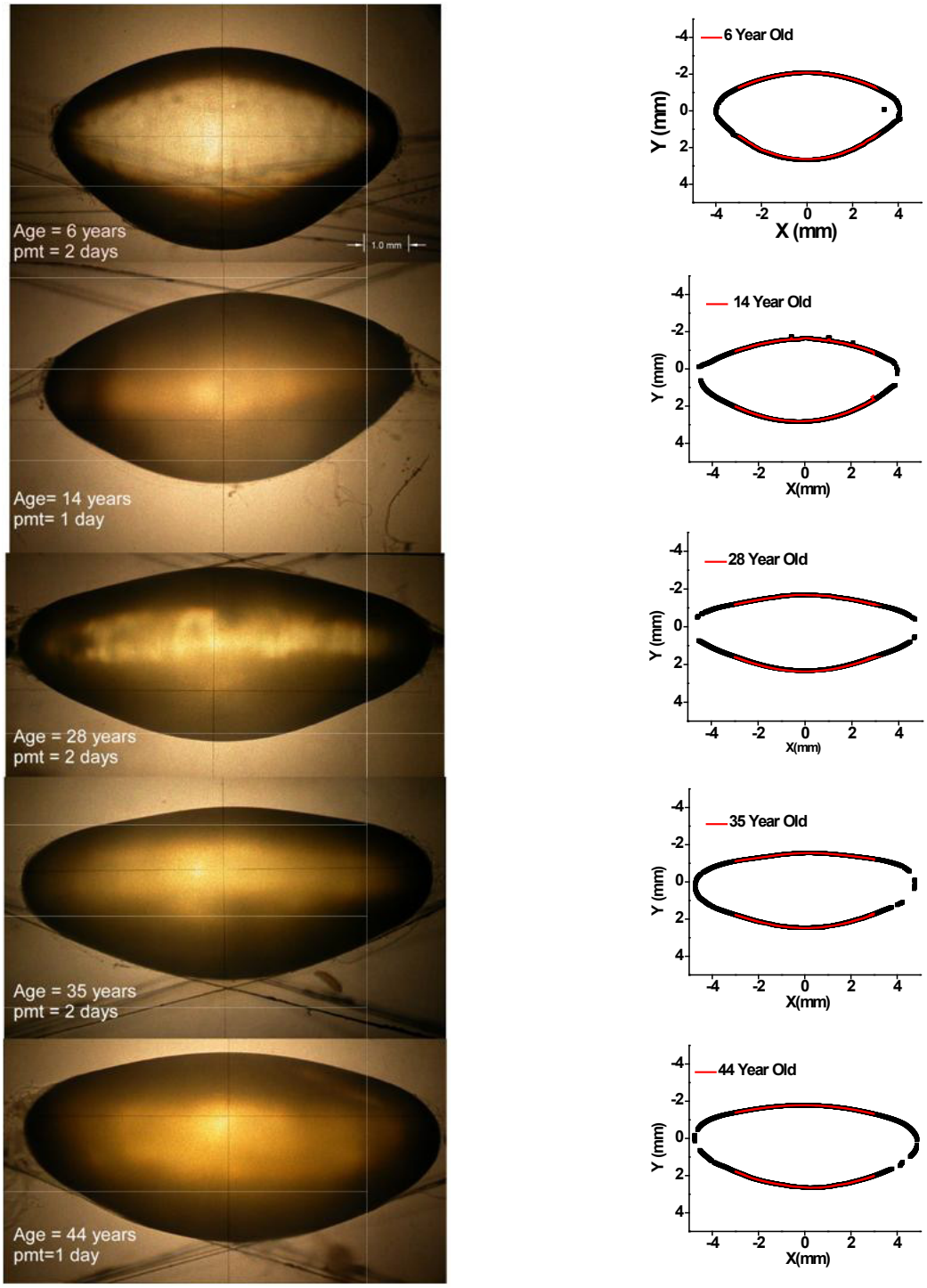

Figure 6.6: Shadowgraph images depicting the growth of the human lens from 6 to 44 years of age. The isolated lens grows in the equatorial direction from birth to 27 years of age.

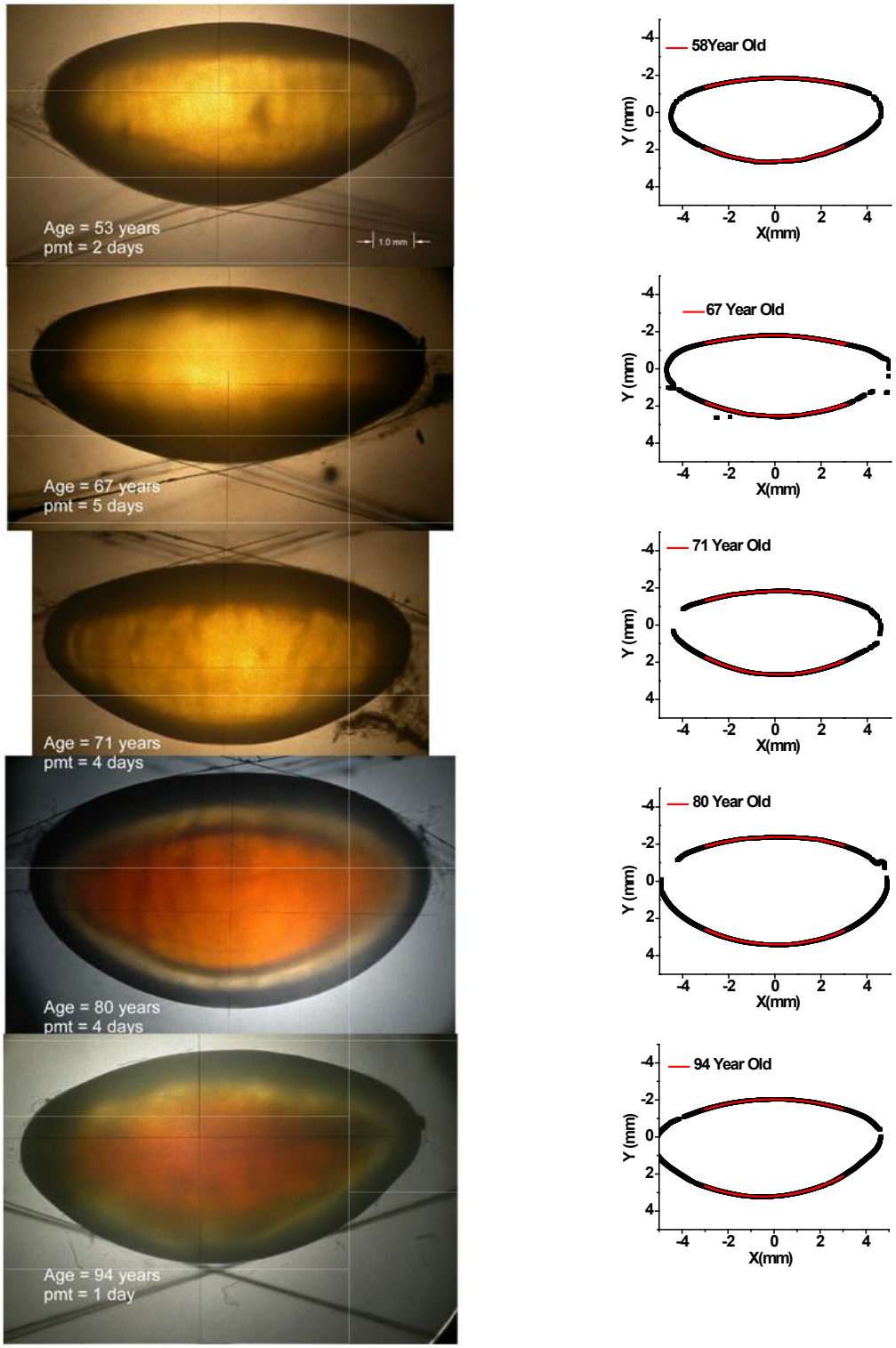

Figure 6.7: Shadowgraph images depicting the growth of the post-presbyopic human lens between 53 and 94 years of age. In this age range the growth of the isolated lens is primarily in the axial (thickness) direction.

6.3.3. Surface curvatures of the isolated in vitro lens

The surface curvatures of the human and non-human primate isolated lenses displayed non-linear age dependent trends (Figure 6.8 and Table 6.2). The human lens anterior surface asphericity showed a biphasic trend with a break-point age similar to those of the thickness and diameter (26-28 years of age). The age-dependencies for surface curvatures and asphericities in the non-human primate lenses are similar those of the lower age group in the human lenses. Overall, these results indicate that the pre-presbyopic lens flattens with age until the onset of presbyopia, after which the lens surfaces become slightly more prolate with shorter radii of curvatures and a positive shift in asphericity.

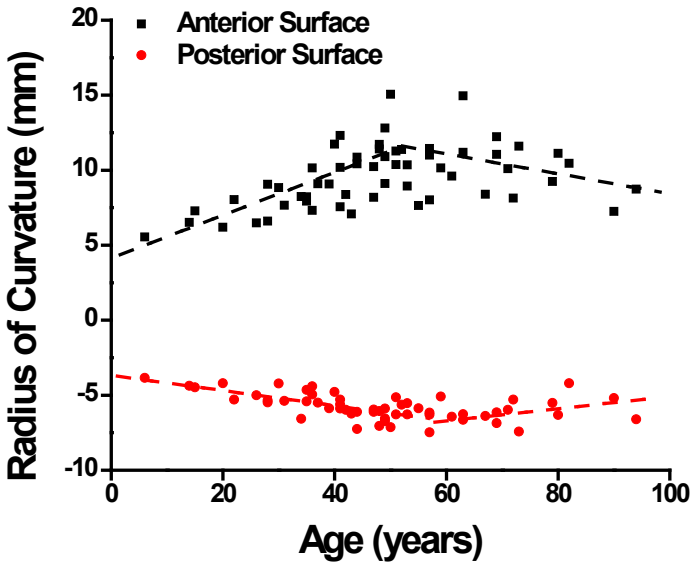

Figure 6.8: The radii of curvature of the isolated *in vitro* lens correspond to that of the maximally accommodated lens. From this graph and Figures 6.6 and 6.7 it can be seen that the lens surfaces flatten in the lower age range. In the upper age range the human lens surface curvatures slightly steepen. The equations for the regression lines are given in Table 6.2.

The anterior and posterior radii of curvature for all three non-human primate species flattened with age (Figure 6.9 and Table 6.2). In the hamadryas baboon the anterior surface curvatures remained relatively constant in the first decade of life, after which the anterior surface curvature increases at a rate of 0.5mm/year. This transition occurs at 14.7 years of age. The baboon anterior surface curvature showed an age dependent increase. However, this trend was not statistically significant. The surface curvatures of the cynomoglus monkey lens increased linearly throughout the sampled age range.

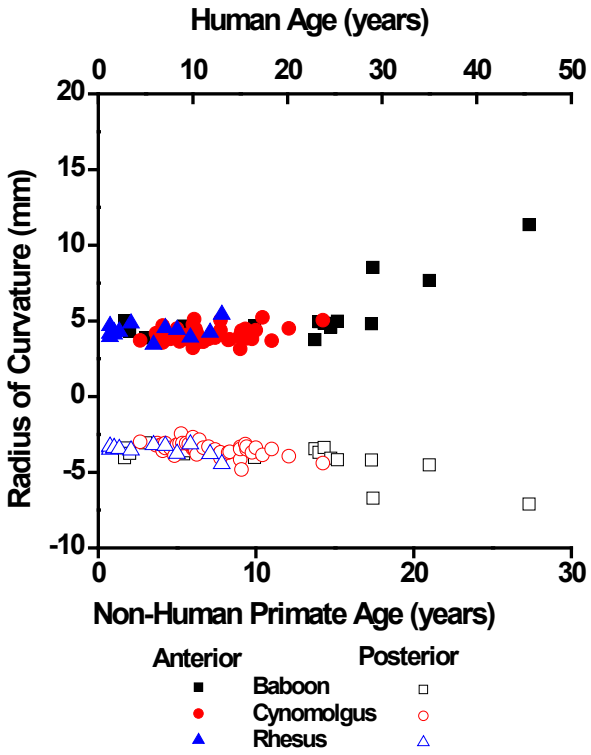

Figure 6.9: Anterior and posterior surface curvatures of *in vitro* isolated hamadryas baboon, cynomolgus and rhesus monkey lenses as a function of age. A bi-linear trend was observed for the baboon lens anterior radii of curvature as well as for the anterior and posterior radii of curvature of the rhesus lenses (Table 6.2). An age-conversion factor of 2.5 non-human primate to human years was used to compare the age-dependent trends of both groups.

A.

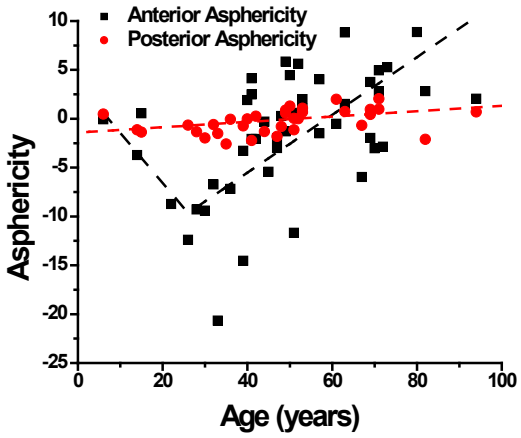

B.

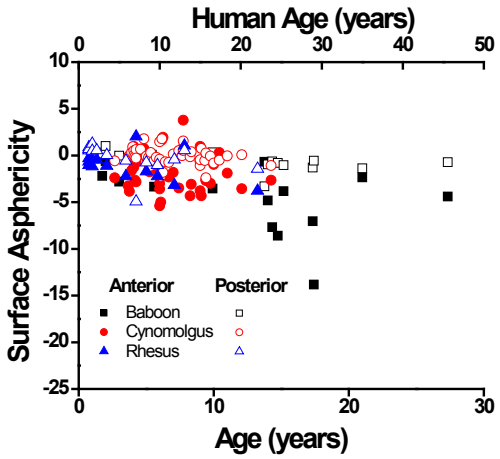

Figure 6.10: *In vitro* lens anterior and posterior surface asphericity for human (A) and non-human primate lenses (B.). The maximally accommodated human and non-human primate anterior lens surface transitions from a parabolic shape (p=0), in the youngest lenses, to hyperbolic shape (p<1) in the age range of presbyopia onset. After the onset of presbyopia, the human lens anterior surface transitions into a prolate shape (p>1).

Species **Age Range**	**Human** (6-94 years)		**Hamadryas Baboon** (1.7 to 27.3 years)		**Cynomolgus Monkey**	**Rhesus Monkey**
	Lower Age Group*	Upper Age Group*	Lower Age Group*	Upper Age Group*	(1.7 to 14.3 years)	(0.7 to 13.3 years)
-----Anterior-----						
Radius of Curvature (mm)	4.46 + 0.14·Age (6 to 50 years) n=26, p<0.001	13.83-0.05·Age (50 to 94 years) n=21, p=0.03	4.81±0.27 (1.7-14.7 years) n=7, p=0.93	-2.54+0.51·Age (14.7 – 27.3 years) n=6, p=0.023	3.66+0.06·Age p=0.04	4.68±1.10 p=0.36
Surface Asphericity	4.84-0.56·Age (6 to 26 years) n=6, p=0.02	-14.7+0.25·Age (26 to 94 years) n=42, p<0.001	-0.89–0.25·Age p=0.01		-1.62 ± 1.96 p=0.60	-0.98 ± 1.38 p=0.34
-----Posterior-----						
Radius of Curvature (mm)	-3.47-0.06·Age (6 to 57 years) n=34, p<0.001	-7.97 + 0.02·Age (57 to 94 years) n=14, p=0.03	-3.03-0.09·Age p=0.01		-2.80–0.09·Age p<0.0001	-3.27-0.08·Age p<0.001
Surface Asphericity	-1.42+0.027·Age p=0.005		0.29-0.06·Age p=0.002		-0.11 ± 0.89 p=0.140	0.52 - 0.23·Age p=0.057

Table 6.2: Age-dependent linear regression equations of the measured non-human primate *in vitro* lens biometric properties. * Linear regressions for an upper and lower age group are given separately when the break point analysis was statistically significant.

6.3.4. Effective refractive power

Figure 6.11 shows the measured in vitro isolated refractive power as a function of age. Over the sampled age range the human and non-human primate lens equivalent refractive power decreases by over 30D. In the human lens a bi-phasic age dependence trend was observed, with the transition occurring after the onset of presbyopia (between 55-58 years of age). A bi-linear model showed the power initially decreases approximately linearly. After this initial linear decrease there is a trend for the refractive power to increase in the older presbyopic human lenses. This same trend has been reported by Glasser and Campbell (1999) for lenses older than 65 years in a study on 19 isolated human lenses with ages ranging from 5 to 96 years of age. Glasser and Campbell modeled this non-linear age dependence with a 2^{nd} order polynomial function which also fits well with the results from this study.

In the non-human primates the equivalent refractive power decreased by over 30 D over the sampled age range (Table 6.3). Compared to the human lenses included in this study, the sampled age range of the non-human primates is skewed to the young pre-prebyopic range (age<15 years). The power decrease in the non-human primate lens can be approximated as linear in the sampled age range. There was an insufficient number of older non-human primate samples to determine if there was a non-linear trend in isolated lens effective refractive power.

These results indicate the refractive power of the maximally accommodated lens decreases with age until the onset of presbyopia, after which the lens undergoes a transition which slightly increases its equivalent refractive power.

A. B.

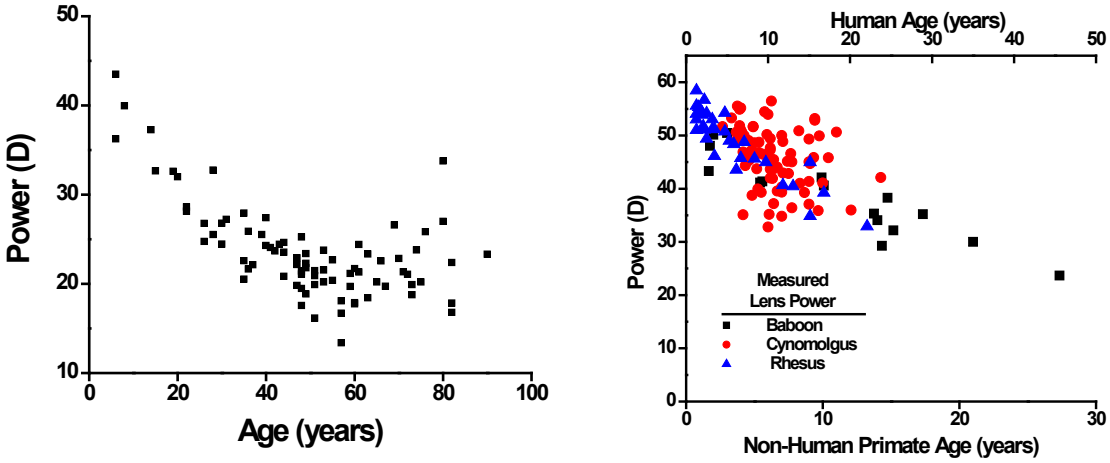

Figure 6.11: A. *In vitro* isolated human lens effective refractive power measured at 1.5mm from the center of the lens (3mm entrance pupil diameter). The results showed a non-linear age dependence for in vitro human lens refractive power with a transition occurring around the age range of presbyopia onset. B. In vitro non-human primate effective refractive power. These results showed a linear decrease in refractive power over the measured age range.

Species / **Age Range**		**Human** (6-94 years)		**Hamadryas Baboon** (1.7 to 27.3 years)	**Cynomolgus Monkey** (1.7 to 14.3 years)	**Rhesus Monkey** (0.7 to 13.3 years)
Power (D)		Lower Age Group	Upper Age Group			
Entrance Pupil Diameter	3mm	41.59 – 0.41·Age (6 to 58 years) r = -0.92, p<0.0001 n=24	-1.34 + 0.33·Age (58 to 82 years) r = 0.63, p=0.002 n=21	52.45– 1.3·Age r = -0.87, p<0.0001 n=17	53.18 - 1.2·Age r=-0.39, p<0.0001 n=88	54.22- 1.8·Age r=-0.78, p<0.0001 n=28
	4.42mm	40.77 – 0.41·Age (6 to 55 years) r = -0.86, p<0.0001 n=32	12.8+ 0.10·Age (55 to 90years) r = 0.20, p=0.5 n=15	50.85 - 1.5·Age r=-0.93, p<0.0001 n=10	55.25 - 1.3·Age r=-0.71, p<0.0001 n=68	57.11 - 2.9·Age r=-0.87, p=0.01 n=7
	5.68mm	32.23 – 0.26·Age (6 to 55 years) r = -0.68, p<0.0001 n=32	11.87+ 0.11·Age (55 to 90 years) r = 0.22, p=0.43 n=14	41.3 - 1.3·Age r=-0.95, p<0.0001 n=10	41.63 - 1.1·Age r=-0.55, p<0.0001 n=69	46.65 - 2.7·Age r=-0.79, p=0.04 n=7

Table 6.3: Age-dependent linear regression equations of the measured human and non-human primate *in vitro* lens equivalent refractive power. In vitro effective refractive power was measured at three different entrance pupil diameters. In general, the refractive power of the lens decreased with increasing entrance pupil diameter. Refractive power decreased with age in all four species. A slight increase in human lens refractive power was observed after the onset of presbyopia. This trend was not observed in the pre-presbyopic non-human primate sample age range.

In the human, baboon and cynomolgus monkey lenses there was no statistically significant difference between the power measurements obtained at 3mm and 4.42mm entrance pupil diameter ($p=0.5$, $n=36$, $t=0.45$). However, the refractive power measured at 5.68mm is significantly lower than the refractive power measured at the 3 and 4.42mm entrance pupil diameters. These results indicate the lens equivalent refractive power can be considered constant over the central optical zone and decreases at entrance pupil diameters larger than 4.42mm.

6.3.5. Refractive contributions of the surfaces

The refractive power of the crystalline lens is a sum of the surface refractive power and the refractive contributions of the lens internal refractive index gradient. In this section the refractive contributions of the isolated lens aspheric surfaces were quantified to indirectly determine the refractive contributions of the lens internal refractive index gradient.

The surface refractive power was calculated for each measured lens assuming a uniform refractive index equal to the cortex refractive index. The refractive index of the cortex was assumed to be $n=1.3709$ (Jones et al 2005) independent of age. The measured aspheric surface curvatures and thickness of each lens were entered into an optical ray tracing software program. This program calculated the surface refractive power for each lens.

The surface refractive power of the human and non-human primate lens as a function of age is presented in Figure 6.12 and Table 6.4. In the human and non-human primate isolated lens the refractive power of the surfaces decreases only slightly with age, despite large changes in lens thickness and surface curvatures over the sampled age

ranges. A bi-phasic transition was detected for the human lens surface refractive power. In the lower age group (from 6-55 years of age) the human lens surface refractive power decreased linearly. After the break-point age, the surface refractive contributions increased slightly. The surface refractive power of the non-human primate lenses decreased linearly with age in all three species.

In the human lens the refractive power of the lens surfaces decreases only slightly with age (Figure 6.12). The age-dependent decrease of the *in vitro* lens power is therefore, due mainly to changes of the internal structure of the lens including the cortex. We find that the surface refractive contribution as a percentage of the total lens power increases with age from 26 to 55% of the total lens power. The bi-linear model showed there was no statistically significant ($p=0.74$) break point age for the relative surface refractive contributions. There was however a statistically significant increase in the relative refractive power contribution from the lens surfaces with age (Figure 5.13 and Table 5.4). The surfaces provide from 41% (at 6 years) to 55.1% (at 82 years) of the total refractive power of the isolated human lens.

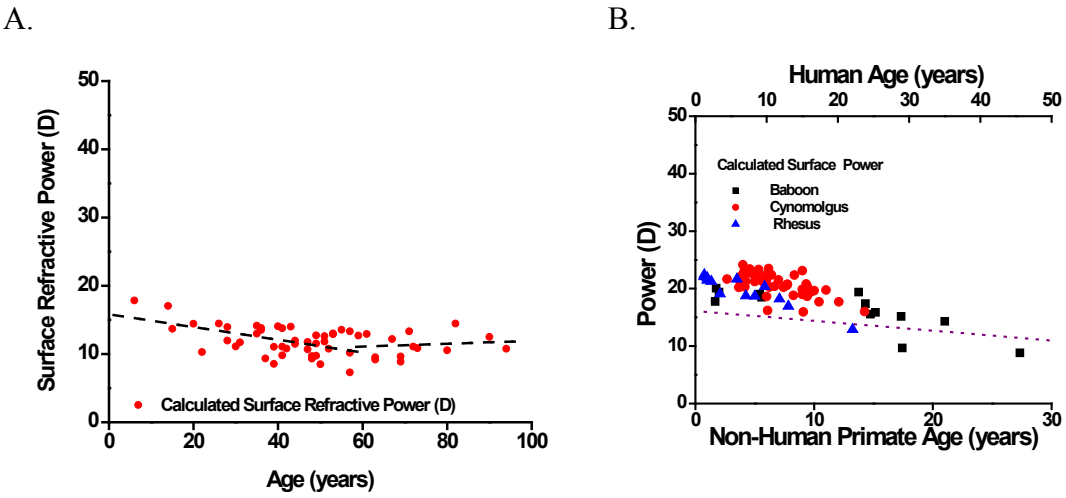

Figure 6.12: The surface refractive power age-dependence for the human (A.) and non-human primate (B.) isolated lens. The age dependence of the human lens surface refractive power is bi-phasic with a transition occurring at 55 years of age. The non-human primate lens surface refractive power decreased linearly with age. The equation for the regression line is given in Table 6.4. An age-conversion factor of 2.5 non-human primate to human years was used to compare the age-dependent trends of both groups.

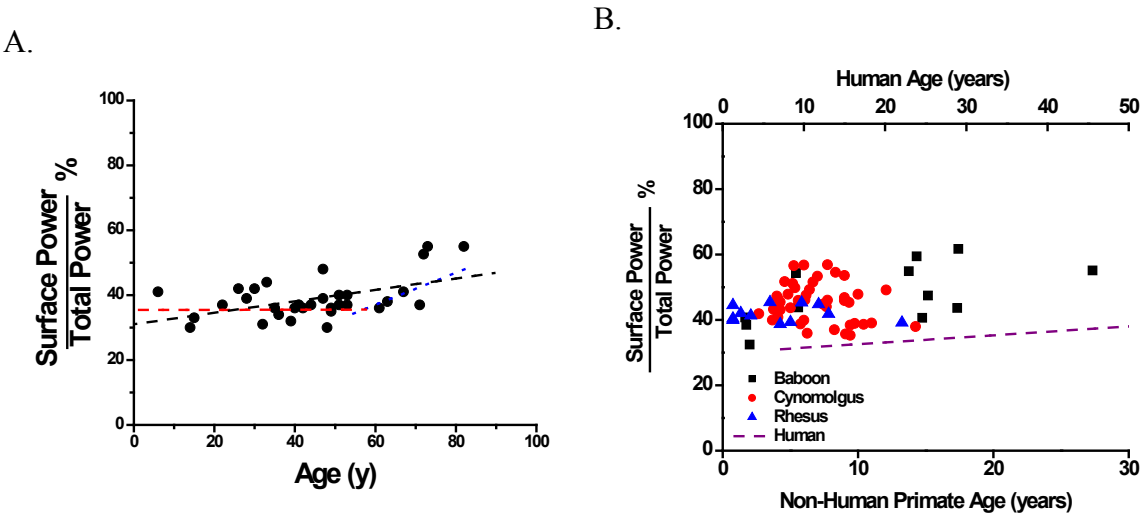

Figure 6.13: The relative surface refractive contributions to the total *in vitro* lens refractive power as a function of age. The equation for the regression line is given in Table 6.4. Compared to the human lenses the surfaces of the non-human primate lenses contribute a larger proportion of refractive power to the total lens refractive power.

Species **Age Range**	**Human** (6-94 years)		**Hamadryas Baboon** (1.7 to 27.3 years)	**Cynomolgus Monkey** (1.7 to 14.3 years)	**Rhesus Monkey** (0.7 to 13.3 years)
	Lower Age Group*	Upper Age Group*			
Surface Refractive Power (D)	15.83-0.10·Age (6 to 55 years) n=39	11.27±1.95·Age (55 to 94 years) n=18	21.56-0.37·Age r=-0.84, p<0.0001 n=14	26.28-0.46·Age r=-0.34, p=0.004 n=68	22.86-0.74·Age r=-0.92, p<0.0001 n=14
Surface Refractive Contribution (%)	30.67+ 0.17· Age p= 0.0031 n =41		38.40 + 0.62·Age r=0.58, p=0.030 n=14	45.29 ± 5.85 p=0.268	41.89 ± 2.50 p=0.710

Table 6.4: Age-dependent linear regression equations of the calculated surface refractive power for the human and non-human primate *in vitro* lens.

6.3.6. Refractive contributions of the gradient

The refractive power of the crystalline lens is the sum of the surface refractive power and the refractive contributions of the lens internal refractive index gradient. In this section the refractive contributions of the internal refractive index gradient is quantified.

The refractive contribution of the lens internal refractive index gradient is quantified in this study as an equivalent refractive index (section 4.4.3). The equivalent refractive index of the baboon and rhesus monkeys were calculated at the 3mm entrance pupil diameter. The human and cynomolgus monkey equivalent refractive indices were calculated at three entrance pupil diameters (3, 4.42, and 5.68mm). There was no statistically significant difference between the refractive index measured at 3 and 4.42mm in the human and cynomolgus lenses. For both species the refractive index measurements at 5.68mm were significantly lower than those measured at 3 and 4.42mm. Figure 6.14

shows the age dependence of the human and non-human primate lens equivalent refractive index.

The human lens equivalent refractive index showed a non-linear age dependence. For the equivalent refractive index the bi-linear model showed a statistically significant ($p<0.028$) break-point age of 60 years for the calculated human lens equivalent refractive index (Table 6.5). In the lower age group the equivalent refractive index decreased at a rate of -3.90×10^{-4}/year independent of entrance pupil diameter. At the break point age the equivalent refractive index value was between 1.4085 and 1.3995 depending on entrance beam diameter. In the upper age range the equivalent refractive index remains relatively constant with age.

No age-dependent trend was observed in the relative surface refractive contributions or in the equivalent refractive index in the rhesus or the cynomolgus monkey. This difference in the age dependence is probably due to the smaller age range of the cynomolgus and rhesus monkey lenses which were available for this study.

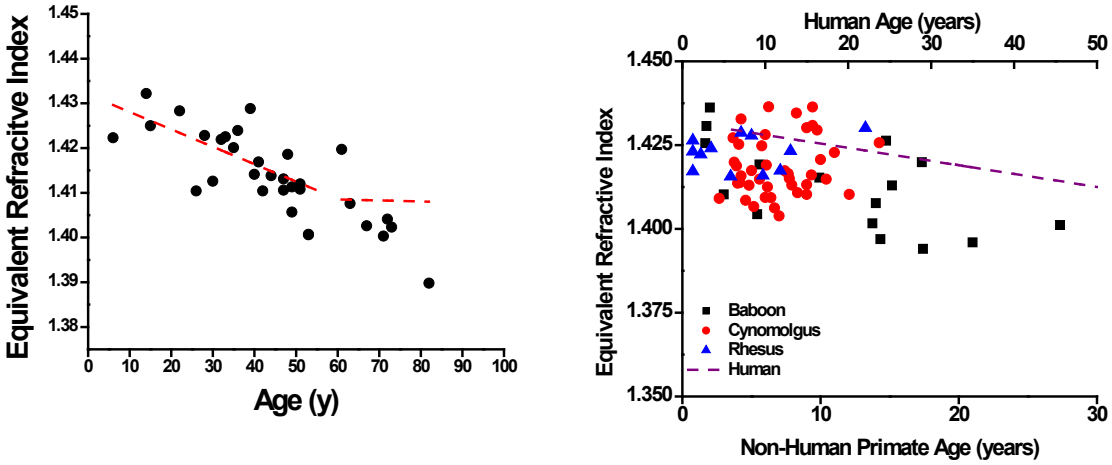

Figure 6.14: The equivalent refractive index of the human (A.) and non-human primate (B.) lens as a function of age.

Species **Age Range**		**Human** (6-94 years)		**Hamadryas Baboon** (1.7 to 27.3 years)	**Cynomolgus Monkey** (1.7 to 14.3 years)	**Rhesus Monkey** (0.7 to 13.3 years)
Equivalent Refractive Index		Lower Age Group	Upper Age Group			
Entrance Pupil Diameter	3mm	$1.432 - 3.90\times10^{-4}\cdot$Age (6 to 60.4 years) r = -0.92, p<0.0001 n=24	$1.410 - 1.8\times10^{-5}\cdot$Age (60.4 to 90 years) r = 0.63, p=0.002 n=21	$1.425–1.1\times10^{-3}\cdot$Age r = -0.64, p=0.007 n=17	1.425 ± 0.010 r=-0.22, p=0.18 n=37	1.423 ± 0.005 r=-0.24, p=0.45 n=12
	4.42mm	$1.432 – 3.94\times10^{-4}\cdot$Age (6 to 60 years) r = -0.50, p=0.004 n=30	1.400 ± 0.010 (60 to 90years) r = 0.007, p=0.98 n=9		1.421 ± 0.007 r=-0.13, p=0.285 n=67	
	5.68mm	$1.422 - 3.87\times10^{-4}\cdot$Age (6 to 60 years) r = -0.37, p=0.004 n=32	1.395 ± 0.010 (60 to 90 years) r = -0.004, p=0.43 n=8		1.403 ± 0.009 r=-0.19, p=0.12 n=66	

Table 6.5: Age-dependent linear regression equations for the equivalent refractive index.

6.4. Discussion

6.4.1. General findings

In summary our measurements showed a decrease in the equivalent refractive index with age or, in other words the contribution of the gradient refractive index distribution decreases. One of the implications of the decrease in equivalent refractive index with age is that the use of fixed equivalent refractive index value to calculate lens power using the lens maker formula will underestimate the power of young lenses and overestimate the power of old lenses. Furthermore an error maybe induced in central lens thickness and posterior radius of curvature calculations when a fixed equivalent refractive index is used (Garner 1997, Garner and Yap 1997) during analysis of in vivo phakometry

or Scheimpflug images. Our measurements confirm that the power and shape of the *in vitro* lens correspond to that of the *in vivo* maximally accommodated lens.

The age-dependence of optical and biometric properties in all three non-human primate species are similar to those found in isolated human lenses. In all species, we find an age dependent flattening of the lens surfaces and a decrease in refractive power.

6.4.2. Human lens equivalent refractive power

Several previous studies have shown that the isolated lens power decreases with age. Jones *et al* (2005) found that the decrease in lens power followed a linear trend over the entire age range of their samples (7 to 82 years). Our study included a larger number of lenses, particularly in the presbyopic age range. With the larger sample size, we find that the age related changes in total power of the *in vitro* lens is bi-phasic, with the transition occurring around or towards the end of the age range of presbyopia onset. The power initially decreases approximately linearly. After this initial linear decrease there is a trend for both the total power and the calculated surface power to increase in the older presbyopic lenses. This same trend has been reported by Glasser and Campbell (1999) for lenses older than 65 years in a study on 19 isolated human lenses with ages ranging from 5 to 96 years of age (Figure 6.15). Glasser and Campbell (1999) attribute this increase to the inclusion of lenses with early stages of cataract. In our study 11 out of 40 lenses over the age range 58-94 had some stage of cataract, as evaluated subjectively by grading the color of the lens in the shadowgraph images. On average the power and the surface contribution of the cataractous lenses was higher even though the difference was not statistically significant. This confirms that the increase in power in older lenses may be due to the effect of cataract formation.

Even though the general trends in our study were similar to those observed by Jones *et al* (2005) the isolated lens power values obtained by Jones *et al* (2005) were significantly higher than our values (by 6.8D for a 20 year old lens and by 8.3D for a 60 year old lens) as well as the values of Glasser and Campbell (1999) (by 7.8 for a 20 year old lens and by 8.3D for a 60 year old lens) and of Schachar (2004). Jones *et al.* (2005) recognized that their lens power is higher than expected. They attributed this difference to a potential increase in lens power beyond maximal accommodation when the lens is removed from the eye. The fact that our results are in excellent agreement with the measurements of Glasser and Campbell (1999), as well as with *in vivo* measurements (Graner et al 1992, Zadnik et al 1993, Hemenger et al 1995 and Goss et al 1997), suggests that the values obtained by Jones *et al.* (2005) overestimated the power of the isolated lens. Our findings suggest that removing zonular tension does not increase the power of the lens significantly compared to the maximally accommodated *in situ* lens.

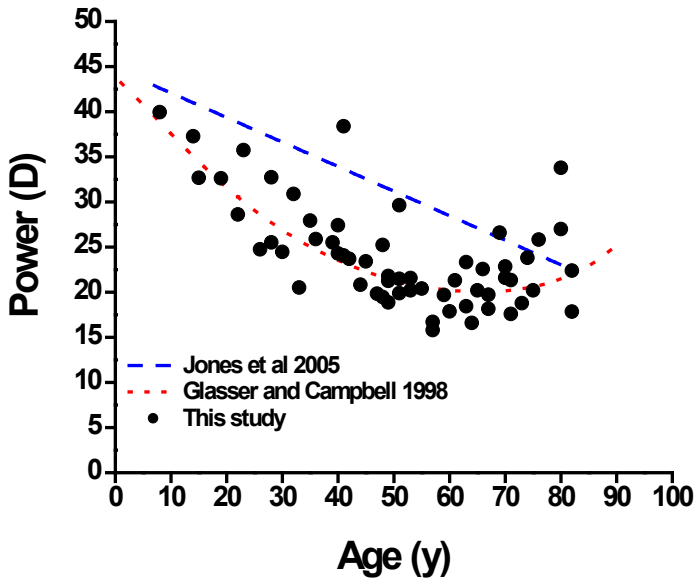

Figure 6.15: Comparison of isolated lens power results from this study with previously published data on the age dependence of the lens power.

The in vitro lens refractive power was measured at three different entrance pupil diameters with three separate measurement systems (Section 4.2). In general, the refractive power of the crystalline lens decreased with increasing entrance pupil diameter. The age dependent decrease in refractive power was observed in all of the power measurement systems independent of entrance pupil diameter. For each species, the age dependent rate of decrease in refractive power was independent of entrance pupil diameter or measurement system. This result indicates the age dependent decrease in refractive power occurs uniformly throughout the lens.

6.4.3. The refractive contributions of the human lens gradient refractive index

The contribution of the gradient refractive index of the lens to the total lens power is often quantified using the concept of an equivalent refractive index. In a longitudinal study of school age children, Mutti *et al.* (1995) showed that the equivalent refractive index between 5 and 16 years of age is approximately constant with an average value of 1.427. Dubbelman and Van der Heijde (2001) found that the equivalent refractive index decreases with age in the adult eye with values ranging from approximately 1.441 to 1.418 in the age range of 16 to 65 years. Glasser and Campbell (1998, and 1999) calculated the equivalent refractive index of isolated lenses from ray tracing experiments. They did not find a change with age. Their mean equivalent refractive index value was 1.4257±0.0163. Glasser and Campbell may not have been able to find an age dependence in equivalent refractive index due to their smaller sample size (n=19). We find that the equivalent refractive index decreases with age from a maximum of 1.437 for a 14 year old lens to a minimum of 1.396 for an 82 year old lens.

Our results show the same trend, with a similar decay rate as the study of Dubbelman and Van der Heijde (2001) (Figure 6.16), but our values are slightly lower. The difference could be due to the fact that we are measuring the *ex-vivo* lens, which is expected to correspond to the maximally accommodated state, whereas Dubbelman and Van der Heijde (2001) measured the refractive index of the relaxed unaccommodated lens *in-vivo*. However, Dubbelman *et al*. (2005) find that the equivalent refractive index slightly increases with accommodation. If the difference is due to a change in accommodative state then our values should be higher. Most likely the difference is due to differences in methodology. In our study we calculated the refractive index of the lens from direct measurements of the lens power and high resolution measurements of the lens shape including lens asphericity. Even though in vitro lenses allow direct measurement, they are subject to alterations in lens shape caused storage and handling. On the other hand, accurate *in-vivo* measurements of the lens equivalent refractive index are difficult to obtain because of the uncertainty of the shape of the posterior lens surface which is imaged through the internal structure of the lens (Dubbelman and Van der Heijde 2001). Despite these potential sources of error in both in vitro and in vivo measurements there is good agreement between our *ex-vivo* results and the *in-vivo* measurements of Dubbelman and Van der Heijde (2001).

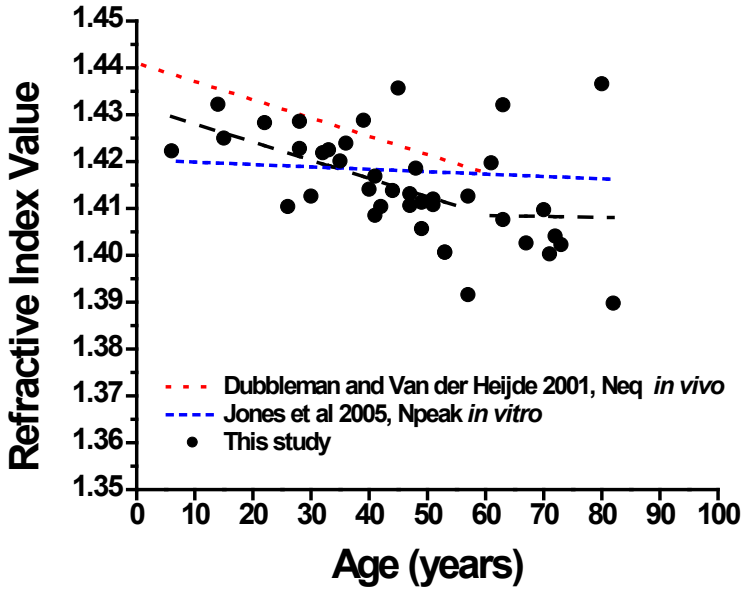

Figure 6.16: Comparison of our results with previously published data on the age dependence of the lens equivalent refractive index.

6.4.4. Age dependent shape of the isolated human lens

Our results demonstrate a biphasic age dependent trend for both anterior and posterior radii of curvatures, which confirms the findings of two previous studies (Howcroft and Parker 1977 and Glasser and Campbell 1999). Since power and radii of curvature exhibit a biphasic age-dependency, we expect to find the same trend in the equivalent refractive index and in the relative contribution of the surfaces to the lens power. The break-point age for anterior and posterior surface curvatures (50-57 years of age) correspond well with the biphasic transitions for refractive power and equivalent refractive index. There is a statistical significant breakpoint in the equivalent refractive index, but not in the relative contribution of the surface power. A larger number of samples is needed in the upper age range (above 55 years) to confirm the biphasic trend of these two parameters.

6.4.5. Implications to presbyopia

Glasser and Campbell (1998 and 1999) found that the decrease of in vitro lens power matches well with the decrease of in vivo accommodation amplitude (Duane 1912). Our results confirm these findings. This result is expected, since it is assumed that the power of the lens when accommodation is relaxed remains approximately constant with age in the adult (Hemenger et al 1995 and Atchison and Smith 2001) and the isolated lens is expected to correspond approximately to the maximally accommodated state. The decrease in accommodation amplitude in the adult must therefore correspond directly to a decrease in the power of the maximally accommodated lens (Figure 6.17). The relation between in vitro lens power and in vivo accommodation amplitude may not hold in children because there is evidence that the dis-accommodated lens power decreases with age in children (Zadnik et al 1993, Jones et al 2005 and Mutti et al 2005).

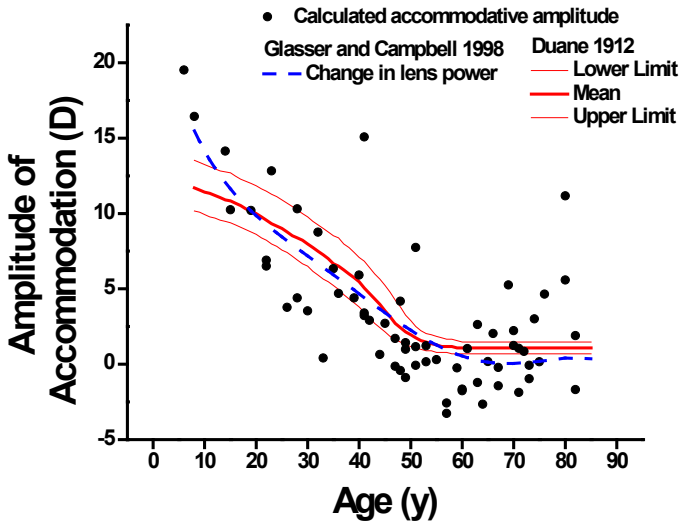

Figure 6.17: Calculated maximum possible accommodative amplitude of each measured lens power data point (n=65). The age dependent data for the in vivo amplitude of accommodation from Duane 1912 (corrected to place the reference plane at the anterior corneal surface instead of the spectacle plane) is superimposed on the graph. There is good agreement between the age dependent loss of accommodation and the maximum amplitude of accommodation calculated from the isolated lens power.

Glasser and Campbell (1999) attribute this increase to the inclusion of lenses with early stages of cataract. In our study 11 out of 40 lenses over the age range 58-94 had some stage of cataract, as evaluated subjectively by grading the color and structure of the lenses in the shadowgraph images. On average the power and the surface contribution of the cataractous lenses was higher even though the difference was not statistically significant. This result confirms that the increase in power in older lenses may be due to the effect of cataract formation.

6.4.6. The non-human primate lens as a model for the human

The results of this study highlight the similarities in optical properties, biometric properties, growth and aging of the non-human primate lenses with those of the human. In both humans and non-human primates there is an age-dependent decrease in the equivalent refractive power of the maximally accommodated lens. The flattening of the lens surfaces in the maximally accommodated state contributes only a small portion to the age-dependent decrease in maximally accommodated lens power. In both the humans and the non-human primates the decrease in refractive contributions from the gradient refractive index is the major contributor to the rapid age-dependent decrease in maximally accommodated lens power and consequentially maximum accommodative amplitude. The results from this study indicate that the hamadryas baboon and the rhesus monkey lens are good models for the human lens. However, the cynomolgus monkey lens is significantly smaller than the human lens.

6.4.7. The refractive contributions of the refractive index gradient in the non-human primate lens

The equivalent refractive index values from the present study (maximum measured values of 1.436 for both cynomolgus monkey and baboon lenses and 1.430 for the rhesus monkey) are similar to those of the human lens *in vivo* (maximum of 1.4375) (Dubbelman and Van der Heijde 2001) and *in vitro* (maximum of 1.432) (Borja *et al.* 2008). The results from the present study are lower than previously reported *in vivo* rhesus monkey values (1.447 for a 5 year old rhesus monkey lens, Qiao-Grider *et al.* 2007). These differences can be attributed to differences in radii of curvatures values used for equivalent refractive index calculations. The significantly higher equivalent refractive index values reported by Qiao-Grider et al 2007 are due to larger spherical equivalent radii of curvature measurements which do not take into account surface asphericity.

6.4.8. Age dependent shape of the isolated non-human primate lens

We find an increase in diameter of the isolated non-human primate lens and a flattening of the lens surfaces over the entire age range of our study, and a decrease in the lens thickness in isolated lenses from young non-human primates. These trends are in good agreement with results obtained *in vivo*. Wendt *et al.* (2008) found that the maximally accommodated rhesus monkey lens diameter increases with age at a rate of 0.043mm/year, which is similar to those reported here for the human, hamadryas baboon and cynomolgus monkey isolated lenses. An age-dependent decrease in young human and non-human primate central lens thickness has been reported during *in vivo* measurements (Zadnik *et al.* 1993, Ip *et al.* 2007, Qiao-Grider *et al.* 2007, Augusteyn 2008). A general flattening of the lens surfaces with age has been well documented in the

monkey (Koretz *et al.* 1987, Qiao-Grider *et al. 2007*). Recently Rosales *et al.* (2008) measured the accommodation dependent lens radii of curvature for two 9 year old rhesus monkeys using Purkinje imaging. They found maximally accommodated radii of curvature (6.79mm for the anterior and -5.11mm for the posterior surfaces) that were within the range of our measurements indicating that the isolated lens is representative of the *in vivo* maximally accommodated lens in the non-human primate, as is the case in human lenses.

6.5. Age-dependent optical model of the isolated human and non-human primate lens

The age-dependencies of the isolated human lens thickness, diameter, surface curvatures, surface asphericities, surface power, effective refractive power and equivalent refractive index were compiled into an optical model (Table 6.6). The age-dependent isolated lens model was placed within a complete eye model and evaluated in an optical analysis software (OSLO LT). This model included the age-dependent anterior chamber depth, anterior and posterior corneal surfaces of the Dubbelman eye model (Norby 2005). The posterior chamber depth was adjusted to match an axial length of 24mm for ages over 15 years. For ages less than 15 years the posterior chamber depth was adjusted to match the total ocular axial length growth rate given by Mutti et al 1998.

This optical model was able to predict the age-dependent increase in the near point of focus (Figure 6.18). The normal age-related growth of the lens has a de-accommodating effect on the shape and power of the lens. These results suggest that, independent of the response of the lens to zonular tension, the changes induced by lens growth alone may significantly contribute to the loss of accommodation amplitude with age.

	Human	
	Lower Age Group*	Upper Age Group*
Central Thickness (mm)	4.96-0.04·Age (6-27 years)	3.62+0.02·Age (27-94 years)
Equatorial Diameter (mm)	7.91+0.04·Age (6-28 years)	8.89+0.01·Age (28-94 years)
Anterior Surface Radius of Curvature (mm)	4.46 + 0.14·Age (6 to 50 years)	13.83-0.05·Age (50 to 94 years)
Anterior Surface Asphericity	4.84-0.56·Age (6 to 26 years)	-14.7+0.25·Age (26 to 94 years)
Posterior Radius of Curvature (mm)	-3.47-0.06·Age (6 to 57 years)	-7.97 + 0.02·Age (57 to 94 years)
Posterior Surface Asphericity	-1.42+0.027·Age	
Equivalent Refractive Power (D)	41.59 – 0.41·Age (6 to 58 years)	-1.34 + 0.33·Age (58 to 82 years)
Surface Refractive Power (D)	14.09-0.13·Age (6 to 55 years)	9.84+0.02·Age (55 to 94 years)
Equivalent Refractive Index	$1.4320 - 3.90\times10^{-4}$·Age (6 to 60.4 years)	$1.4096 - 1.8\times10^{-5}$·Age (60.4 to 90 years)
Surface Refractive Contribution (%)	30.67+ 0.17· Age	

Table 6.6: Age-dependent optical model of the human isolated lens. All ages in years. *A bi-linear model is given for the optical and biometric parameters with non-linear age dependencies.

A.

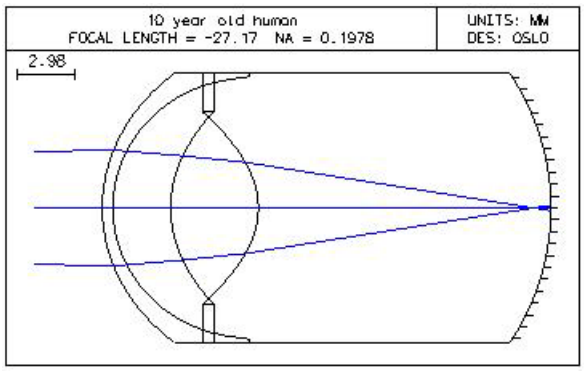

C.

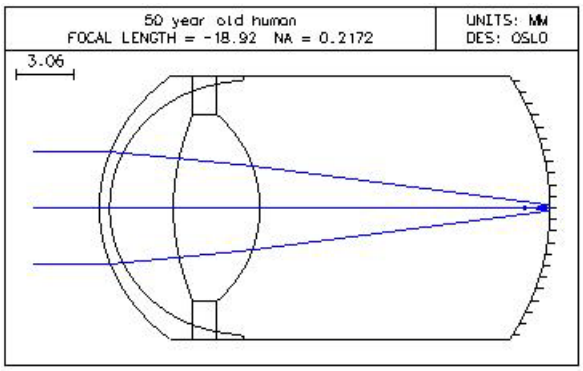

B.

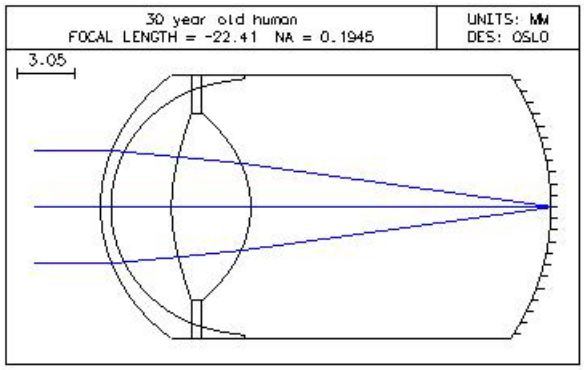

D.

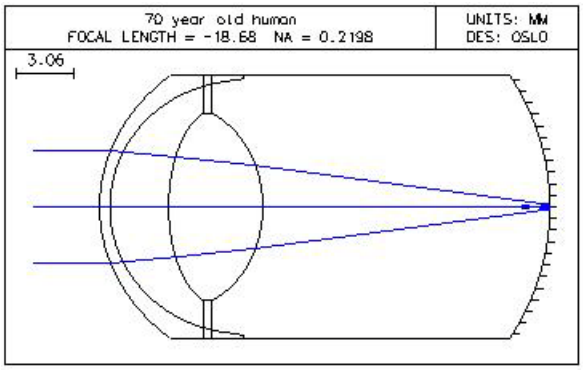

E.

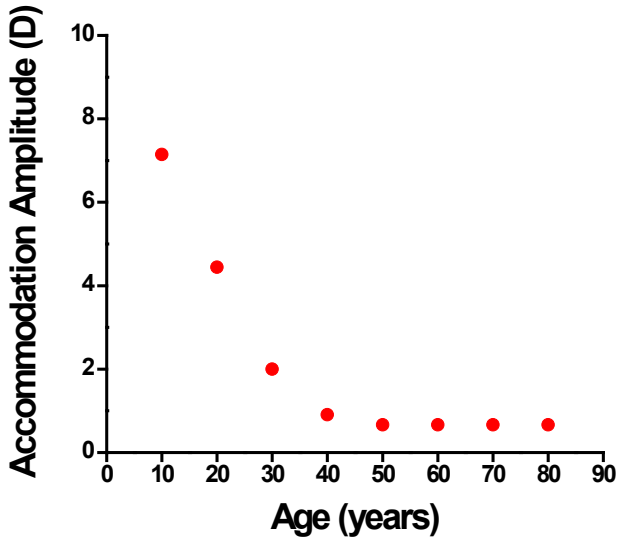

Figure 6.18: The human isolated lens model was evaluated at every decade from 10 to 80 years of age. The calculated lens model was entered into an optical analysis software (OSLO LT). The maximally accommodated human eye at 10 (A), 30 (B), 50 (C), and 70 (D) years of age. E. The accommodation amplitude predicted by the model as a function of age.

	Hamadryas baboon	
	Lower Age Group*	Upper Age Group*
Central Thickness (mm)	4.64-0.04·Age	
Equatorial Diameter (mm)	7.59+0.06·Age	
Anterior Surface Radius of Curvature (mm)	4.81±0.27 (1.7-14.7 years)	-2.54+0.51·Age (14.7 – 27.3 years)
Anterior Surface Asphericity	-0.89–0.25·Age	
Posterior Radius of Curvature (mm)	-3.03-0.09·Age	
Posterior Surface Asphericity	0.29-0.06·Age	
Equivalent Refractive Power (D)	52.45– 1.3·Age	
Surface Refractive Power (D)	21.56-0.37·Age	
Equivalent Refractive Index	$1.425–1.1x10^{-3}$·Age	
Surface Refractive Contribution (%)	38.40 + 0.62·Age	

Table 6.7: Age-dependent optical model of the hamadryas baboon isolated lens. All ages in years. *A bi-linear model is given for the optical and biometric parameters with non-linear age dependencies.

	Cynomolgus monkey	Rhesus monkey
Central Thickness (mm)	4.33-0.05·Age	4.93-0.078·Age
Equatorial Diameter (mm)	6.92+0.07·Age	$\frac{8.82}{1+e^{-0.3(Age+4.7)}}$
Anterior Surface Radius of Curvature (mm)	3.66+0.06·Age	4.68±1.10
Anterior Surface Asphericity	-1.62 ± 1.96	-0.98 ± 1.38
Posterior Radius of Curvature (mm)	-2.80–0.09·Age	-3.27-0.08·Age
Posterior Surface Asphericity	-0.11 ± 0.89	0.52 - 0.23·Age
Equivalent Refractive Power (D)	53.18 - 1.2·Age	54.22- 1.8·Age
Surface Refractive Power (D)	26.28-0.46·Age	22.86-0.74·Age
Equivalent Refractive Index	1.4252±0.010	1.423 ± 0.005
Surface Refractive Contribution (%)	45.29 ± 5.85	41.89 ± 2.50

Table 6.8: Age-dependent optical model of the human isolated lens. All ages in years.

6.6. Implications for Phaco Ersatz

Phaco-Ersatz aims to restore accommodation by replacing the hardened lens contents with a soft polymer which can be deformed during accommodation. Ideally the goal of Phaco-Ersatz procedure is to restore the normal accommodative function of a

young adult eye. If we use the optical properties of a 20 year old human lens as a reference, the results of this study suggest that the target properties for artificially refilled lens should be:

- Power = 33.4 D
- Refractive Index = 1.424
- Volume = 177 mm^3
- Anterior Radius = 7.3 mm
- Posterior Radius = 4.7 mm

If the mechanical properties of the implant match those of the young natural lens then the application of zonular forces is expected to create the same change in shape as in the natural lens. The flattening of the surfaces will cause a decrease in the power of the implant. The amplitude of accommodation of the implant will then depend on whether or not the gradient contributes to the accommodative amplitude in the natural lens. The role of the gradient to the accommodation amplitude of the natural lens is quantified in the next chapter.

6.7 Summary

In this chapter we presented results of the isolated human and non-human primate lens shape and refractive power measurements. These results were used to develop an age-dependent optical model of the isolated lens. The data was used to develop initial optical design criteria for the Phaco-Ersatz lens refilling implant. To the best of our knowledge, the data presented in this chapter is the most complete dataset of optical and biometric properties of the primate crystalline lens in terms of age range, species and number of samples. The main findings of this part of the study are:

- the isolated lens shape and power values obtained in this study correspond well to those of the in vivo maximally accommodated lens
- the growth of the lens has a dis-accommodating effect on the shape and power of the isolated lens
- the changes in lens shape and surface refractive power have a minor contribution to the age dependent decrease in isolated lens power
- the age-dependent decrease in isolated lens refractive power can be attributed to the decrease in the refractive contributions from the gradient
- the decrease in refractive contributions from the gradient corresponds to the decrease in accommodative amplitude with age
- and that the human and the non-human primate lenses have similar age dependencies.

All of these findings are in agreement with the basic principle of the Helmholtz theory of accommodation. They suggest that the age-dependent changes in lens shape and the changes in the refractive index distribution inside the lens could have a significant contribution to presbyopia.

CHAPTER 7. DYNAMIC OPTICAL MODEL OF THE LENS DURING SIMULATED ACCOMMODATION

7.1. Objective

The goal of this dissertation is to better understand the relationship between the crystalline lens shape, its non-uniform refractive index gradient and its optical power and their changes with age and accommodation. In the previous section we developed an age-dependent optical model of the isolated lens (which is free of external forces). The objective of this section is to develop an accommodation-dependent model. The model will be used to determine the contribution of the gradient refractive index to the accommodative amplitude of the natural lens.

7.2. Methods

7.2.1. General Description

Biometric and optical power measurements of ex-vivo in situ lenses were performed during simulated accommodation in the second generation lens stretching system (Erhmann et al 2008) (EVAS II) (Section 4.2). Biometric properties of the lens during stretching were measured from cross sectional optical coherence tomography images and Scheimpflug slit-lamp images (Section 4.3). The refractive power of the lens at different levels of accommodation was measured with an optical system based on the Scheiner principle (Section 4.2). Finally the acquired optical and biometric data was used to calculate the refractive contributions of the refractive index gradient (the equivalent refractive index) at each incremental step of stretching.

During the stretching experiments the actuators were programmed to travel a total of 2mm in 0.5mm steps at a speed of 0.25mm/second. This corresponds to a total

displacement of 4mm applied to the outer sclera. The actuators are stopped for 10 seconds at each step to allow for measurements of lens power and acquisition of the Scheimpflug cross sectional images. The actuators are stopped for 60 seconds during the OCT image acquisition. The load was continuously recorded during the stretching experiments

7.2.2. Donor tissue

7.2.2.1. Human tissue

All human tissue was obtained and used in compliance with the guidelines of the Declaration of Helsinki for research involving the use of human tissue. Experiments were performed on a total of 13 eyes from 12 phakic donors. The donor globes arrived in sealed, Styrofoam containers filled with ice and used between 1 and 5 days post-mortem (average: 2.3±0.7 days). The donor ages ranged from 31 to 90 years.

7.2.2.2. Non-human primate tissue

All animal experiments adhered to the ARVO Statement for the use of animals in research. No animal tissue was used for the sole purpose of this study. Hamadryas baboon and rhesus monkey tissue was donated by the Division of Veterinary Resources at the University of Miami as part of a tissue sharing protocol. Measurements were performed on 9 isolated hamadryas baboon (*Papio hamadryas*) lenses from 8 donors within 24 hours of euthanasia (PMT = 7.1 ± 9.4 hours, ages = 3 to 21 years).

7.2.3. Tissue preparation

Tissue dissection was performed by an ophthalmic surgeon under an operation microscope (Figure 7.1). The tissue preparation followed the same protocol as described in a previous study (Parel, 2002, Manns et al, 2007). In this technique a band of 8 independent scleral shoes were bonded with cyanoacrylate adhesive (Duro SuperGlue, Henkel Locktite Corp, Cleveland, OH) onto the anterior sclera surface from the limbus to the equator. The band of scleral shoes prevents deformation of the globe during dissection and provides attachment points for the lens stretcher device. The posterior pole was then sectioned and the cornea and iris were removed. Scleral incisions were made between adjacent shoes to produce 8 segments for stretching. The dissected tissue was then transferred to the testing chamber, which was filled with the DMEM preservation medium.

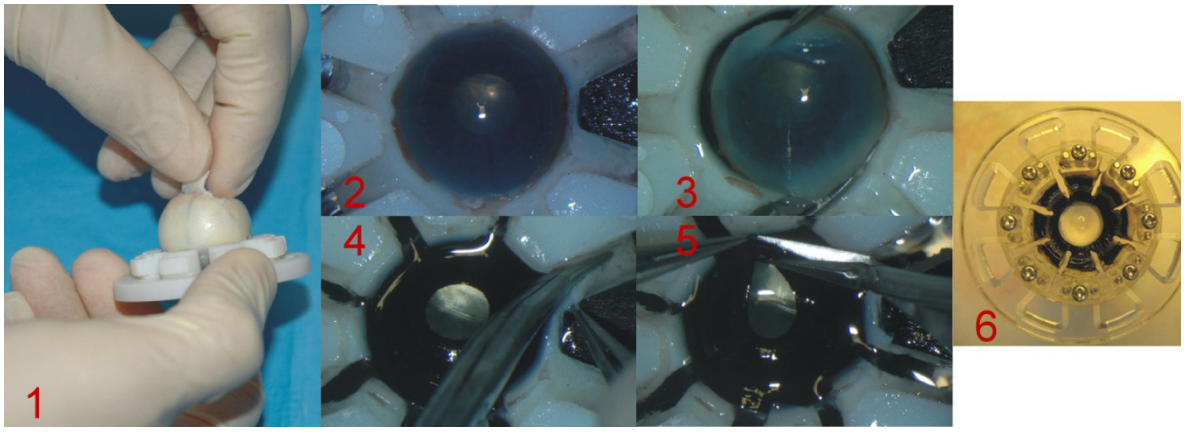

Figure 7.1: EVAS II - Surgical Tissue Preparation - The intact globe (1) is bonded to eight independent scleral shoes. The posterior hemisphere and cornea are removed (2 and 3). Full thickness incisions are made into the sclera to separate adjacent shoes (4). The iris is removed (5). The prepared tissue sample is ready to be mounted in the stretcher system (6).

7.2.4. Data and statistical analysis

To prevent values obtained from paired eyes biasing the statistics for age dependence, the values from left and right eyes of each donor were averaged. The average values were then used as a single point for age dependence calculations. A p-value of 0.05 was set as the condition for statistical significance.

The age and accommodation dependent model was developed using the following steps. First, the parameters (lens diameter, thickness, surface curvatures, equivalent refractive index, surface refractive power, and surface refractive contribution) of the lens free of zonular (maximally accommodated) were used as a starting point for the model. According to Chapter 6 these parameters correspond to the parameters of the isolated lens. The results of the stretching experiments described in the following sections were then used to express the variation of each parameter *X*, as a function of the change in power of the lens, ΔP:

$$X(\Delta P) = X_{isolated} + f(\Delta P) \qquad \text{Eq. 7.1}$$

where *f* is the function that gives the power dependence. In most cases the variations with power can be modeled with a linear function:

$$X(\Delta P) = X_{isolated} + \Delta P \cdot Slope \qquad \text{Eq. 7.2}$$

where *Slope* is the slope of the linear regression of the parameter (X) as a function of the power change (ΔP). Both the isolated lens parameters and the slope of the regression vary with age:

$$X_{isolated}(age) = X_0 + b \cdot age \qquad \text{Eq. 7.3}$$

$$Slope(age) = Slope_0 + c \cdot age \qquad \text{Eq. 7.4}$$

where X_0 and b are the parameters of the age-dependent model of Chapter 6 and $Slope_0$ and c were derived from the analysis of the age-dependence of the lens stretching results. Combining Equations 7.2, 7.3 and 7.4 gives the following expression for the age and accommodation dependence of each parameter:

$$X(\Delta P, age) = X_0 + b \cdot age + \Delta P \cdot (Slope_0 + c \cdot age) \qquad \text{Eq. 7.5}$$

As a final step a maximum value of the power change ΔP max was derived for each age from the results of the stretching experiments.

7.3. Results

7.3.1 General trends

In general the results of this study are consistent with the Helmholtz theory of accommodation. Ex vivo simulated accommodation by radially stretching the young pre-presbyopic crystalline lens produces:

-an increase of the lens equatorial diameter

-a decrease of the central lens thickness

-a flattening (increase of the) anterior and posterior surface radii of curvature

-a negative shift in anterior and posterior surface asphericities (a hyperbolic shift)

-a decrease in equivalent refractive power

- a decrease in surface refractive power

- no significant changes to the surface refractive contributions

- and no significant changes in the refractive contributions of the gradient refractive index.

Sample images of a 2 and a 21 year old baboon lens are given in Figure 7.2 and 7.3 respectively. The typical stretching response curves of the young and the old baboon

lenses are given in Figure 7.4 as a function of induced load and in Figure 7.5 as a function of the induced power change during simulated accommodation. Sample images a 31 and a 60 year old human lens are given in Figures 7.6 and 7.7 respectively. The typical stretching response curves of the two human lenses are given in Figure 7.8 as a function of load. The stretching induced changes in human lens properties are presented in Section 7.3.2. The age dependent maximum stretching changes in baboon lens properties are presented in Section 7.3.4. The stretching changes in the baboon lens properties as a function of induced load are presented in Section 7.3.5. The stretching changes in the baboon lens properties as a function of induced power change are presented in Section 7.3.6.

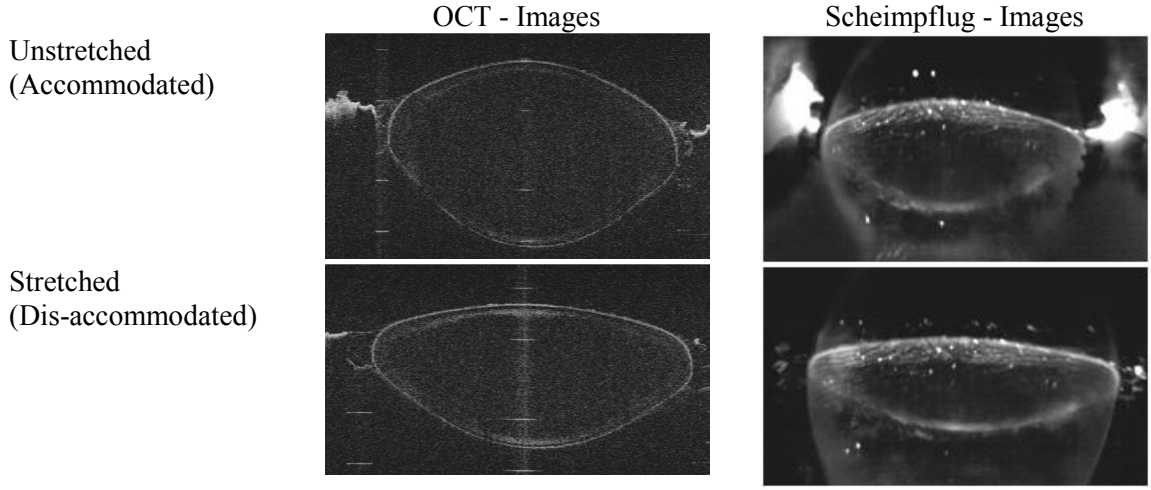

Figure 7.2: Cross sectional images of a 2 year old hamadryas baboon (within 2 hours postmortem) during simulated accommodation. The lenses were stretched from 0 to 2mm and crossectional images were obtained at every 0.5mm of stretch with an (Left) OCT system and a (Right) Scheimpflug slit-lamp microscope system.

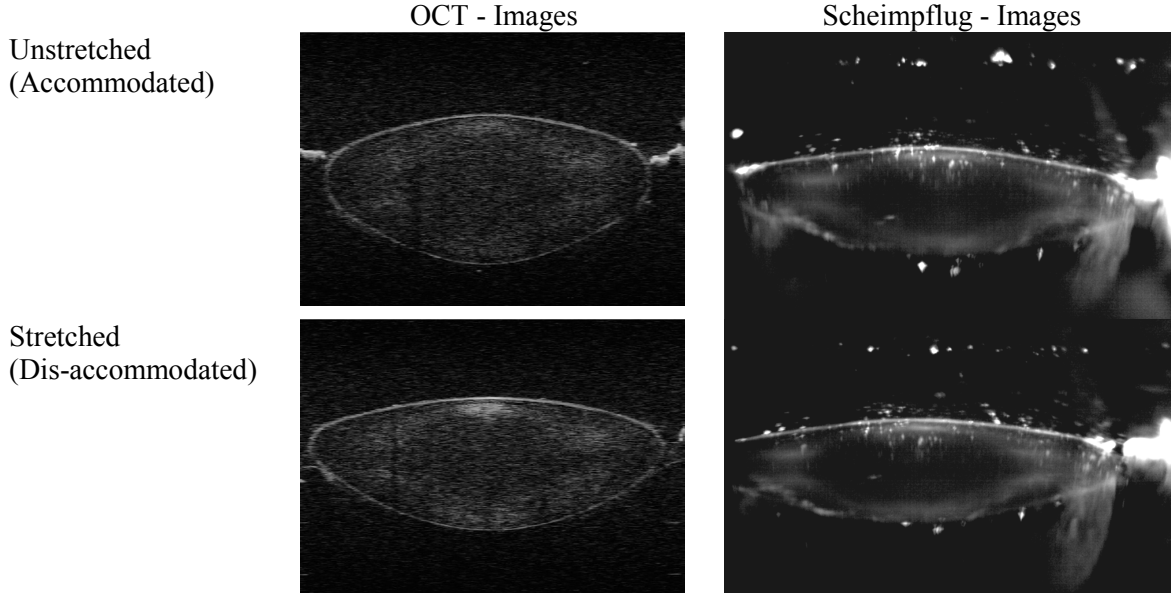

Figure 7.3: Cross sectional images of a 21 year old hamadryas baboon (within 2 hours postmortem) during simulated accommodation. The lenses were stretched from 0 to 2mm and crossectional images were obtained at every 0.5mm of stretch with an (Left) OCT system and a (Right) Scheimpflug slit-lamp microscope system.

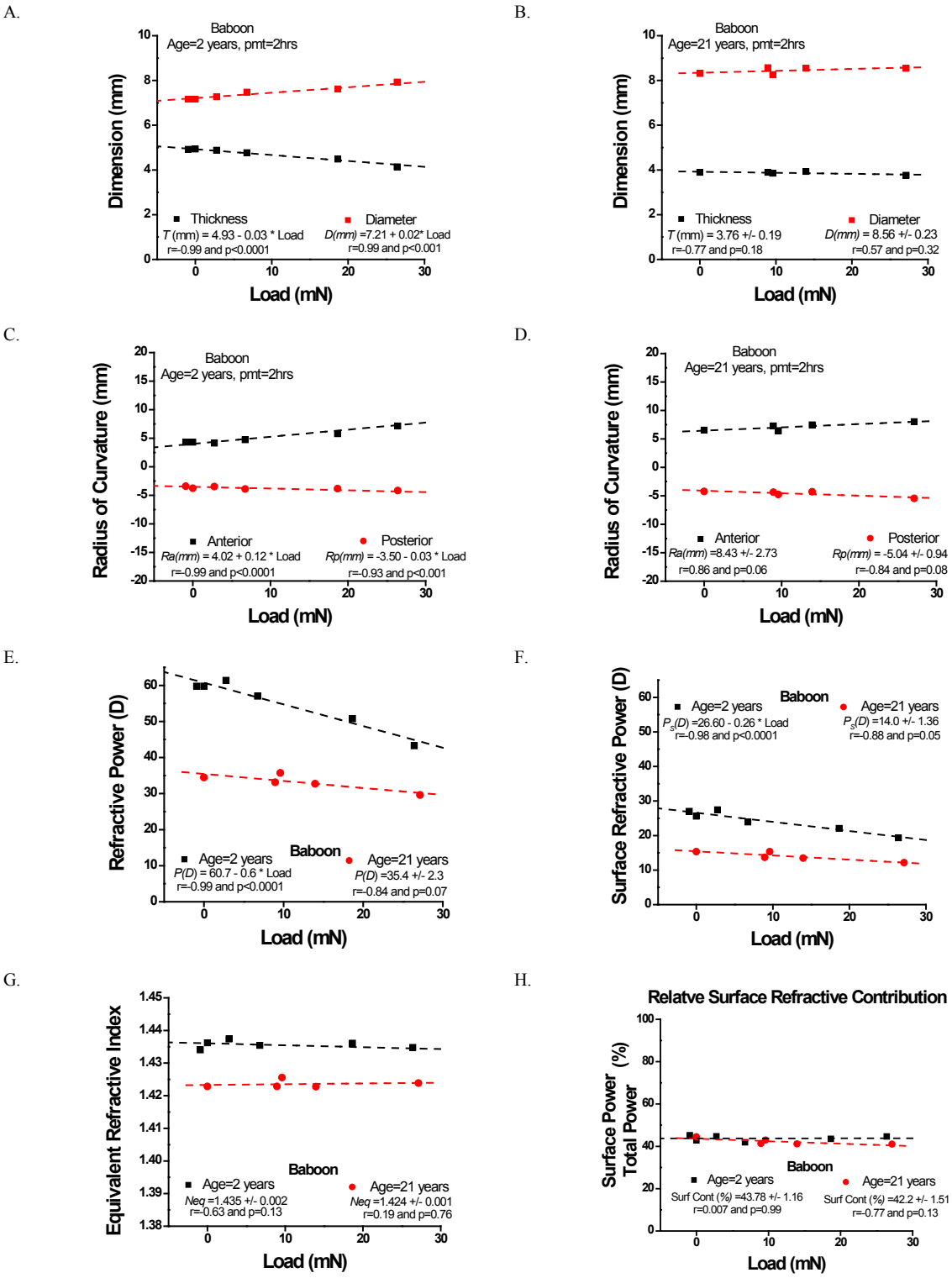

Figure 7.4: Typical load response of a 2 and a 21 year old hamadryas baboon lens (postmortem time =2 hours). The changes in lens diameter and thickness (A and B) radius of curvature (C and D) and power (E and F) as a function of the load induced during stretching. No load dependence was observed in the equivalent refractive index (G) or the relative surface refractive contributions (H).

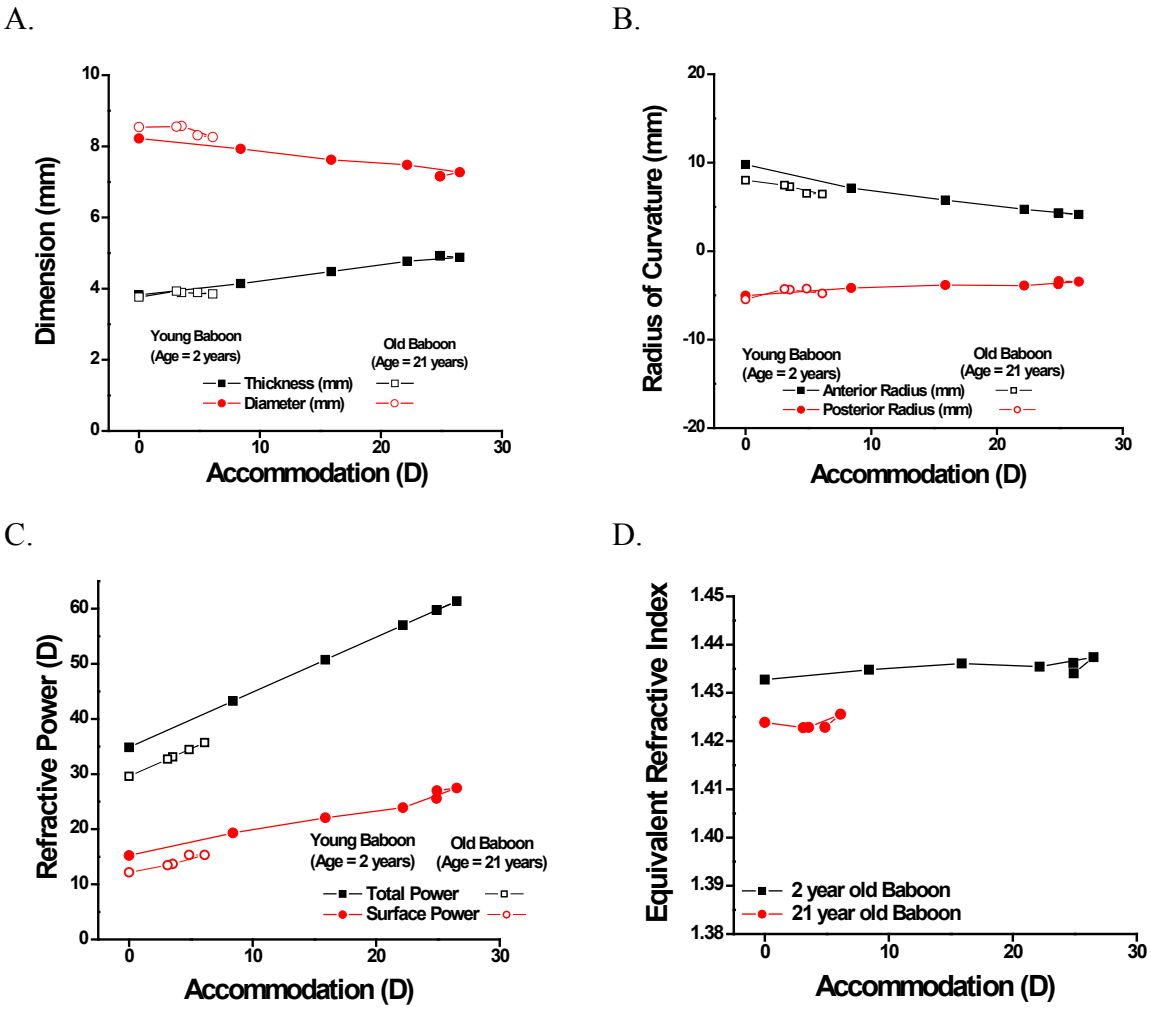

Figure 7.5: Typical stretching response of a 2 year old and a 21 year old hamadryas baboon (postmortem time =2 hours). In this figure the x-axis is labeled "Accommodation". Throughout this chapter this term refers to the change in power at each step with respect to the maximum stretched refractive power. The changes in lens thickness, diameter (A.) and radii of curvature (B.) as a function of the power change induced during stretching. (C.) The back vertex power and surface power of the lens as a function of the power change during stretching. (D.) The equivalent refractive index remained constant during power change.

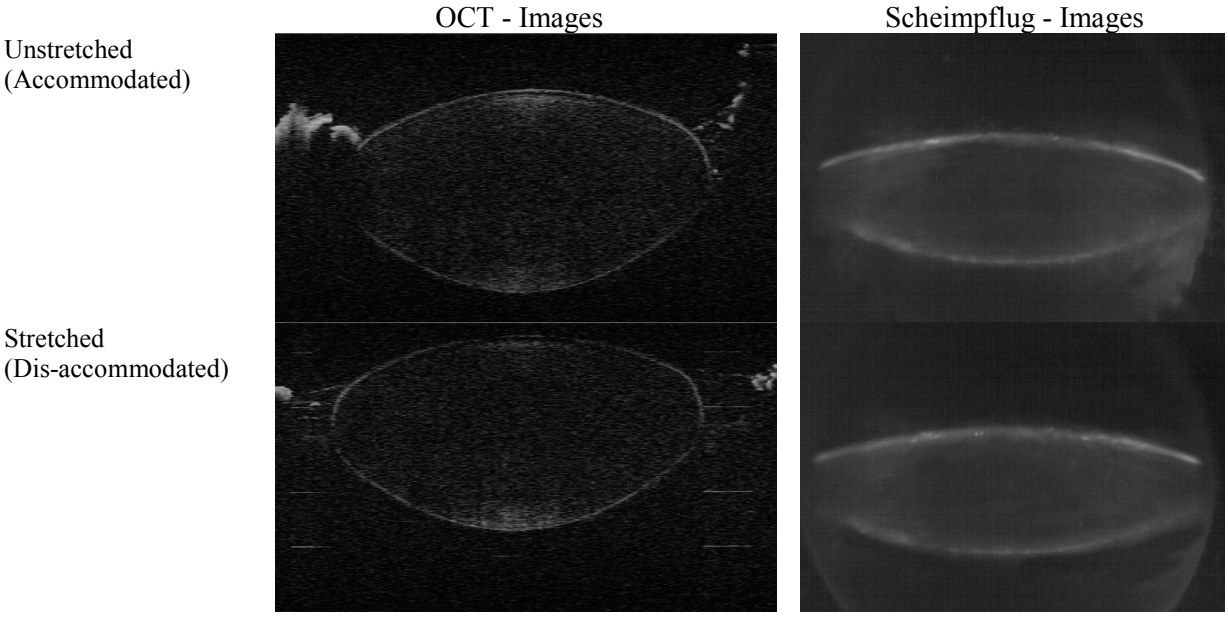

Figure 7.6: Cross sectional images of a 34 year old human lens (within 88 hours postmortem) during simulated accommodation. The lenses were stretched from 0 to 2mm and cross sectional images were obtained at every 0.5mm of stretch with an (Left) OCT system and a (Right) Scheimpflug slit-lamp microscope system.

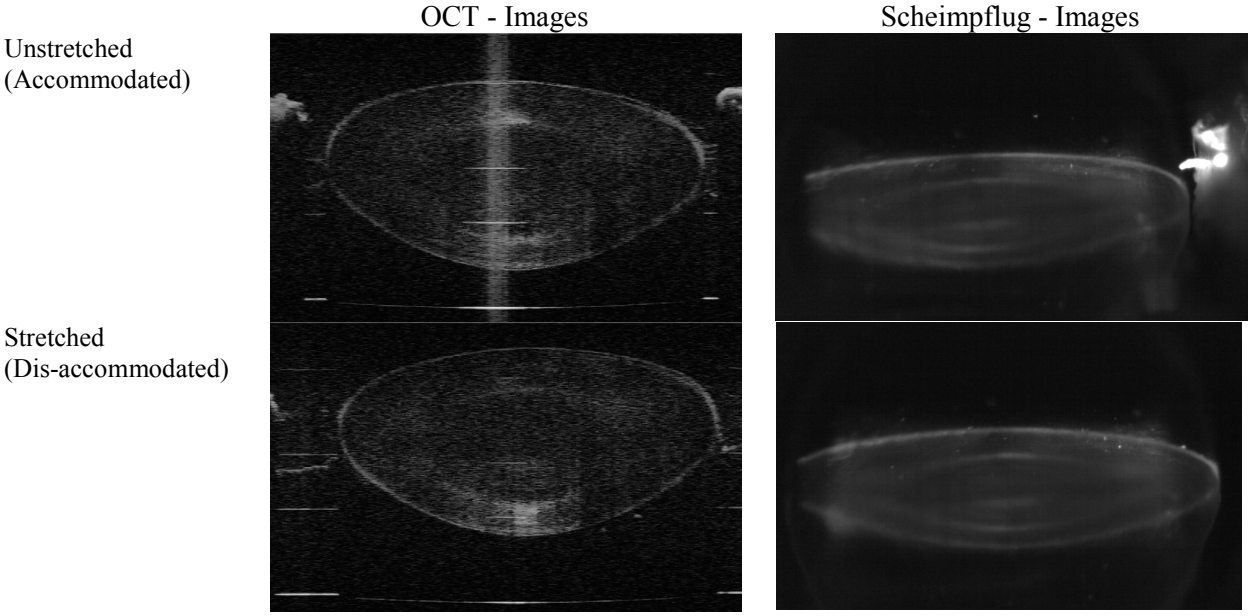

Figure 7.7: Cross sectional images of a 57 year old human lens (within 77 hours postmortem) during simulated accommodation. The lenses were stretched from 0 to 2mm and cross sectional images were obtained at every 0.5mm of stretch with an (Left) OCT system and a (Right) Scheimpflug slit-lamp microscope system.

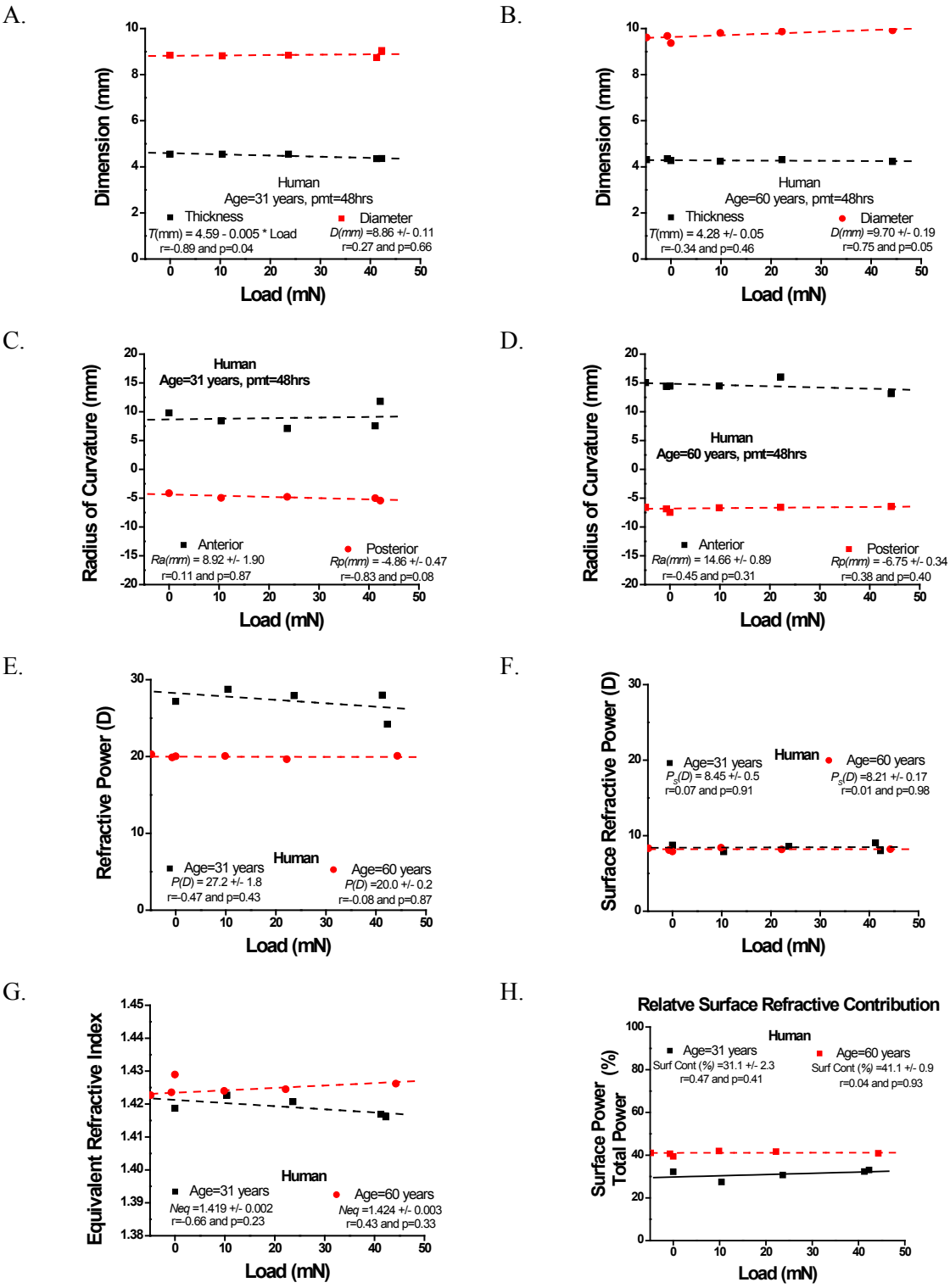

Figure 7.8: Typical load response of a 31 and a 60 year old human lens (postmortem time =2 days). The changes in lens diameter and thickness (A and B) radius of curvature (C and D) and power (E and F) as a function of the load induced during stretching. The load response of the lens equivalent refractive index (G) and the relative surface refractive contributions (H).

7.3.2 Stretching response of the human lens

The maximum change in the human lens shape and power induced during simulated accommodation were plotted as a function of age. Lenses obtained from donors within the presbyopic age range showed no significant changes in lens shape and power during stretching. Two pair of human lenses obtained from donors in the age range near the onset of presbyopia showed slight changes in lens shape and power during stretching. There was insufficient human data to determine the age dependencies of the changes in the lens induced during stretch.

A.

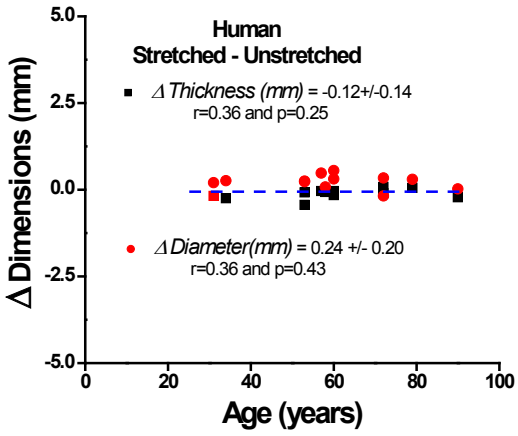

B.

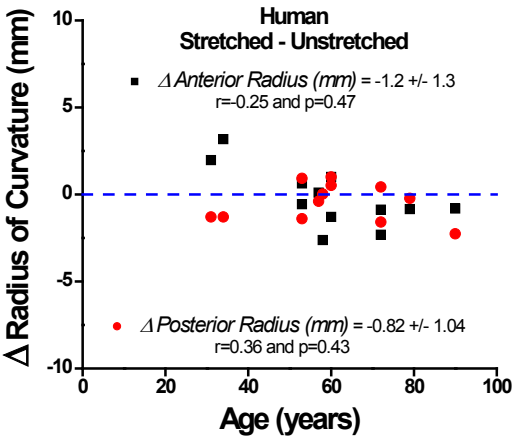

C.

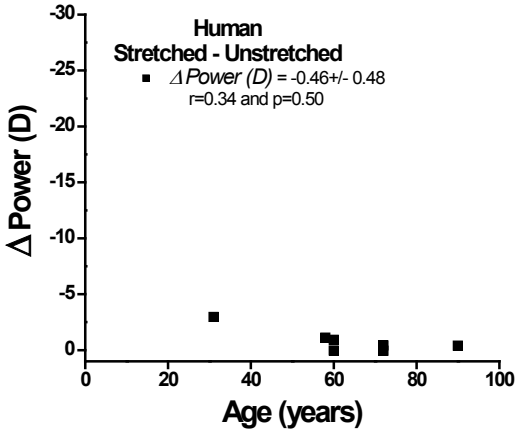

Figure 7.9: Maximum stretching induced changes in human lens shape and power. Two pre-presbyopic human lenses showed significant changes in lens shape and power during stretching.

7.3.3 The age dependent changes between the unstretched and stretched baboon lens

The values of the unstretched and maximum stretched lens biometric parameters (thickness, diameter and surface curvatures) and optical parameters (equivalent refractive index, refractive power and surface refractive power) for each baboon lens were plotted as a function of age (Figure 7.10). A linear regression was performed to determine the age dependence in the lens shape and power parameters at the two states. A similar analysis was performed on the maximum change (stretched – unstretched) in lens parameters during simulated accommodation (Figure 7.11).

The age dependencies for the unstretched baboon lens biometric and optical properties closely match those of the isolated baboon lens (Chapter 6). Most of the biometric and optical properties of the maximally stretched lens had no age dependence over the sampled age range (Figure 7.10 and Table 7.1). As a result the maximum change in lens shape and power during simulated accommodation decrease with age (Figure 7.11 and Table 7.2). The stretching induced changes in lens shape and power approach zero in the hamadryas baboon during third decade of life. The age dependent linear regression equations for the unstretched and stretched lens parameters are given in Table 7.1. The linear regressions for the age dependent decrease in maximum change in lens parameters are given in Table 7.2.

During stretching there was no change in the refractive contribution of the surfaces. There was no change in equivalent refractive index during simulated accommodation. The age-dependent rate of decrease in the equivalent refractive index of both the stretched and unstretched lens closely matched the rate of decrease of the isolated baboon lens (-1.1×10^{-3}/year).

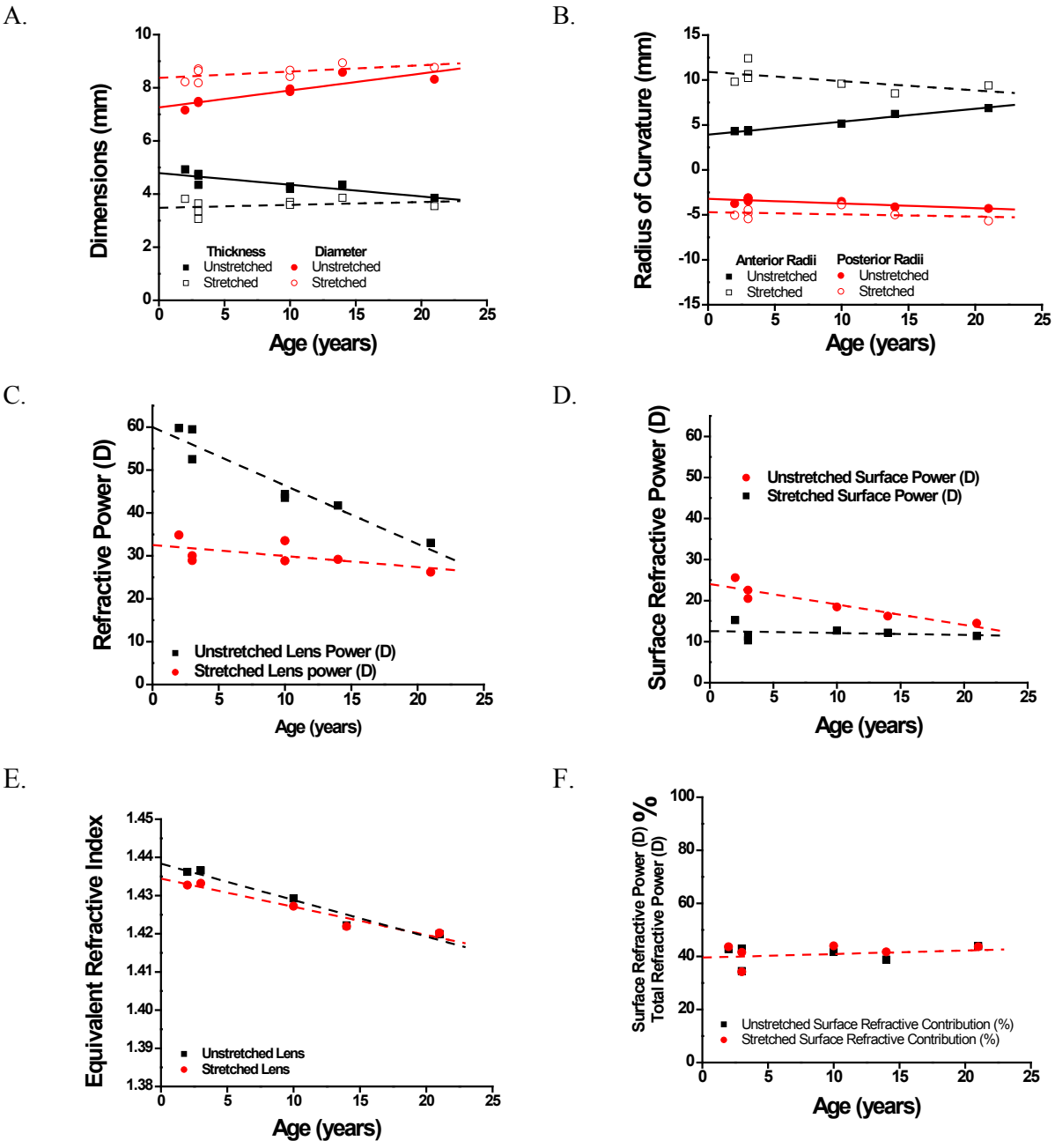

Figure 7.10: A comparison of the unstretched and stretched baboon lens thickness, diameter (A.) and surface curvatures (B.) as well as total refractive power (C.) and surface refractive power (D.) as a function of age. Equivalent refractive index did not significantly change with stretching (E.). Over the sampled age range there were no significant age dependent changes in the stretched lens shape or power. As the lens ages the shape and power of the unstretched lens converges to that of the stretched lens. The age dependent linear regression equations for the unstretched and stretched lens parameters are given in Table 7.1

	Unstretched lens	Stretched
Thickness (mm)	4.79-0.036·Age r=-0.85, p=0.007	3.57±0.26
Diameter (mm)	7.26+0.06·Age r=0.90, p=0.002	8.57±0.27
Anterior Radius (mm)	3.92+0.14·Age r=0.99, p<0.001	10.07±1.22
Anterior Surface Asphericity	0.81-0.45·Age r=-0.83, p=0.021	-4.59±3.9
Posterior Radius (mm)	-3.22-0.05·Age r=-0.83, p=0.02	-4.90±0.60
Posterior Surface Asphericity	0.83-0.10·Age r=-0.91, p=0.003	-0.005±1.37
Back Vertex Power (D)	60.0-1.4·Age r=-0.96, p<0.001	30.2±3.0
Surface Refractive Power (D)	24.1 - 0.37·Age r=-0.92, p=0.008	12.15±1.7
Surface Refractive Contribution (%)	41.5 ± 3.3 r=0.29, p=0.58	41.0 ± 3.5 r=0.41, p=0.42
Equivalent Refractive Index	$1.438-9.5\times10^{-4}\cdot$Age r=-0.97, p=0.004	$1.434-7.37\times10^{-4}\cdot$Age r=-0.97, p=0.005

Table 7.1: Age dependent trends of the unstretched (accommodated) and maximally stretched (dis-accommodated) baboon lens during simulated accommodation. All ages are in years. The mean values are given for the parameters which did not have statistically significant age dependence.

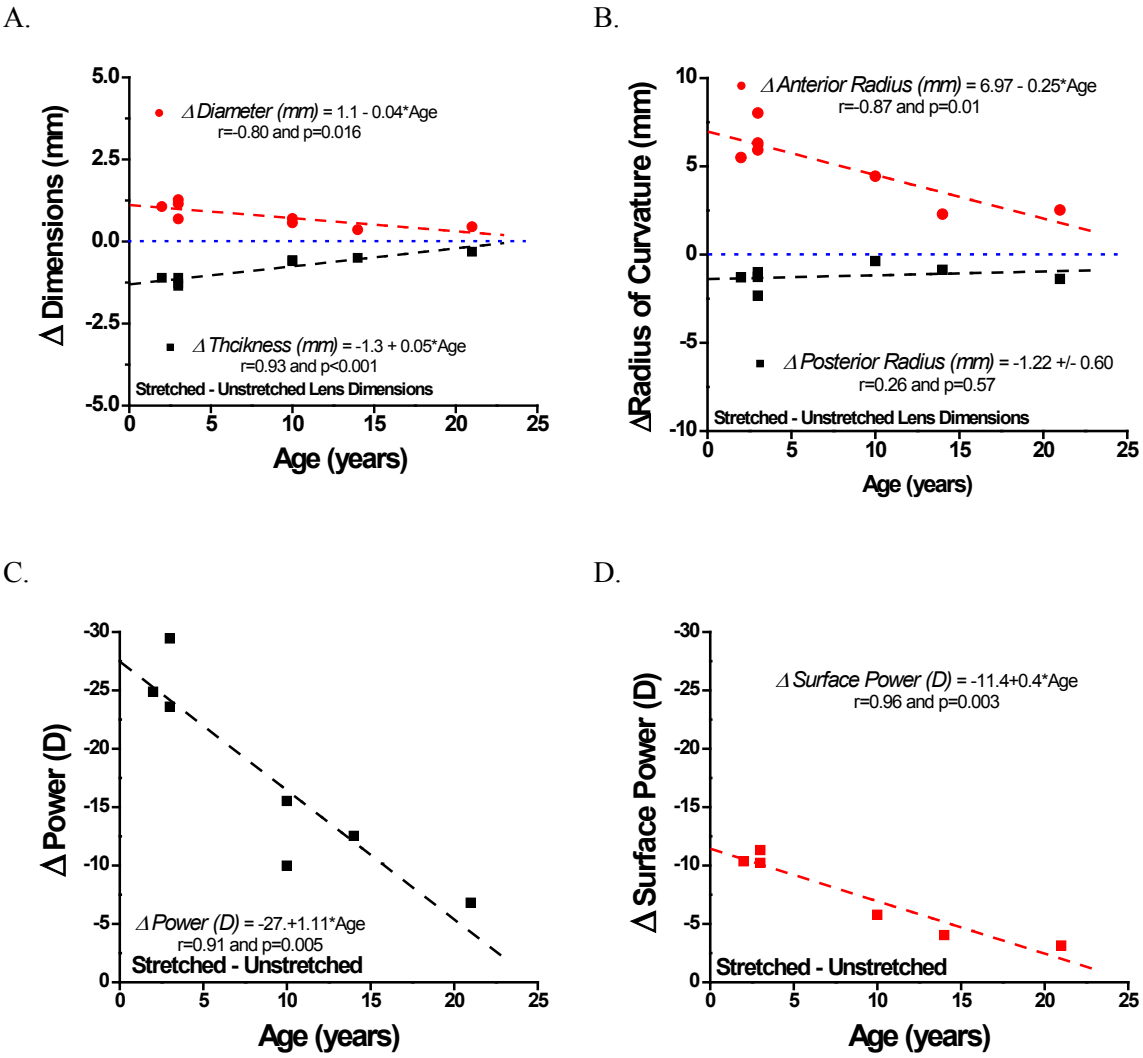

Figure 7.11: Changes in hamadryas baboon lens thickness, diameter (A), radii of curvatures (B) back vertex power (C) and surface refractive power (D) induced during simulated accommodation as a function of age. The changes induced during stretching decrease with age and approach zero in the third decade of life in the hamadryas baboon.

Maximum stretching induced changes as a function of age	
Thickness (mm)	-1.31 + 0.05 · Age
Diameter (mm)	1.11 - 0.04 · Age
Anterior Radius (mm)	6.97 - 0.25 · Age
Anterior Asphericity	-5.14 ± 3.98
Posterior Radius (mm)	-1.22 ± 0.60
Posterior Asphericity	0.51 ± 1.69
Surface refractive power (D)	-11.1 + 0.4 · Age
Change in lens power (ΔD)	-27.5 + 1.1 · Age

Table 7.2: Age dependent linear regression of the maximum changes in lens shape and power induced during stretching. As the lens ages the changes induced during stretching decrease and approach zero in the baboon during third decade of life. The mean and standard deviations are given for the properties which showed no age dependence.

7.3.4. The age dependent load response of the lens during simulated accommodation

Typical load responses of a 2 and a 21 year old baboon lens during simulated accommodation are given in Figure 7.4. Typically load increases as the lens is stretched from 0 to 2mm. The induced load is partially transferred to the sclera, cilliary body, zonular fibers and the remainder to the lens capsule and the lens contents itself. This increasing load on the lens causes an increase lens diameter, a decrease in lens thickness, a flattening of the lens surfaces, and a decrease in refractive power.

A linear response was observed for the baboon lens shape and power as a function of the induced load during stretching (Figure 7.4). The slopes of the lens shape and power load responses were plotted as a function of age. A linear regression was performed to determine any age dependence for the lens stretching load response (Figure 7.12).

The baboon lens power-load response and shape-load response decrease with age. However, these age-dependent changes are not statistically significant. The average baboon lens load response is presented in Table 7.3.

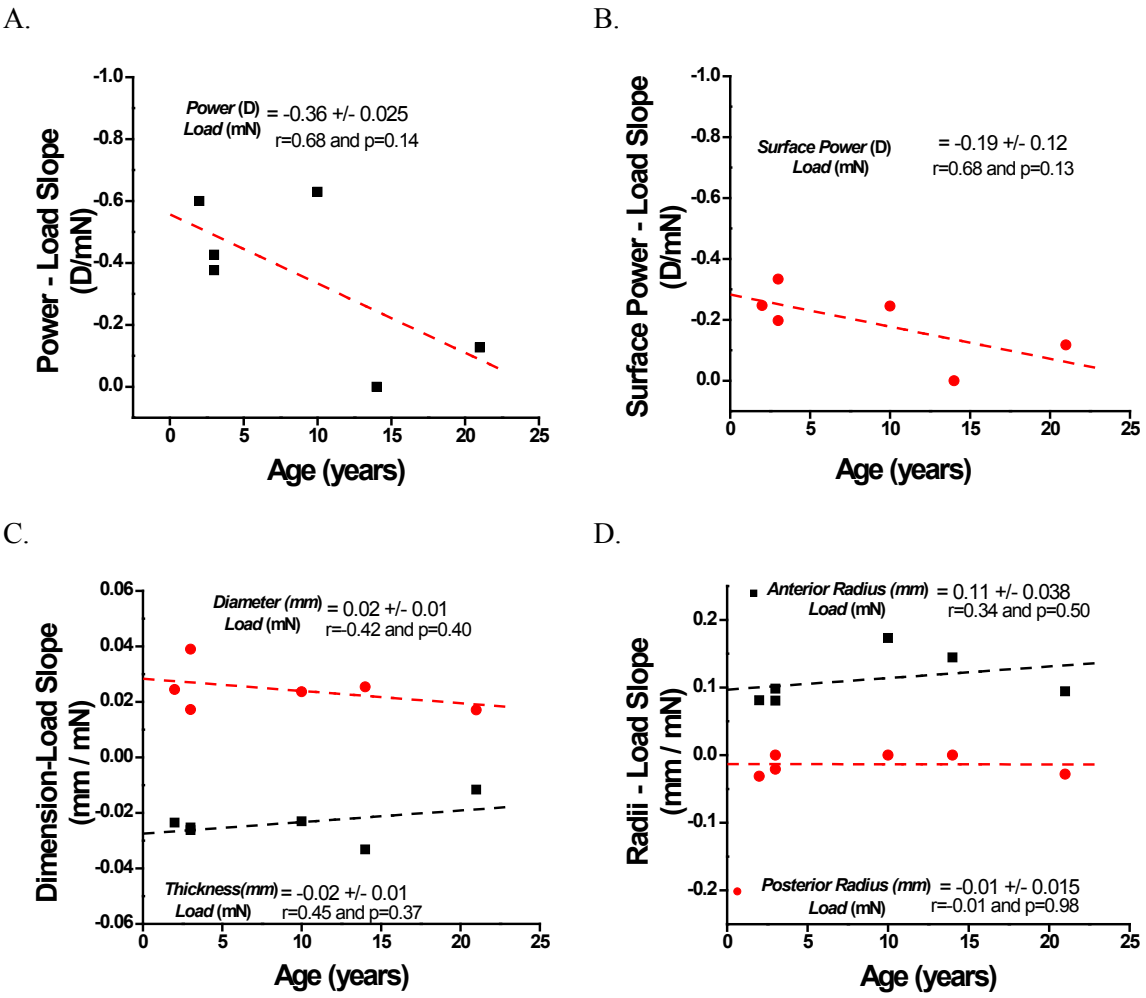

Figure 7.12: The age-dependent changes in lens shape and power as a function of induced load. The lens power-load slope (A) and surface power-load slope (B) decrease with age. Similarly the thickness-load slope, diameter-load slope (C) and surface curvature-load slopes (D) decrease with age. The age-dependent changes in the lens-load responses were not statistically significant.

	Load response of the baboon lens
Thickness (mm)	-0.02 (±0.01) [mm/mN]
Diameter (mm)	+0.02 (±0.01) [mm/mN]
Anterior Radius (mm)	+0.10 (±0.06) [mm/mN]
Anterior Surface Asphericity	-0.01 (±0.23) [/mN]
Posterior Radius (mm)	-0.01 (±0.02) [mm/mN]
Posterior Surface Asphericity	+0.01 (±0.02) [/mN]
Back Vertex Power (D)	-0.27 (±0.30) [D/mN]
Surface Refractive Power (D)	-0.13 (±0.11) [D/mN]
Equivalent Refractive Index	No change

Table 7.3: The changes in baboon lens shape and power as a function of applied load during simulated accommodation. The load response of the baboon lens showed an age-dependent decrease. However these changes were not statistically significant.

7.3.5. The age dependent power response during simulated accommodation

The typical stretching response as a function of induced power change for a 2 and 21 year old baboon lens are given in Figure 7.5. During stretching there is a linear relationship between the induced power change and the lens thickness, diameter, surface curvatures and the surface refractive power. Slopes of these lens parameters as function of the induced power changes were plotted as a function of donor age. A linear regression was performed to determine the age dependence of the power slopes (Figure 7.13).

The age dependent power slopes for the baboon lens are presented in Table 7.4. There was no age dependent change in the diameter-power slope, thickness-power slope or the posterior surface curvature-power slope. There was a significant age-dependent negative shift in the anterior surface curvature-power slope. The change in surface refractive power as a function of total refractive power change is constant with age (Figure 7.13.c).

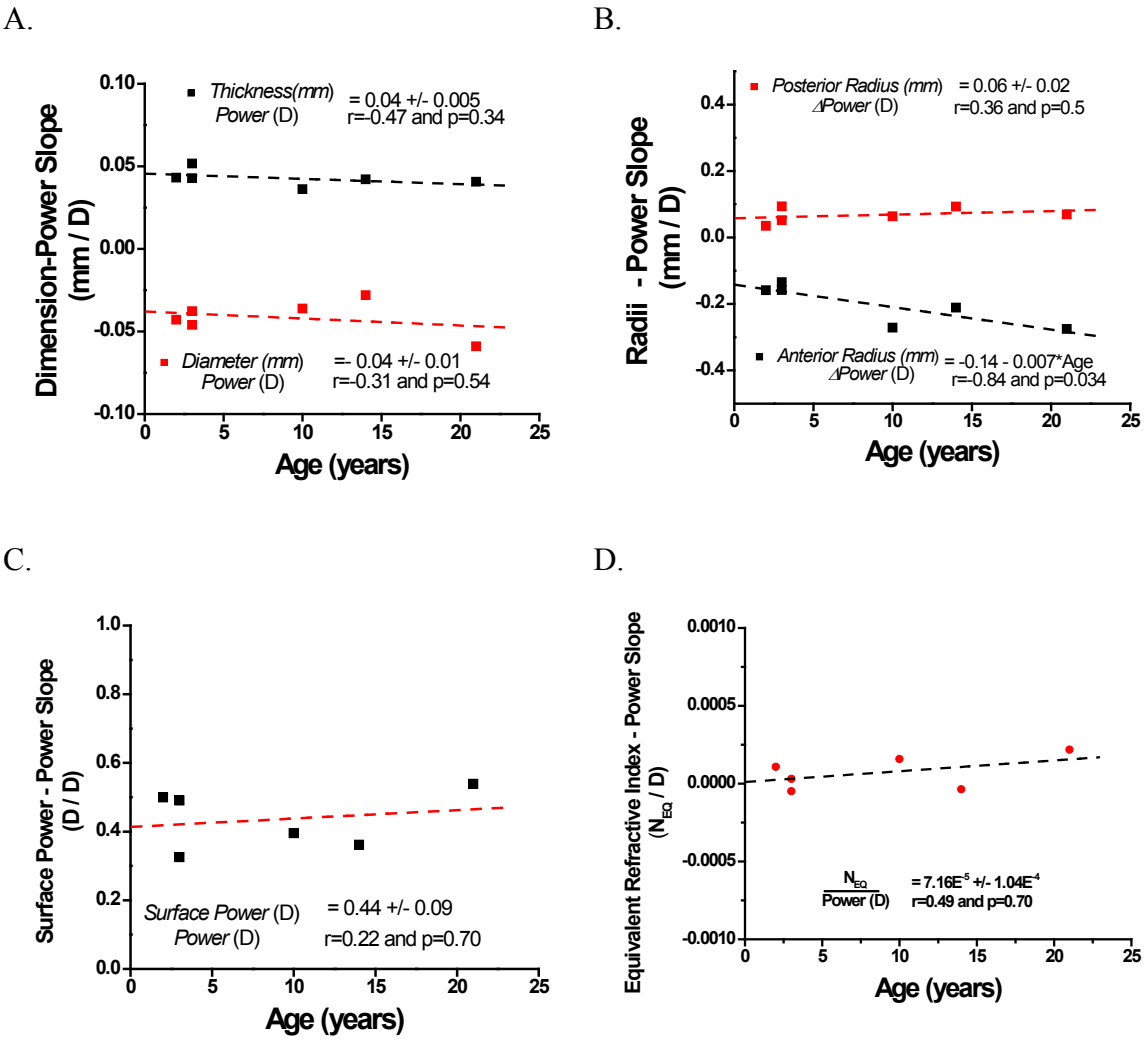

Figure 7.13: The age-dependent simulated accommodation power response of the baboon lens. (A) The lens diameter-power slope and the thickness-power slope had no age dependence. (B) The posterior curvature-power slope did not change with age. The anterior surface curvature-power slope increased with age. Indicating an increase in anterior surface curvature change is needed to produce the total power change in older lenses. (C) The surface refractive power-power slope was constant with age, indicating that the surfaces contribute a constant amount of power change independent of age. (D.) The NEQ-Power slope was near zero and constant with age indicating that the refractive contributions of the gradient do not change during simulated accommodation.

Power response of the baboon lens	
Thickness–Power Slope [mm/D]	-0.04 ± 0.01
Diameter –Power Slope [mm/D]	0.04 ± 0.01
Anterior Radius–Power Slope [mm/D]	-0.14 -0.01·Age
Anterior Surface Asphericity –Power Slope [/D]	0.26 ± 0.09
Posterior Radius [mm/D]	0.06 ± 0.02
Posterior Surface Asphericity –Power Slope [/D]	-0.09 ± 0.04
Surface Refractive Power –Power Slope [D/D]	0.44 ± 0.09
Equivalent Refractive Index	No change

Table 7.4: The age-dependent changes in lens shape as function of the change in lens power (accommodation). A statistically significant age-dependent trend was observed only for the change in anterior lens radius of curvature with change in lens power. The mean values are given for the parameters which did not have statistically significant age dependence.

7.4. Discussion

7.4.1. Age-dependent decrease in accommodation amplitude

During simulated accommodation the refractive power of a 2-3 year old baboon lens decreases by 25-30D. This change in refractive power decreases with age. This decrease in simulated accommodative amplitude is related to the age-dependent decrease in unstretched lens refractive power. The unstretched lens refractive power decreases with age at a rate (-1.4 D/year) similar to the isolated lens (-1.3 D/year) (Section 6.7). The refractive power of the stretched lens remains relatively constant over the sampled age range (mean = 30.2±3 D, p=0.15). The change in refractive power of the lens (accommodative amplitude) decreases with age by 1.1 D per year (Table 6.1). This loss of simulated accommodation amplitude in the baboon corresponds well with the in vivo

loss of accommodative amplitude reported for the rhesus monkeys over a similar age range (-1.02 D/year, Crawford et al 1990). These findings suggest that the baboon lens and accommodative mechanism are a good model for studying the age-dependent changes leading to presbyopia, and that simulated accommodation by lens stretching accurately reproduces the effects of the in vivo accommodation mechanism on the refractive power of the lens.

The shape parameters of the maximally stretched (dis-accommodated) lens including the diameter, thickness and surface curvatures are constant throughout the sampled age range. These findings are consistent with the findings of studies performed on in vivo humans (Dubbelman et al 2005), in vitro human lenses (Glasser and Campbell 1999) and in vivo rhesus monkeys (Wendt et al 2008). The combination of these two trends cause the maximum changes in lens diameter, thickness and surface curvatures to decrease with age (Figure 7.11). These findings indicate that as the lens ages, the shape of the unstretched (maximally accommodated lens) approaches that of the maximally stretched (dis-accommodated) lens.

7.4.2. Changes in lens surface curvatures during simulated accommodation

There was an age dependent decrease (negative shift) in the anterior surface curvature-power slope. However, the posterior surface curvature-power slope (Figure 7.7D) did not significantly change with age. These findings agree with the in vivo observation that it is mainly the anterior surface of the lens that changes with accommodation. These results also suggest that there is a different contribution of the anterior and posterior lens surface to the loss of accommodation with age. The posterior

lens surface seems to retain most of its accommodative ability while the changes in the anterior lens surface progressively decrease with age.

7.4.3. Refractive contributions of the lens surfaces to the change in lens power

The refractive power of the lens surfaces is calculated using a technique described in Section 4.7. Figure 7.9 illustrates the age dependent decrease in the calculated refractive power of the unstretched (maximally accommodated) lens surfaces. The results of the unstretched lens are similar to those found in the isolated lens. The calculated refractive power of the stretched (dis-accommodated) lens surfaces is constant throughout the measured age range (mean =12.15 D ± 1.7 D, p=0.70). As a result the maximum change in surface refractive power induced during simulated accommodation decreases with age (Figure 7.14). The surface refractive power contributes 40-45 % of the total lens refractive power independent of age or accommodative state. The remainder (50-55 %) of the static lens refractive power is due to the lens refractive index gradient.

The surface refractive power contributes 40.75% ± 3.5% of the total lens refractive power independent of age and accommodative state. These results indicate the change in surface refractive power contributes 40% of the accommodative amplitude of the lens. The majority of the total refractive power change of the lens is due to refractive index gradient.

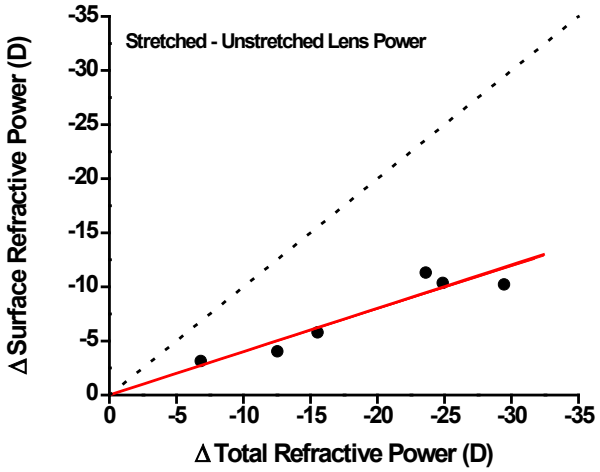

Figure 7.14:. The surface refractive power contributes 40-45% of the total refractive power of the lens independent of age or accommodative state. Δ Surface Refractive Power (D) = 0.40·Δ Total Refractive Power (D)

The fact that there was no change in the equivalent refractive index is another indication that the contribution of the gradient does not change with accommodation. The age-dependent rate of decrease in the isolated lens equivalent refractive index matches well with the age-dependent decrease in the maximally stretched lens equivalent refractive index (-1.1×10^{-3}/year) (Table 7.1).

7.5. Dynamic age-dependent optical model of the baboon crystalline lens

An age and accommodation dependent optical model of the in vitro baboon lens (Eq. 7.5) incorporating the power dependence of the lens shape and power (Eq. 7.4) was developed from the age dependent optical model of the isolated lens (Eq. 7.3 and Section 6.5). This model is valid for the pre-presbyopic baboon from 2 to 21 years of age. The model predicts the change in lens shape based on the level of accommodation. A similar approach can be used to develop optical models for the human, rhesus and cynomolgus lenses once data has been acquired over a wide enough age range.

		Age and Accommodation dependent parameters
Accommodative State (D)	ΔP_{max}	27.5 - 1.1 · Age
Thickness (mm)	t	4.64-0.04·Age -0.04 · ΔP
Diameter (mm)	d	7.59+0.06·Age + 0.04 · ΔP
Anterior Radius (mm)	R_A	4.81±0.27 (0<age <14.7) -2.54+0.51·Age (14.7<age <27.3) + (-0.14 -0.01·Age) · ΔP
Anterior Asphericity	P_A	-0.89–0.25·Age + 0.26 · ΔP
Posterior Radius (mm)	R_P	-3.03-0.09·Age + 0.06 · ΔP
Posterior Asphericity	P_P	0.29-0.06·Age -0.09 · ΔP
Equivalent Refractive Index	N_{EQ}	$1.434–7.4x10^{-4}$·Age
Equivalent Refractive Power (D)	P	52.45– 1.3·Age
Lens Surface Power (D)	P_S	21.56-0.37·Age + 0.44 · ΔP

Table 7.5: An age and accommodation dependent optical model of the hamadryas baboon crystalline lens. This model is valid between the ages of 2 and 21 years of age. All ages are in years. ΔP (D) corresponds to the accommodative state and is given in Diopters. For the unaccommodated lens the accommodative state is ΔP (D) = 0 and is independent of age. The maximum accommodative state is age dependent and is used to calculate all other terms in the model.

7.6. Implications for Phaco-Ersatz

A set of initial optical design parameters for the Phaco-Ersatz implant were derived in Chapter 6 based on the age-dependent model of the isolated lens. These parameters restore the refractive power of the maximally accommodated state of the natural lens. One of the remaining issues was whether the absence of the gradient has an effect on the accommodation amplitude provided by this implant. The results of Chapter 7 show that the equivalent refractive index remains constant with accommodation. This finding suggest that a lens with a uniform refractive index equal to the equivalent refractive index of the natural lens will provide the same accommodation amplitude as the natural lens with its gradient as long as the starting power remains the same. The design parameters for the Phaco-Ersatz implant given in Section 6.6 are therefore expected to provide both the static power and accommodation amplitude of a 20 year old human lens if the mechanical properties are adequate.

7.7. Summary

This chapter presents an age and accommodation dependent optical model of the pre-presbyopic hamadryas baboon lens. This model is based on direct lens power and shape measurements acquired during simulated accommodation experiments. The same technique can be applied to the human lens once sufficient data is available. The key findings of this part of the study are:

- The model predicts that the loss of accommodative amplitude of the crystalline lens is due to the loss of maximally accommodated lens power.
- The gradient refractive index contributes 60% of the total refractive power of the lens independent of accommodative state.

- The surfaces contribute the remaining 40% of the lens refractive power independent of accommodative state.

- The forces required to change the lens shape and power did not change significantly over the sampled age range (young pre-presbyopic baboon lens).

- The shape and power of the maximally stretched lens did not change with age over the sampled age range.

- As the lens ages, the shape of the unstretched (maximally accommodated) lens approaches that of the maximally stretched (dis-accommodated) lens.

- The posterior surface of the lens retains its accommodative ability with age whereas the changes in shape of the anterior surface decrease with age

Together these findings suggest that the loss of accommodation with age is due to the fact that, with age, the shape of the maximally accommodated lens progressively converges to that of the relaxed lens.

The fact that the contribution of the gradient index remains constant with accommodation suggests that accommodation can be restored by replacing the natural crystalline lens with a Phaco-Ersatz implant which has a uniform refractive index equal to the equivalent refractive index of the natural lens. The initial optical design parameters provided in Section 6.6 are expected to restore both the static power and the accommodation amplitude of a 20 year old natural lens.

CHAPTER 8. SUMMARY AND CONCLUSION

The goal of this dissertation is to better understand the relationship between the crystalline lens shape, its non-uniform refractive index gradient and its optical power and their changes with age and accommodation. This optical model will be used to derive optical design criteria for the Phaco-Ersatz implant.

In this study direct lens power and shape measurements were acquired on isolated lenses, and on lenses mounted in a lens stretching system designed to simulate accommodation. These direct measurements were used to develop an age-dependent optical-mechanical model of the lens during accommodation. This study required the development of several lens shape and power measurement techniques as well as optical models. The main technical achievement was the development of a Scheimpflug imaging system optimized for imaging the crystalline lens. This Scheimpflug system provides a large depth of field, an illumination system with a long depth of focus, and a correction algorithm, all specifically designed for quantitative cross sectional imaging of the in vitro lens. To the best of our knowledge there are no other similar systems available optimized for lens biometry. Other approaches have either used commercial Scheimpflug systems (Dubbelman and Van der Heijde 2001, Dubbelman et al 2005) or custom built systems which did not include a correction algorithm (Brown 1974).

In the first aim of this study, measurements of isolated lens shape and power on a large group of fresh human and non-human primate lenses over a wide age range led to the development of a complete age-dependent optical model of the isolated lens. This optical model showed that the growth of the lens has a significant contribution to the loss of accommodation. The results from this section of the study indicate the rhesus monkey

and the hamadryas baboon lenses are good models for the human lens. To our knowledge this study represents the largest collection of optical and biometric data on the human and non-human primate crystalline lenses in terms of sample size and age distribution.

In the second aim, measurements of the in vitro lens shape and power during simulated accommodation were performed on a group of fresh human and non-human primate lenses over a wide age range. The data was used to develop an age and accommodation dependent optical model for the baboon lens. The results showed that, with age, the shape and power of the maximally accommodated lens progressively converges to the shape and power of the relaxed lens. These findings indicate the growth pattern of the lens causes an age-dependent decrease in accommodated amplitude which ultimately leads to presbyopia.

The results of this study were used to derive initial optical parameters for the Phaco-Ersatz implant. In particular the fact that the refractive contribution from the gradient remains constant with accommodation shows that accommodation can be restored with an implant having a uniform refractive index. From a paraxial optics point of view both the static power and the accommodation amplitude of the natural lens, which has a gradient of refractive index, can be restored with a Phaco-Ersatz implant with a uniform refractive index.

The age and accommodation dependent model could only be completed for the baboon lens. This model is currently being extended for the human lens. However, this requires additional measurement of young pre-presbyopic human lens shape and power during simulated accommodation. Further areas of study include improvements to the biometry technique which will allow for corrected measurements of lens surface

asphericity as well as for biometry of the internal lens structures including the nucleus and the cortex. Future studies are also needed to determine the effects of this dynamic lens model on optical aberrations. These investigations can be done by including the age and accommodation dependent optical model of the lens in an age-dependent optical model of the whole eye (Norby 2005). Finally the findings presented in this study must be validated with in vivo measurements.

In conclusion, our results show independent of changes in the elastic properties of the lens, the normal age-related growth of the lens is a major contributor to the progressive loss of accommodation amplitude. Our results also suggest that accommodation can be restored by refilling the lens with a material with uniform refractive index. The loss of the lens gradient will not affect the restoration of accommodation.

REFERENCES

Augusteyn RC, Rosen AM, Borja D, Ziebarth NM, and Parel JM. Biometry of primate lenses during immersion in preservation media. *Molecular Vision,* 12: 740-7; 2006.

Augusteyn RC. Growth of the lens: *in vitro* observations. *Clinical & Experimental Optometry*, 91(3): 226-239; 2008.

Atchison DA. Review of accommodation and presbyopia. *Ophthalmic & Physiological Optics*, 15: 255-272; 1995.

Atchison DA, Collins MJ, Wildsoet CF, Christensen J, Waterworth MD. Measurement of monochromatic ocular aberrations of human eyes as a function of accommodation by the Howland aberroscope technique. *Vision Research*, 35: 313-23; 1995.

Atchison DA, and Smith G. *Optics of the human eye*. Butterworth Heinemann, Boston, 2000.

Bennett AG. A method of determining the equivalent powers of the eye and its crystalline lens without resort to phakometry. *Ophthalmic & Physiological Optics,* 8(1): 53-59; 1988.

Bennett AG, and Rabbetts RB. *Clinical visual optics*, 3rd edition. Butterworth-Heinmann, London. 1998.

Bito LZ, DeRousseau CJ, Kaufman PL, Bito JW. Age-dependent loss of accommodative amplitude in rhesus monkeys: an animal model for presbyopia. *Investigative Ophthalmology & Visual Science*, 23(1): 23-31; 1982.

Borja D, Manns F, Ho A, Ziebarth N, Rosen AM, Jain R, Amelinckx A, Arrieta E, Augusteyn RC, Parel JM. Optical power of the isolated human crystalline lens. *Investigative Ophthalmology & Visual Science,* 49: 2541-2548; 2008.

Born M and Wolf E. *Principles of optics: electromagnetic theory of propagation, interference and diffraction of light*. Pergamon Press, New York, 1980.

Brown N. Slit-image photography. *Transactions of the Ophthalmological Society of the U.K.*, 89:397-408; 1970.

Brown N. The change in lens curvature with age. *Experimental Eye Research*, 19:175-183; 1974.

Burd HJ, Judge SJ, Cross JA. Numerical modelling of the accommodating lens. *Vision Research,* 42(18):2235-2251; 2002.

Crawford KS, Kaufman PL, Bito LZ. The role of the iris in accommodation of rhesus monkeys. *Investigative Ophthalmology & Visual Science,* 31(10):2185-90; 1990.

Croft MA, Kaufman PL, Crawford KS, Neider MW, Glasser A, Bito LZ. Accommodation dynamics in aging rhesus monkeys. *American Journal of Physiology*, 275:1885-1897; 1998.

Croft MA, Glasser A, Heatley G, McDonald J, Ebbert T, Dahl DB, Nadkarni NV, Kaufman PL. Accommodative ciliary body and lens function in rhesus monkeys, I: normal lens, zonule and ciliary process configuration in the iridectomized eye. *Investigative Ophthalmology & Visual Science,* 47: 1076-1086; 2006.

Croft MA, Glasser A, Heatley G, McDonald J, Ebbert T, Nadkarni NV, Kaufman PL. The zonula, lens, and circumlental space in the normal iridectomized rhesus monkey eye. *Investigative Ophthalmology & Visual Science,* 47:1087-1095; 2006.

Datiles MB, Edwards PA, Trus BL, Green SB. *In vivo* studies on cataracts using the scheimpflug slit lamp camera. *Investigative Ophthalmology & Vision Science,* 28: 1707-1710; 1987.

Denham D, Holland S, Mandelbaum S, Pflugfelder S, and Parel JM. Shadow photogrammetric apparatus for the quantitative evaluation of corneal buttons. *Ophthalmic Surgery*, 20:794-99; 1989.

Denham DB, Rosen A, Manns F, Margolesky J, Parel JM, Ho A. Measurement of excised primate lens power in aqueous solutions using simply modified lensometers. *Investigative Ophthalmology & Vision Science,* 44: E-Abstract 244; 2003.

Duane A. Normal values of the accommodation at all ages. *Journal of the American Medical Association,* 59:1010-1013; 1912.

Duane A. Normal values of the accommodation at all ages. *Transactions of Ophthalmology AMA*, 383; 1912.

Dubbelman M, Van der Heijde GL. The shape of the aging human lens: curvature, equivalent refractive index and the lens paradox. *Vision Research,* 41:1867-77; 2001.

Dubbelman M, Van der Heijde GL, Weeber HA. Change in shape of the aging human crystalline lens with accommodation. *Vision Research*, 45:117-132; 2005.

El-Hage SG, Berny F. Contribution of the crystalline lens to the spherical aberration of the eye. *Journal of the Optical Society of America A*, 63: 205-11; 1973.

Emsley HH. *Visual optics,* 5th edition. 1952.

Fincham EF. *The mechanism of accommodation.* British Journal of Ophthalmology, Monograph Supplement VIII, Pulman & Sons Ltd. London, 1937.

Fisher, R.F. The significance of the shape of the lens and capsular energy changes in accommodation. *Journal of Physiology*, 201:21-47; 1969.

Garner LF, Yap M, Scott R. Crystalline lens power in myopia. *Optometry & Vision Science,* 69(11):863-865; 1992.

Garner LF, Yap MK. Changes in ocular dimensions and refraction with accommodation. *Ophthalmic & Physiological Optics,* 17(1):12-17; 1997.

Garner LF. Calculation of the radii of curvature of the crystalline lens surfaces. *Ophthalmic & Physiological Optics,* 17(1):75-80; 1997.

Glasser A, Campbell MC. Presbyopia and the optical changes in the human crystalline lens with age. *Vision Research*, 38:209-29; 1998.

Glasser A, Kaufman PL. The mechanism of accommodation in primates. *Ophthalmology*, 106(5):863-72; 1999.

Glasser A, Campbell MC. Biometric, optical and physical changes in the isolated human crystalline lens with age in relation to presbyopia. *Vision Research*, 39:1991-2015; 1999.

Glasser A, Wendt M, Ostrin L. Accommodative changes in lens diameter in rhesus monkeys. *Investigative Ophthalmology & Vision Science,* 47(1):278-86; 2006.

Goss DA, Van Veen HG, Rainey BB, Feng B. Ocular components measured by keratometry, phakometry, and ultrasonography in emmetropic and myopic optometry students. *Optometry & Vision Science,* 74(7):489-495; 1997.

Gullstrand A. Appendix 11.3. *The optical system of the eye. In Helmholtz H. von, physiological optics,* Vol. 1. Pp.350-358. English translation: J.P.C. Southhall (ed.) New York: Optical Society of America.: Dover Publications, New York. 1909, Reprinted 1962.

Haefliger E, and Parel JM. Accommodation of an endocapsular silicone lens (Phaco-Ersatz) in the aging rhesus monkey. *Journal of Refractive & Corneal Surgery,* 10:550-555; 1994.

Hemenger RP, Garner LF, Ooi CS. Change with age of the refractive index gradient of the human ocular lens. *Investigative Ophthalmology & Vision Science,* 36(3):703-707; 1995.

Hermans EA, Dubbelman M, van der Heijde GL, Heethaar RM. Estimating the external force acting on the human eye lens during accommodation by finite element modeling. *Vision Research,* 46:3642-3650; 2006.

Hermans EA, Dubbelman M, van der Heijde GL, Heethaar RM. Change in the accommodative force on the lens of the human eye with age. *Vision Research*, 48(1):119-26; 2008.

Howcroft MJ, Parker JA. Aspheric curvatures for the human lens. *Vision Research,* 17(10):1217-1223; 1977.

Ip JM, Huynh SC, Kifley A, Rose KA, Morgan IG, Varma R, Mitchell P. Variation of the contribution from axial length and other oculometric parameters to refraction by age and ethnicity. *Investigative Ophthalmology & Vision Science,* 48(10): 4846-4853; 2007.

Jones CE, Atchison DA, Meder R, Pope JM. Refractive index distribution and optical properties of the isolated human lens measured using magnetic resonance imaging (MRI). *Vision Research*, 45(18):2352-2366; 2005.

Jones LA, Mitchell GL, Mutti DO, Hayes JR, Moeschberger ML, Zadnik K. Comparison of ocular component growth curves among refractive error groups in children. *Investigative Ophthalmology & Vision Science,* 46(7):2317-2327; 2005.

Kasthurirangan S, Markwell EL, Atchison DA, Pope JM. In vivo study of changes in refractive index distribution in the human crystalline lens with age and accommodation. *Investigative Ophthalmology & Vision Science,* 49(6):2531-2540; 2008.

Kaufman PL, Rohen JW, and Barany EH. Hyperopia and loss of accommodation following ciliary muscle disinsertion in the cynomolgus monkey physiologic and scanning electron microscopic studies. *Investigative Ophthalmology & Visual Science*, 18: 665-673; 1979.

Kaufman PL, and Alm A. *Adler's Physiology of the Eye*. Mosby, Philadelphia, PA, 2007.

Kaufman PL, Calkins BT, and Erickson KA. Ocular biometry of the cynomolgus monkey. *Current Eye Research*, 1(5):307-9; 1981.

Kingslake R. *Lens Design Fundamentals*. Academic Press, Burlington, MA, 1978.

Koretz JF, Handelman GH, Brown NP. Analysis of human crystalline lens curvature as a function of accommodative state and age. *Vision Research*, 24:1141-51; 1984.

Koretz JF, Neider MW, Kaufman PL, Bertasso AM, DeRousseau CJ, Bito LZ. Slit-lamp studies of the rhesus monkey eye. I. Survey of the anterior segment. *Experimental Eye Research,* 44(2):307-18; 1987.

Koretz JF, Bertasso AM, Neider MW, True-Gabelt BA, Kaufman PL. Slit-lamp studies of the rhesus monkey eye: II. Changes in crystalline lens shape, thickness and position during accommodation and aging. *Experimental Eye Research*, 45(2):317-26; 1987.

Koretz JF, Bertasso AM, Neider MW, Kaufman PL. Slit-lamp studies of the rhesus monkey eye: III. The zones of discontinuity. *Experimental Eye Research*, 46 (6):871-80; 1988.

Koretz JF, Cook CA. Methods to obtain quantitative parametric descriptions of the optical surfaces of the human crystalline lens from Scheimpflug slit-lamp images. I. Image processing methods. *Journal of the Optical Society of America A*, 15:1473-85; 1998.

Koretz JF, Cook CA, Kaufman PL. Aging of the human lens: changes in lens shape at zero-diopter accommodation. *Journal of the Optical Society of America A*, 18(2):265-72; 2001.

Koretz JE, Strenk SA, Strenk LM, Semmlow JL. Scheimpflug and high-resolution magnetic resonance imaging of the anterior segment: a comparative study. *Journal of the Optical Society of America A*. 21(3):346-354; 2004.

Koopmans SA, Terwee T, Glasser A, Wendt M, Vilupuru AS, van Kooten TG, Norrby S, Haitjema HJ, and Kooijman AC. Accommodative lens refilling in rhesus monkeys. *Investigative Ophthalmology & Visual Science,* 47(7):2976-84; 2006.

Kooijman AC. Light distribution on the retina of a wide-angle theoretical eye. *Journal of the Optical Society of America*, 73(11):1544-50; 1983.

Lapuerta P, Schein SJ. A four-surface schematic eye of macaque monkey obtained by an optical method. *Vision Research*, 35(16):2245-54; 1995.

Liou HL and Brennan N. The prediction of spherical aberration with schematic eyes. *Ophthalmic and Physiological Optics,* 16(4): 348-354; 1996.

Liou HL and Brennan N. Anatomically accurate, finite model eye for optical modeling. *Journal of the Optical Society of America A,* 14(8): 1684-1694; 1997.

Liou HL, Brennan NA. Letter contrast sensitivity function of the eye. *Acta Ophthalmologica Scandinavica*, 76(3):325-8; 1998.

Lotmar W. Theoretical eye model with aspherics. *Journal of the Optical Society of America*. 61(11): 1522-1529; 1971

Ludwig K, Kampik A. The mechanism of accommodation in primates. *Ophthalmology,* 107(2):221-2; 2000.

Manns F, Ho A, Kruger RR. *Customized visual correction of presbyopia. In Wavefront-guided corrections: The quest for super vision*, 2nd Edition, Chapter 41. p 353-360. SLACK Inc, Thorofare, NJ, 2004.

Manns F, Fernandez V, Zipper S, Sandadi S, Hamaoui M, Ho A, Parel JM. Radius of curvature and asphericity of the anterior and posterior surface of human cadaver crystalline lenses. *Experimental Eye Research,* 78(1):39-51; 2004.

Manns F, Parel JM, Denham D, Billotte C, Ziebarth N, Borja D, Fernandez V, Aly M, Arrieta E, Ho A, Holden B. Optomechanical response of human and monkey lenses in a lens stretcher. *Investigative Ophthalmology & Visual Science,* 48:3260-3268; 2007.

Moffat BA, Atchison DA, Pope JM. Age-related changes in refractive index distribution and power of the human lens as measured by magnetic resonance micro-imaging *in vitro*. *Vision Research*, 42:1683-93; 2002.

Mutti D, Zadnik K, and Adams A. A video technique for phakometry of the human crystalline lens. *Investigative Ophthalmology & Visual Science,* 33(5):1771-1782; 1992.

Mutti D, Zadnik K, and Adams A. The equivalent refractive index of the crystalline lens in childhood. *Vision Research,* 35(11):1565-1573; 1995.

Mutti DO, Mitchell GL, Jones LA, Friedman NE, Frane SL, Lin WK, Moeschberger ML, Zadnik K. Axial growth and changes in lenticular and corneal power during emmetropization in infants. *Investigative Ophthalmology & Visual Science,* 46(9):3074-3080; 2005.

Navarro R, Santamaria J, Bescos J. Accommodation-dependent model of the human eye with aspherics. *Journal of the Optical Society of America A*, 2:1273-81; 1985.

Navarro R, Palos F, González LM. Adaptive model of the gradient index of the human lens. I. Formulation and model of aging ex vivo lenses. *Journal of the Optical Society of America A*, 24(8):2175-85; 2007

Neider MW, Crawford K, Kaufman PL, Bito LZ. In vivo videography of the rhesus monkey accommodative apparatus. Age-related loss of ciliary muscle response to central stimulation. *Archives of Ophthalmology,* 108:69-74; 1990.

Nishi O, Nakai Y, Mizumoto Y, and Yamada Y. Capsule opacification after refilling the capsule with an inflatable endocapsular balloon. *Journal of Cataract & Refractive Surgery*, 23(10):1548-55; 1997.

Nishi O, and Nishi K. Accommodation amplitude after lens refilling with injectable silicone by sealing the capsule with a plug in primates. *Archives of Ophthalmology*, 116(10):1358-61; 1998.

Norby S. The Dubbelman Eye model analyzed by ray tracing through spheric surfaces. *Ophthalmic Physiological Optics*, 25: 153-161;2005.

Oyster, Clyde W. *The human eye: structure and function*. Sunderland, Mass, Sinauer Associates, 1999.

Parel JM, Gelender H, Trefers WF, Norton EW. Phaco-Ersatz: cataract surgery designed to preserve accommodation. *Graefes Archives Clinical Experimental Ophthalmology*, 224:165-73; 1986.

Parel JM, Manns F, Fernandez V, Billotte C, Denham D, Lamar P, Stoiber J, Orozco M, Ho A. Dioptric power vs zonular tension during ex-vivo simulated accommodation of primate crystalline lenses before and after refilling. *Investigative Ophthalmology & Visual Science,* 45: E-abstract 887; 2003.

Parel, JM, Lee W, Lamar P, Acosta AC, Abri A, Nose I, Manns F, Manual lens stretching apparatus (MLSA) for rapid analysis of the optical properties of the natural lens, accommodating IOL and refilled lens capsule (PHAC0-ERSATZ). *Investigative Ophthalmology & Visual Science,* 45: E-abstract 1724; 2004.

Pierscionek BK, Chan DY, Ennis JP, Smith G, Augusteyn RC. Nondestructive method of constructing three-dimensional gradient index models for crystalline lenses: I. Theory and experiment. *American Journal of Optometry and Physiological Optic,* 65(6):481-91; 1988.

Pierscionek BK, Chan DY. Refractive index gradient of human lenses. *Optometry & Vision Science,* 66(12):822-829; 1989.

Pierscionek BK. Refractive index of the human lens surface measured with an optic fiber sensor. *Ophthalmic Research*, 26(1):32-5, 1994.

Qiao-Grider Y, Hung LF, Kee CS, Ramamirtham R, Smith EL 3rd. Normal ocular development in young rhesus monkeys (*Macaca mulatta*). *Vision Research,* 47(11):1424-44; 2007.

Remington LA. *Clinical anatomy of the visual system*. Elsevier Butterworth Heinmann, St. Louis MS, 2005.

Rosales P, Dubbelman M, Marcos S, van der Heijde R. Crystalline lens radii of curvature from Purkinje and Scheimpflug imaging. *Journal of Vision,* 6(10):1057-1067; 2006.

Rosales P, Wendt M, Marcos S, Glasser A. Changes in crystalline lens radii of curvature and lens tilt and decentration during dynamic accommodation in rhesus monkeys. *Journal of Vision*, 8(1):18.1–12; 2008.

Rosen A, Denham D, Manns F, Fernandez V, Augusteyn R, Parel JM, Shadow photogrammetric method for assessing changes in physical lens dimensions during immersion in tissue preservation media. *SPIE Proceedings*, 4951:07; 2003.

Rosen AM, Denham DB, Fernandez V, Borja D, Ho A, Manns F, Parel JM, Augusteyn RC. *In vitro* dimensions and curvatures of human lenses. *Vision Research*, 46:1002-1009; 2006.

Schachar RA. Central surface curvatures of postmortem-extracted intact human crystalline lenses: implications for understanding the mechanism of accommodation. *Ophthalmology,* 111(9):1699-1704; 2004.

Schachar RA, Abolmaali A, Le T. Insights into the age-related decline in the amplitude of accommodation of the human lens using a non-linear finite-element model. *British Journal of Ophthalmology,* 90(10):1304-1309; 2006.

Sivak JG, Kreuzer RO. Spherical aberration of the crystalline lens. *Vision Research,* 23(1):59-70; 1983.

Smith, WJ. *Modern optical engineering; the design of optical systems*. McGraw-Hill, New York, 1966.

Smith G, Pierscionek BK, Atchison DA. The optical modeling of the human lens *Ophthalmic and physiological optics*. 11:359-369; 1991.

Smith G, Atchison DA, Pierscionek BK. Modeling the power of the aging human eye. *Journal of the Optical Society of America A,* 9:2111-7; 1992.

Smith G, Atchison DA. Equivalent power of the crystalline lens of the human eye: comparison of methods of calculation. *Journal of the Optical Society of America A*, 14: 2537-46; 1997.

Smith G, Atchison DA. The gradient index and spherical aberration of the lens of the human eye. *Ophthalmic Physiological Optics,* 21:317-26; 2001.

Smith G. The optical properties of the crystalline lens and its significance. *Clinical and Experimental Optometry.* 86(1):3-18; 2003.

Strenk SA, Strenk LM, Guo S. Magnetic resonance imaging of aging, accommodating, phakic, and pseudophakic ciliary muscle diameters. *Journal of Cataract & Refractive Surgery,* 32(11):1792-1798; 2006.

Subramanian R, Cook C, Croft M, DePaul KL, Neider M, Ferrier NJ, Kaufman PL, Koretz JF. Unilateral real-time Scheimpflug videography to study accommodation dynamics in human eyes. *Investigative Ophthalmology & Visual Science,* 45: E-abstract 240; 2003.

Tornqvist G. Effect of topical carbachol on the pupil and refraction in young and presbyopic monkeys. *Investigative Ophthalmology & Visual Science*; 5:186-195; 1966.

Vilupuru A, and Glasser A. Optical and biometric relationships of the isolated pig crystalline lens. *Ophthalmic and Physiological Optics*, 21: 296-311; 2001.

Von Helmholtz HH (Translated by JPC Southhall): *Treatise on physiological optics*. Mineola, Dover, NY, 1962.

Weale RA, *The aging eye.* Hoeber Medical Division, Harper & Row, New York, NY, 1963.

Welford WT. *Aberrations of optical systems,* 1st edition. Taylor & Francis, Oxford, 1986.

Wendt M, Croft MA, McDonald J, Kaufman PL, Glasser A. Lens diameter and thickness as a function of age and pharmacologically stimulated accommodation in rhesus monkeys. *Experimental Eye Research,* 86(5):746-752; 2008.

Zadnik K, Mutti DO, Friedman NE, Adams AJ. Initial cross-sectional results from the Orinda Longitudinal Study of Myopia. *Optometry & Vision Science,* 70(9):750-758; 1993.